Author:
Nicolaidou, Evangelia

Title:
Reduced-order modelling of nonlinear dynamic structures

Reduced-Order Modelling of Nonlinear Dynamic Structures

EVANGELIA NICOLAIDOU

Department of Mechanical Engineering
UNIVERSITY OF BRISTOL

A dissertation submitted to the University of Bristol
in accordance with the requirements of the degree of
Doctor of Philosophy in the Faculty of Engineering.

Word count: ~46,000

OCTOBER 2022

Abstract

With the ever-increasing demand for better performance, modern engineering structures continue to tend towards thin, low-weight, and highly flexible designs. As a result, they are often required to undergo large deformations or rotations during operation, and experience geometric nonlinearity. However, performing nonlinear dynamic analysis of large models can pose prohibitively high computational costs during the design and optimisation of structures. Reduced-order modelling methods aim to ease this bottleneck, by constructing low-dimensional models which are able to capture the salient dynamics of the full-order model in a much more efficient manner.

The aim of this thesis is to further the current state-of-the-art of nonlinear reduced-order modelling methodologies, which are applicable to geometrically nonlinear structures built using commercial finite element software. The methods proposed herein build on existing techniques, exploiting their merits and aiming to address their limitations. Specifically, the focus of this thesis is on so-called force-based indirect reduction techniques, such as the Implicit Condensation and Expansion (ICE) method, which rely on a static condensation procedure to achieve reduction for structures characterised by slow/fast dynamics.

In this thesis, several developments of the ICE method are proposed. First it is shown that, in order to fully account for the effect of the statically condensed modes, the reduced dynamics must include not only higher orders of nonlinearity, compared to the full-order model, but also some additional velocity- and acceleration-dependent terms. The latter components capture the kinetic energy of the condensed modes, which the standard method neglects, thus extending its applicability to a far wider range of structures whilst maintaining accuracy to higher deflection amplitudes.

Then, a method for efficiently detecting the existence of internal resonances between reduced and condensed modes is proposed. This may serve as a tool for guiding the reduction basis selection process, as well as verifying the accuracy of reduced-order models, without the need for full-order simulations.

Finally, the ICE method is extended to nonconservative structures, such that forced response curves may be computed directly. The proposed formulation is such that any energy gained or dissipated by the condensed modes is accounted for in the reduced dynamics, enabling features such as parametric resonances — which would otherwise be neglected — to be accurately captured.

Acknowledgements

First and foremost, I would like to thank my supervisors, Dr. Tom Hill and Prof. Simon Neild, for placing their trust in me and for generously providing excellent guidance and support over the last few years. They have played no small part in my PhD journey being a rewarding and genuinely enjoyable experience, and I am extremely fortunate and grateful for that.

I would like to thank Dr. Dimitris Karamitros, Dr. Alberto Gambaruto, and Prof. Guido Herrmann, with whom I have worked as an undergraduate at Bristol. Thank you to each of them for guiding me through my early ventures into academic research, and for encouraging me to pursue a PhD. I am also grateful to the many talented friends and colleagues I have worked with during my PhD. I would particularly like to thank Dongxiao Hong and Alessandra Vizzaccaro for the interesting and insightful discussions, and for inspiring me to be a better researcher. In addition, I would like to acknowledge the financial support of the EPSRC through a DTP studentship.

I am very grateful to all my friends, both in Bristol and beyond. In particular, I would like to thank my housemates, Vaso and Maro, for providing a seemingly endless supply of baked goods and good vibes; my *almost* housemates, George, Christos and Martha, for keeping me sane through the pandemic; and my partner, Markus, for all the adventures and his incredible patience, love and support.

Last but not least, I am very grateful to my family back home, and especially my parents, for always encouraging me to follow my passions and believing I can achieve any goal.

Author's declaration

I declare that the work in this dissertation was carried out in accordance with the requirements of the University's *Regulations and Code of Practice for Research Degree Programmes* and that it has not been submitted for any other academic award. Except where indicated by specific reference in the text, the work is the candidate's own work. Work done in collaboration with, or with the assistance of, others, is indicated as such. Any views expressed in the dissertation are those of the author.

SIGNED:

DATE:

Publications

As a result of the work conducted in this thesis, the following publications have been produced.

Journal articles

- Nicolaidou, E., Melanthuru, V. R., Hill, T. L. and Neild, S. A. (2020). Accounting for quasi-static coupling in nonlinear dynamic reduced-order models. *Journal of Computational and Nonlinear Dynamics*, 15(7):071002.
- Hong, D., Nicolaidou, E., Hill, T. L. and Neild, S. A. (2020). Identifying phase-varying periodic behaviour in conservative nonlinear systems. *Proceedings of the Royal Society A: Mathematical, Physical and Engineering Sciences*, 476(2237).
- Nicolaidou, E., Hill, T. L. and Neild, S. A. (2020). Indirect reduced-order modelling: Using nonlinear manifolds to conserve kinetic energy. *Proceedings of the Royal Society A: Mathematical, Physical and Engineering Sciences*, 476(2243).
- Nicolaidou, E., Hill, T. L. and Neild, S. A. (2021). Detecting internal resonances during model reduction. *Proceedings of the Royal Society A: Mathematical, Physical and Engineering Sciences*, 477(2250).
- Nicolaidou, E., Hill, T. L. and Neild, S. A. (2022). Nonlinear mapping of non-conservative forces for reduced-order modelling. *Proceedings of the Royal Society A: Mathematical, Physical and Engineering Sciences*, 478(2268).

Conference proceedings

- Nicolaidou, E., Hill, T. L. and Neild, S. A. (2023). Indirect reduced-order modelling of nonconservative nonlinear structures. *Nonlinear Structures & Systems, Volume 1*, pp. 35–37. Springer, Cham.

Table of Contents

List of Figures

List of Tables

Nomenclature

Subscripts

$\bullet_r$	Reduced modes
$\bullet_s$	Statically coupled modes
$\bullet_u$	Unmodelled modes
$\bullet_{\mathrm{st}}$	Static solution

Operators

$\dot{\bullet}$	Time derivative
$\ddot{\bullet}$	Second time derivative
$\bullet^\intercal$	Transpose
$\bullet^{-1}$	Inverse

Scalars

t	Time
N	Number of physical DOFs
R	Number of reduced modes
S	Number of statically coupled modes
U	Number of unmodelled modes
$\mathcal{T}$	Kinetic energy
$\mathcal{V}$	Potential energy
$\mathcal{L}$	Lagrangian

Vectors

$\mathbf{x}$	Vector of physical coordinates
$\mathbf{q}$	Vector of (full) modal coordinates
$\mathbf{r}$	Vector of reduced coordinates
$\mathbf{f}(\mathbf{x})$	Vector of nonlinear internal forces in the physical space
$\mathbf{f}_q(\mathbf{q})$	Vector of nonlinear internal forces in the (full) modal space
$\mathbf{f}_r(\mathbf{r})$	Vector of nonlinear internal forces in the reduced space
$\mathbf{F}$	Vector of external forces in the physical space
$\mathbf{g}$	Vector of quasi-static coupling functions in the modal space
θ	Vector of quasi-static coupling functions in the physical space

Matrices

$\mathbf{M}$	Linear mass matrix in the physical space
$\mathbf{K}$	Linear stiffness matrix in the physical space
$\mathbf{\Lambda}$	Linear stiffness matrix in the (full) modal space
$\mathbf{\Lambda}_r$	Linear stiffness matrix in the reduced space
$\mathbf{\Phi}$	Matrix of modeshapes of full-order model
$\mathbf{\Phi}_r$	Matrix of reduced modeshapes
$\mathbf{\Phi}_s$	Matrix of statically coupled modeshapes

Higher-rank tensors

$\mathbf{K}^{(2)}$	Rank-3 tensor containing the full-order quadratic stiffness coefficients in the physical space
$\mathbf{K}^{(3)}$	Rank-4 tensor containing the full-order cubic stiffness coefficients in the physical space
$\mathbf{A}^{(n)}$	Rank-$(n+1)$ tensor containing the n^{th}-order stiffness coefficients in the reduced space
$\mathbf{B}^{(n)}$	Rank-$(n+1)$ tensor containing the n^{th}-order quasi-static coupling coefficients

Abbreviations

DOF	Degree Of Freedom
FE	Finite Element
ICE	Implicit Condensation and Expansion
ICE-IC	ICE with Inertial Compensation
ICE-IC-FC	ICE with Inertial Compensation and Force Compensation
LNM	Linear Normal Mode
NNM	Nonlinear Normal Mode
ODE	Ordinary Differential Equation
ROM	Reduced-Order Model

Chapter 1

Introduction

Traditionally, the dynamics of engineering structures have been modelled according to linear vibration theory, and a number of powerful analysis methodologies and tools have been developed based on the concept of *linear normal modes*. However, despite its useful mathematical properties, linear dynamic behaviour is usually an idealised model, which is becoming increasingly inadequate in characterising real-world structural dynamics. With the ever-increasing demand for better performance, modern engineering structures continue to tend towards thin, low-weight and highly flexible designs. This trend, combined with the extreme loading environments in which structures are often required to operate, can lead to large-amplitude vibrations and give rise to *geometric nonlinearity*. Examples of engineering structures experiencing geometric nonlinearity include flexible aircraft wings (Shearer and Cesnik, 2007) and wind turbine blades (Manolas *et al.*, 2015), skin panels of hypersonic aircraft under extreme thermal, aerodynamic and acoustic loads (Blevins *et al.*, 1993; Gordon and Hollkamp, 2011), as well as nano/micro-electromechanical systems (N/MEMS) (Lazarus *et al.*, 2012; Zega *et al.*, 2020) which find use in ultrasensitive mass and force sensors (Rugar *et al.*, 2004; Jensen *et al.*, 2008), radio frequency telecommunication devices (Nguyen, 2007), bit storage systems (Mahboob and Yamaguchi, 2008), and energy harvesting devices (Challa *et al.*, 2008).

Whilst nonlinearity is undeniably a source of additional complexity in the modelling and simulation of dynamical systems, it is not necessarily an undesirable feature that must be avoided. Instead, nonlinearity presents unique opportunities to design structures with enhanced performance and efficiency. To this end, the concept of a *nonlinear normal mode* has been introduced as an extension of its linear coun-

terpart, and has served as a tool for studying and better understanding nonlinear systems. In recent years, new analytical and numerical techniques have been developed based on this concept, which have enabled nonlinear effects to be incorporated in the modelling and simulation of dynamical systems. Nevertheless, the practical implementation of nonlinear dynamic analysis in the design of engineering structures remains a challenge. This is because the applicability of nonlinear methods is typically limited to low-dimensional systems; at the same time, engineering structures are often modelled using finite element (FE) software, where the structure is descretised in space, resulting in very large numbers of degrees-of-freedom. As a result, applying these nonlinear techniques to the full-order FE model is mathematically intractable from an analytical perspective, and often prohibitively computationally expensive, from a numerical perspective.

Reduced-order modelling methods aim to ease this bottleneck, by constructing computationally cheap, low-dimensional models, which capture the salient dynamics of a structure in an efficient manner. By dramatically reducing the computational cost associated with nonlinear dynamic analysis, reduced-order models (ROMs) enable the effective design and optimisation of engineering structures. In addition, ROMs enable the implementation of hybrid testing frameworks, whereby part of the structure is tested experimentally whilst the rest of it is simulated, such that real-time computations are essential.

This thesis aims to further the current state-of-the-art of nonlinear reduced-order modelling, focussing on methods applicable to structures modelled using commercial FE software. The methods proposed herein build on existing techniques, aiming to improve their accuracy, efficiency and robustness, and broaden their applicability to a wider range of structures.

Chapter 2

Background

This chapter lays the foundations for the rest of the thesis. Section 2.1 outlines the effects of geometric nonlinearity in structural dynamics, and introduces the concept of nonlinear normal modes as well as associated techniques, which are suited to the analysis of nonlinear dynamical systems. Section 2.2 introduces the equations of motion of a general, geometrically nonlinear finite element model, which typically forms the starting point in reduced-order modelling frameworks. In section 2.3, the existing literature on reduction methodologies for geometrically nonlinear structures is reviewed. Finally, the scientific contributions of this thesis are outlined in section 2.4.

2.1 Nonlinearity in structural dynamics

2.1.1 Linear normal modes

In classical vibration theory, the concept of a linear normal mode[1] (LNM) provides a powerful tool for understanding and characterising linear dynamical systems. A fundamental feature of LNMs is orthogonality, which essentially allows the equations of motion of the system to be decoupled, such that all modal responses are mutually independent. As a result of mode orthogonality, two important properties of linear systems arise (Rayleigh, 1896; Kerschen *et al.*, 2009):

1. *Invariance*: if a specific mode is excited, the remaining unforced modes remain quiescent for the duration of the system response

[1]The terms *mode* and *linear normal mode* are equivalent and used interchangeably throughout this thesis.

2. *Superposition*: the net response of a system can be expressed as a linear combination of individual modal responses.

Due to the intuitive physical interpretation of LNMs, as well as their useful mathematical properties, several frameworks for analysing linear systems have been developed based on this concept, with a wide range of applications in science and engineering. Examples of such techniques include modal testing (Ewins and Saunders, 1986), statistical energy analysis (Fahy, 1994), modal substructuring (Craig and Bampton, 1968), finite element model updating (Mottershead and Friswell, 1993) and structural health monitoring (Doebling *et al.*, 1996).

2.1.2 Geometric nonlinearity

Geometric nonlinearity arises when structures experience large-amplitude vibrations,[2] and is typically associated with thin and highly flexible structures such as beams, plates and shells. Examples of engineering structures experiencing geometric nonlinearity include flexible aircraft wings (Shearer and Cesnik, 2007) and wind turbine blades (Manolas *et al.*, 2015), skin panels of hypersonic aircraft under extreme thermal, aerodynamic and acoustic loads (Blevins *et al.*, 1993; Gordon and Hollkamp, 2011), as well as nano/micro-electromechanical systems (Lazarus *et al.*, 2012; Zega *et al.*, 2020) which find use in ultrasensitive mass and force sensors (Rugar *et al.*, 2004; Jensen *et al.*, 2008), radio frequency telecommunication devices (Nguyen, 2007), bit storage systems (Mahboob and Yamaguchi, 2008), and energy harvesting devices (Challa *et al.*, 2008).

When nonlinearities are present in a system, an orthogonal modal basis does not generally exist. This is because the underlying linear modes are coupled to one another through the nonlinear terms, such that the invariance and superposition properties are no longer applicable. Instead, nonlinear systems possess new distinct dynamical features, most notably *frequency-energy dependence*, *bifurcations* and *instabilities*, all of which are concepts that have no linear counterparts. As a result of the modal couplings, nonlinear systems can exhibit a number of complex behaviours; examples of such nonlinear phenomena include:

- the co-existence of multiple stable equilibria and the sudden transitions (“jumps") between them (Nayfeh and Mook, 1995; Brennan *et al.*, 2008);

[2] It should be noted that other sources of nonlinearity exist, e.g. material nonlinearity and localised nonlinearities due to joints. These are beyond the scope of this thesis.

- limit cycle oscillations (Patil *et al.*, 2001; Thothadri and Moon, 2005);
- mode localisation, i.e. the spatial confinement of free periodic motions in a region of the structure near the source of excitation (Bendiksen, 1987);
- internal resonance, whereby exchange of energy takes place between modes whose nonlinear response frequencies are commensurate (Nayfeh and Mook, 1995; Sayed and Kamel, 2012).

Whilst nonlinear behaviour is often associated with *dynamic* modal interactions, a specific type of modal coupling that is particularly prominent in structural dynamics, is *quasi-static* coupling. This means that, even though the underlying linear normal modes are coupled together, they do not necessarily act as independent degrees-of-freedom; instead, it is assumed that the response of a mode may be approximated as a function of the response of a different mode or set of modes. This type of coupling is often seen in structures characterised by slow/fast dynamics, such as thin plates and slender beams, where the high-frequency in-plane modes are approximately quasi-statically coupled to a small set of low-frequency transverse modes; this effect is often referred to as *membrane stretching* (Mignolet *et al.*, 2013). Quasi-static coupling forms the basis for a number of reduced-order modelling methodologies, and will be considered extensively throughout this thesis.

2.1.3 Nonlinear normal modes

The fundamentally distinct nature of nonlinear systems renders traditional analysis techniques suboptimal at best, and often altogether inapplicable. As a first step towards addressing the lack of tools suited to nonlinear behaviours, the concept of a *nonlinear normal mode* (NNM) was pioneered by Rosenberg (1960, 1962, 1966). Conceptually, NNMs are analogous to the well-established LNMs from classical vibration theory, which practising structural dynamicists use and are familiar with. Even though they do not possess many of the appealing mathematical properties of their linear counterparts, NNMs offer a rigorous theoretical tool for analysing and interpreting phenomena which cannot be captured by linear theory.

The simplest definition of an NNM of a conservative (i.e. unforced and undamped) system, stemming from the work of Rosenberg (1960), is a *vibration in-unison*, i.e. a synchronous periodic oscllation, where all displacement coordinates of the system are always in-phase or in anti-phase. As such, all physical displacements can be expressed in terms of a single reference coordinate by means of a modal function, while

velocities can be computed by considering conservation of energy during the motion. This concept was further explored by Pak and Rosenberg (1968), Rand (1971, 1974) and Manevich and Mikhlin (1972), who used geometrical/analytical techniques to establish the existence of, and derive expressions for, NNMs of conservative nonlinear systems. Nonlinear normal modes received renewed attention and significance in the 1990s, following the seminal work of Vakakis *et al.* (1990, 1992, 1994, 1996, 1997) and Shaw and Pierre (1991, 1992, 1993, 1994), who used analytical methods, and in some cases numerical integration, to study phenomena such as bifurcations, stability and localisation in nonlinear systems. The latter authors also introduced a new problem formulation that utilises the theory of invariant manifolds for dynamical systems, as opposed to Rosenberg's original energy-based formulation. This allows for the inclusion of physical velocities as independent variables, such that the concept of NNMs can be extended to nonconservative systems (Shaw and Pierre, 1991, 1993). To this end, the concept of a spectral submanifold defined as the smoothest nonlinear continuation of the spectral subspace of the linearised system, has recently been introduced, with the aim of proving the existence and uniqueness of such subspaces for dissipative systems (Haller and Ponsioen, 2016; de la Llave and Kogelbauer, 2019).

Nonlinear normal modes have been successfully employed in a large number of studies addressing the analysis of nonlinear phenomena, most of which are based on asymptotic approaches. Some of the analytical techniques that have received considerable attention in the context of NNM computation include the method of averaging (Sanders *et al.*, 2007; Gonzalez-Buelga *et al.*, 2008), the method of multiple scales (Nayfeh, 1981; Wagg and Neild, 2015), the harmonic balance method (Nayfeh and Mook, 1995; Petrov and Ewins, 2003), and the method of normal forms (Jezequel and Lamarque, 1991; Touzé *et al.*, 2004a; Neild *et al.*, 2015).

Recently, Rosenberg's definition of an NNM has been extended to include any, not necessarily synchronous, periodic motion of the conservative nonlinear system (Kerschen *et al.*, 2009; Peeters *et al.*, 2009). This definition becomes particularly attractive when considering systems in the presence of internal resonance, where out-of-unison (Hill *et al.*, 2015) or phase-varying (Hong *et al.*, 2020) periodic motions may occur. Through this more recent definition, the concept of NNMs has become associated with numerical, rather than analytical, techniques, as it enables the computation of NNMs using algorithms for the *continuation* of periodic solutions (Kerschen *et al.*, 2009; Hill, 2016).

Numerical continuation is a method of computing parametrically-defined manifolds. In the context of analysing smooth dynamical systems, these manifolds are defined by a finite number of ordinary differential equations, which can describe either discrete systems, or discrete approximations of continuous systems. The method relies on the assumption that, as a parameter in the equations of motion varies continuously, so does the solution. Based on this, a new solution, which corresponds to a sufficiently small change in a system parameter, can be found in the vicinity of a known solution, and the locus of the solution manifold is traced sequentially as such. The initial solution required for this approach can often be obtained by considering the modes of the underlying linear system, which, at sufficiently low energy levels, approximate the NNMs (Peeters *et al.*, 2009; Allen *et al.*, 2012). As the steady-state solutions are sought directly, numerical continuation allows for more efficient computations compared to the direct numerical integration of the equations of motion, particularly for weakly-damped systems, where transient settling times can be large. In addition, it enables the computation of multiple (including unstable) steady-state solutions which would otherwise not be found, thus providing a better insight into the behaviour of the system.

2.2 Finite element models

The finite element method is a powerful, versatile and extremely popular technique for modelling structures, and sees widespread use by dynamicists in the engineering industry and academia alike (Reddy, 1993; Bathe, 2006). FE procedures involve the discretisation of structures in space, enabling the accurate representation of complex geometries and inclusion of nonlinear effects. The resulting semi-discretised equations of motion of the structure take the form of second-order ordinary differential equations in terms of the $N \times 1$ time-dependent vector of generalised coordinates $\mathbf{x}(t)$, representing the displacements and/or rotations at each node, where N is the number of DOFs of the model. For a linearly elastic structure, these are written as

$$\mathbf{M}\ddot{\mathbf{x}} + \mathbf{K}\mathbf{x} + \mathbf{f}(\mathbf{x}) = \mathbf{F}, \tag{2.1}$$

where $\mathbf{M}$ and $\mathbf{K}$ are the $N \times N$ linear mass and stiffness matrices, respectively, $\mathbf{f}(\mathbf{x})$ is the $N \times 1$ vector of nonlinear internal restoring forces, and $\mathbf{F}$ is the $N \times 1$ vector of

external forces acting on the structure.[3] Typically, it is assumed that the nonlinear restoring forces take the form of quadratic and cubic polynomial functions of the generalised coordinates (Lazarus *et al.*, 2012; Mignolet *et al.*, 2013), i.e.

$$\mathbf{f}(\mathbf{x}) = \mathbf{K}^{(2)}\mathbf{x}\mathbf{x} + \mathbf{K}^{(3)}\mathbf{x}\mathbf{x}\mathbf{x}, \tag{2.2}$$

where $\mathbf{K}^{(2)}$ and $\mathbf{K}^{(3)}$ are tensors[4] of rank 3 and 4, respectively, characterising the geometric nonlinearity of the structure. This formulation is mathematically exact when the model is discretised using 3D elements or 2D elements under the von Kármán kinematic assumption, which states that the axial strain and curvature are small relative to the transverse deflection, such that strain can be expressed as a quadratic function of displacement (Thomas and Bilbao, 2008). In the case of geometrically exact beam elements, equation (2.2) is a truncated approximation that is accurate up to moderate amplitudes (Thomas *et al.*, 2016; Givois *et al.*, 2019).

It is worth noting that the tensors $\mathbf{K}^{(2)}$ and $\mathbf{K}^{(3)}$, which contain N^3 and N^4 elements, respectively, can pose a significant computational burden and memory requirements for very large FE models. In practice, and particularly in commercial FE software, these coefficients are rarely computed explicitly, but instead the internal forces are computed in an iterative manner.

For reduction purposes, it is often useful to consider the FE model in its modal space, where the modal coordinates, $\mathbf{q}$, are linearly uncoupled. This can be achieved using the linear transform

$$\mathbf{x} = \boldsymbol{\Phi}\mathbf{q}, \tag{2.3}$$

where $\boldsymbol{\Phi}$ is the $N \times N$ matrix of mass-normalised modeshapes, such that

$$\boldsymbol{\Phi}^{\mathsf{T}}\mathbf{M}\boldsymbol{\Phi} = \mathbf{I}, \tag{2.4a}$$

$$\boldsymbol{\Phi}^{\mathsf{T}}\mathbf{K}\boldsymbol{\Phi} = \boldsymbol{\Lambda}, \tag{2.4b}$$

where $\boldsymbol{\Lambda}$ is the $N \times N$ diagonal matrix containing the squares of the corresponding natural frequencies, and $\mathbf{I}$ is the identity matrix. The n^{th} column in $\boldsymbol{\Phi}$, $\boldsymbol{\phi}_n$, and the n^{th} value along the leading diagonal of $\boldsymbol{\Lambda}$, ω_n^2, are the eigenvector and eigenvalue, respectively, which satisfy

$$\left(\mathbf{K} - \omega_n^2\mathbf{M}\right)\boldsymbol{\phi}_n = \mathbf{0}. \tag{2.5}$$

[3] Note that, in general, the external forces may be displacement-dependent (e.g. follower forces) and/or velocity-dependent (e.g. aerodynamic drag). Here, it is assumed that $\mathbf{F} = \mathbf{F}(t)$ for the sake of simplicity, but the more general case of $\mathbf{F} = \mathbf{F}(t, \mathbf{x}, \dot{\mathbf{x}})$ is considered later in Chapter 6.

[4] Here, the term *tensor* refers to a multidimensional array of dimension, or *rank*, greater than two. Scalars, vectors, and matrices may be considered as arrays of rank 0, 1, and 2, respectively.

Substituting equation (2.3) into equation (2.1) and premultiplying by $\boldsymbol{\Phi}^\top$ leads to

$$\ddot{\mathbf{q}} + \boldsymbol{\Lambda}\mathbf{q} + \mathbf{f}_q(\mathbf{q}) = \mathbf{F}_q, \tag{2.6}$$

where

$$\mathbf{f}_q(\mathbf{q}) = \boldsymbol{\Phi}^\top \mathbf{f}(\boldsymbol{\Phi}\mathbf{q}) = \boldsymbol{\Lambda}^{(2)}\mathbf{q}\mathbf{q} + \boldsymbol{\Lambda}^{(3)}\mathbf{q}\mathbf{q}\mathbf{q}, \tag{2.7a}$$

$$\mathbf{F}_q = \boldsymbol{\Phi}^\top \mathbf{F} \tag{2.7b}$$

are the vectors of nonlinear internal forces and external forces in the modal space, respectively, and $\boldsymbol{\Lambda}^{(2)}$ and $\boldsymbol{\Lambda}^{(3)}$ are tensors of rank 3 and 4, respectively.

2.3 Reduced-order modelling

There exists a vast body of literature devoted to reduced-order modelling of geometrically nonlinear dynamical systems (Mignolet *et al.*, 2013; Touzé *et al.*, 2021), with different methodologies often having overlapping characteristics, and sometimes conflicting terminology. In this thesis, reduced-order modelling methods are divided into two broad classes:

1. *Intrusive* or *direct* methods: these methods rely on manipulation of the coefficients of the full-order equations of motion, or a subset thereof, in order to compute the ROM parameters. They are typically seen in academic applications, where in-house or open-source FE codes are employed.
2. *Non-intrusive* or *indirect* methods: these methods do not require knowledge of the exact equations of motion of the full-order model. They are well-suited to industrial applications, which utilise commercial FE software, where the full-order nonlinear stiffness coefficients are inaccessible.

In the following subsections, we review both intrusive and non-intrusive model order reduction methods used in structural dynamics, with special emphasis on the latter, which is the focus of this thesis.

2.3.1 Intrusive methods

The category of direct reduced-order modelling methods includes any approach which requires knowledge of the equations of motion of the full-order model. For linearly elastic FE models, this requires access to the stiffness tensors which contain

the coefficients of the quadratic and cubic monomials characterising the geometric nonlinearity, in addition to the linear mass and stiffness matrices.

Early works have focussed on modal reduction methods, originally developed for linear dynamics, in which the number of DOFs is reduced through a Galerkin projection onto a subset of the linear normal modes of the FE model (Nash, 1977; Mei and Moorthy, 1995; Shi and Mei, 1996; Przekop *et al.*, 2004a,b). Due to the coupling between modes, i.e. the membrane stretching induced by finite deflections/rotations in thin plates or slender beams, typically a large number of modes must be included in the reduction basis in order to accurately capture the nonlinear response. Additionally, a major drawback of such methods is that the number and type of modes needed to describe the response of the structure vary as the response amplitude increases, requiring that the reduction basis be updated during time integration (Jacob and Ebecken, 1992).

These issues stem from the fact that the eigenproblem characterising the nonlinear model is configuration-dependent; the LNMs are precisely the solution of this problem at zero displacement, but they diverge from it as the amplitude increases. In this context, *modal derivatives* have been introduced as the second-order approximation of the state-dependent modes (Idelsohn and Cardona, 1985b,a). Modal derivatives can be obtained by differentiating the nonlinear eigenproblem with respect to the modal coordinates (Slaats *et al.*, 1995), thus requiring knowledge of the exact form of the nonlinearities in the equations of motion.[5] The inertia of the model may sometimes be neglected during this process, yielding so-called *static* modal derivatives (Jain *et al.*, 2017). Several contributions have shown that the effects of the coupling between modes can be effectively accounted for by including (static) modal derivatives in the reduction basis, in addition to the dynamically important LNMs. Examples of structures for which modal derivatives have been successfully employed during model order reduction include flat and arched clamped-clamped beams and cantilever plates (Tiso *et al.*, 2011; Wu and Tiso, 2016; Sombroek *et al.*, 2018). Since the number of modal derivatives grows quadratically with respect to the number of retained modes, a drawback of this approach is that the size of the reduction basis increases quickly, thus limiting the applicability of this method to relatively simple structures. To alleviate this burden, several heuristic methods for

[5] Modal derivatives may also be approximated in a non-intrusive manner using finite difference schemes in conjunction with commercial FE software; however, this can lead to significant numerical errors if the step size is not carefully tuned (Rutzmoser, 2018).

ranking and selecting the most relevant modal derivatives have been proposed (Tiso, 2011; Rutzmoser, 2018).

Alternatively, the concept of a *quadratic manifold* has been proposed as a method of constraining the amplitude of the modal derivatives to that of the LNMs, rather than treating them as independent DOFs (Jain *et al.*, 2017). As such, reduction is achieved through a nonlinear transform consisting of a linear and a quadratic part, whose coefficients are made up of LNMs and modal derivatives, respectively. This method was found to work remarkably well for thin-walled structures characterised by von Kármán kinematics, where the quadratic enslavement of the in-plane modes to the transverse modes is exact. However, poor results can be obtained when this assumption is not valid, as has been demonstrated using a cantilever beam in Rutzmoser *et al.* (2017). This suggests that, generally, a projection onto a higher-order manifold (i.e. higher than quadratic) might be necessary to accurately capture the nonlinear behaviour of the structure.

A similar but more general concept which has been utilised for reduced-order modelling, is that of nonlinear normal modes defined as *invariant manifolds* in phase space (Shaw and Pierre, 1991, 1993, 1994). The fundamental idea underpinning NNMs is that, through a nonlinear transform, the system can be defined in terms of a set of invariant, *normal coordinates*. In this framework, each displacement–velocity pair of normal coordinates defines an NNM, and includes the effects of all the underlying LNMs (Pesheck, 2000). As such, ROMs can be realised by retaining the normal coordinates associated with NNMs whose linearised natural frequencies lie in the bandwidth of interest, whilst all other coordinates can be neglected without introducing error in the process; this may be considered as the nonlinear counterpart of modal truncation methods used in linear dynamics. In its asymptotic formulation, the nonlinear transform applied to each modal coordinate of the full-order FE model, takes the form of a polynomial function spanning the reduced states (Touzé *et al.*, 2004b, 2008). Analytical expressions for the newly introduced coefficients can be derived by substituting the transform into the full-order equations of motion and equating the coefficients of like monomial terms; the dynamics of the reduced coordinates can then be expressed as a function of the coefficients of the FE model. Reduced-order modelling based on invariant manifolds has been demonstrated for a range of structures, including beams (Touzé *et al.*, 2004a,b; Vizzaccaro *et al.*, 2020) and cylindrical and spherical shells (Touzé and Amabili, 2006; Touzé and Thomas, 2006).

Whilst this method provides a powerful tool for generating accurate ROMs with the fewest possible time-dependent variables, it does come with a major drawback associated with the asymptotic nature of the nonlinear change of coordinates, in addition to being intrusive. As noted in Touzé *et al.* (2004b), the accuracy of the results can deteriorate quite rapidly in strongly nonlinear regimes, where higher orders of nonlinearity need to be considered, thus compromising the reliability of the ROM. At the same time, due to the analytical and mathematically involved nature of the method, calculations quickly become onerous when considering truncations beyond cubic.

More recently, a new formulation of a reduced-order modelling methodology based on normal form theory has been proposed, whereby the *physical* (rather than modal) coordinates are directly mapped into the normal coordinates; this is referred to as *direct normal form* (Vizzaccaro *et al.*, 2021; Opreni *et al.*, 2021). This approach has the advantage of not requiring a full linear modal transform, which can be a bottleneck when considering very large FE models. This framework considers an arbitrary order of expansion (Vizzaccaro *et al.*, 2022), the presence of damping and external forcing (Vizzaccaro *et al.*, 2021), following the work of Touzé *et al.* (2004a, 2006), as well as the proper treatment of internal resonances; the latter has been demonstrated using a MEMS arch resonator exhibiting a 1:2 internal resonance (Opreni *et al.*, 2021). Nevertheless, the direct normal form approach requires knowledge of a subset of the nonlinear coefficients of the full-order model. As a result, whilst it is theoretically possible for the method to be applied to FE models built using commercial software, this must be preceded by an identification process, using for example the stiffness evaluation procedure (Muravyov and Rizzi, 2003; Perez *et al.*, 2014), which is discussed in the following subsection. In addition, such a non-intrusive implementation of the direct normal form method is only feasible for nonlinear mappings up to the cubic order, beyond which the calculations become intractable.

2.3.2 Non-intrusive methods

Indirect reduced-order modelling methods do not require access to the inner workings of the FE code or knowledge of the nonlinear coefficients in the full-order equations of motion, i.e. $\mathbf{K}^{(2)}$ and $\mathbf{K}^{(3)}$ in the physical space, or $\mathbf{\Lambda}^{(2)}$ and $\mathbf{\Lambda}^{(3)}$ in the modal space. Instead, the two pieces of information that must be extracted from the FE model are:

1. its linear properties, i.e. the mass (**M**) and stiffness (**K**) matrices, typically obtained through a linear perturbation procedure;
2. a set of nonlinear static solutions, typically obtained using an iterative procedure such as the Newton-Raphson method.

Both of the above are standard features in commercial FE software such as Nastran (MSC Software Corporation, 2003) and Abaqus (Dassault Systèmes, 2017).

In this class of methods, it is assumed that the dynamics of the full-order model can be approximated by a small subset of its linear normal modes, whilst the remaining modes can be neglected (Mignolet *et al.*, 2013). The modeshapes corresponding to the retained modes are compiled in the $N \times R$ matrix $\mathbf{\Phi}_r$, which forms the *reduction basis*, where $R \ll N$ is the number of DOFs of the reduced-order model. The equations of motion of the FE model are reduced using the *linear transform*

$$\mathbf{x} = \mathbf{\Phi}_r \mathbf{r}, \tag{2.8}$$

where $\mathbf{r}$ is the $R \times 1$ vector of reduced coordinates. Substituting this into equation (2.1) and premultiplying by $\mathbf{\Phi}_r^\intercal$ leads to the reduced equations of motion, written as

$$\ddot{\mathbf{r}} + \mathbf{\Lambda}_r \mathbf{r} + \mathbf{f}_r(\mathbf{r}) = \mathbf{\Phi}_r^\intercal \mathbf{F}, \tag{2.9}$$

where $\mathbf{\Lambda}_r = \mathbf{\Phi}_r^\intercal \mathbf{\Lambda} \mathbf{\Phi}_r$ is the $R \times R$ diagonal matrix containing the squares of the natural frequencies of the reduced modes, and $\mathbf{f}_r(\mathbf{r})$ is the $R \times 1$ vector of nonlinear internal restoring forces in the reduced space. The latter is given by

$$\mathbf{f}_r(\mathbf{r}) = \mathbf{\Phi}_r^\intercal \mathbf{f}(\mathbf{\Phi}_r \mathbf{r}) = \mathbf{A}^{(2)}\mathbf{r}\mathbf{r} + \mathbf{A}^{(3)}\mathbf{r}\mathbf{r}\mathbf{r}, \tag{2.10}$$

where $\mathbf{A}^{(2)}$ and $\mathbf{A}^{(3)}$ are tensors of rank 3 and 4, containing the quadratic and cubic coefficients of the ROM, respectively. In index notation, the i^{th} component in $\mathbf{f}_r$ is written

$$\mathrm{f}_{r,i} = \sum_{j=1}^{R}\sum_{k=1}^{R} A^{(2)}_{ijk}\mathrm{r}_j\mathrm{r}_k + \sum_{j=1}^{R}\sum_{k=1}^{R}\sum_{l=1}^{R} A^{(3)}_{ijkl}\mathrm{r}_j\mathrm{r}_k\mathrm{r}_l. \tag{2.11}$$

Since the full-order nonlinear coefficients cannot be used in estimating the ROM coefficients, these must be computed in an indirect manner. This is achieved via linear regression, typically in a least-squares manner, using a set of nonlinear static solutions of the FE model.

There exist two variations of indirect methods, which differ in how the static solution dataset is obtained. In the *displacement-based* approach, which is often

referred to as the enforced displacement procedure or stiffness evaluation procedure (STEP), the structure is constrained into a prescribed shape, $\mathbf{x}_{\text{st}}$, and the resulting reaction forces needed to hold that shape, $\mathbf{F}_{\text{st}}$, are extracted (Muravyov and Rizzi, 2003; Rizzi and Przekop, 2005; Perez *et al.*, 2014). For each static load case, the displacement imposed on the structure is a linear combination of the basis functions, i.e.

$$\mathbf{x}_{\text{st}} = \boldsymbol{\Phi}_r \boldsymbol{\kappa}_{\text{disp}}, \tag{2.12}$$

where $\boldsymbol{\kappa}_{\text{disp}}$ is an $R \times 1$ vector of displacement scale factors, typically containing up to three non-zero components, and is equivalent to the static displacement in the reduced modes, i.e. $\mathbf{r}_{\text{st}} \equiv \boldsymbol{\kappa}_{\text{disp}}$. The resulting reaction forces are extracted from the FE model using a standard nonlinear static solver, and the vector of nonlinear restoring forces in the reduced modes is computed as

$$\mathbf{f}_{r,\text{st}} = \boldsymbol{\Phi}_r^{\mathsf{T}} \mathbf{F}_{\text{st}} - \boldsymbol{\Lambda}_r \mathbf{r}_{\text{st}}. \tag{2.13}$$

Finally, the nonlinear coefficients in the ROM, $\mathbf{A}^{(2)}$ and $\mathbf{A}^{(3)}$, are estimated by fitting quadratic and cubic polynomial functions to the static solution dataset, $\{\mathbf{f}_{r,\text{st}}, \mathbf{r}_{\text{st}}\}$, as expressed in equations (2.10) and (2.11). The displacement-based approach has been used in a number of different studies involving beam and plate structures — see for example Mignolet and Soize (2008); Lazarus *et al.* (2012); Kim *et al.* (2013); Givois *et al.* (2019).

In the force-based variation of indirect methods, which is commonly referred to as the applied loads method or implicit condensation[6] (IC), a static force, $\mathbf{F}_{\text{st}}$, is applied to the structure, and the resulting displacement, $\mathbf{x}_{\text{st}}$, is extracted (Segalman and Dohrmann, 1996; McEwan *et al.*, 2001; Hollkamp and Gordon, 2008; Gordon and Hollkamp, 2011). The shape of the applied force is a linear combination of the reduced modeshapes, i.e.

$$\mathbf{F}_{\text{st}} = \mathbf{M}\boldsymbol{\Phi}_r \boldsymbol{\kappa}_{\text{force}}, \tag{2.14}$$

where $\boldsymbol{\kappa}_{\text{force}}$ is an $R \times 1$ vector of force scale factors, which is equivalent to the forces applied to the reduced modes. The resulting displacement vector is extracted using a nonlinear static solver, and the reduced static displacements are computed as

$$\mathbf{r}_{\text{st}} = \boldsymbol{\Phi}_r^{\mathsf{T}} \mathbf{M} \mathbf{x}_{\text{st}}. \tag{2.15}$$

[6]The term *condensation* refers to the elimination of a set of modes, by capturing their effects within the dynamics of the remaining coordinates.

The reduced nonlinear restoring forces are computed using equation (2.13), and the nonlinear ROM coefficients are estimated using the $\{\mathbf{f}_{r,\mathrm{st}}, \mathbf{r}_{\mathrm{st}}\}$ dataset, as with the displacement-based approach. Examples of structures for which the force-based method has been applied include clamped beams and plates for aeronautic (Hollkamp *et al.*, 2005; Gordon and Hollkamp, 2011; Kuether *et al.*, 2015) and MEMS applications (Frangi and Gobat, 2019). The procedure for constructing ROMs using indirect methods is summarised in table 2.1, both for the displacement-based and force-based variations.

It is worth noting that the number of nonlinear coefficients that must be estimated can be reduced by enforcing linear dependencies between elements of $\mathbf{A}^{(2)}$ and $\mathbf{A}^{(3)}$, such that symmetry is preserved, and the resulting equations of motion are consistent with an underlying elastic potential energy function — see Touzé *et al.* (2021); Gordon and Hollkamp (2011) for further details. Reduced-order models constructed using this approach, which is sometimes referred to as *constrained* IC, were found to be more stable during time integration compared with their unconstrained counterparts (Gordon and Hollkamp, 2011).

Table 2.1. Outline of the ROM generation procedure for indirect reduction methods.

	Displacement-based method (e.g. STEP)	Force-based method (e.g. IC)
→ Extract the mass matrix, $\mathbf{M}$, and linear stiffness matrix, $\mathbf{K}$, of the FE model.		
→ Select the reduction basis, $\boldsymbol{\Phi}_r$; compute the linear reduced coefficients, $\boldsymbol{\Lambda}_r$.		
→ Repeat for each load case:		
a)	Select disp. scale factors, κ_{disp}.	Select force scale factors, κ_{force}.
b)	Enforce structure into static shape, $\mathbf{x}_{\mathrm{st}} = \boldsymbol{\Phi}_r \kappa_{\mathrm{disp}}$.	Apply static force to structure, $\mathbf{F}_{\mathrm{st}} = \mathbf{M}\boldsymbol{\Phi}_r \kappa_{\mathrm{force}}$.
c)	Extract resulting reaction forces, $\mathbf{F}_{\mathrm{st}}$.	Extract resulting displacement, $\mathbf{x}_{\mathrm{st}}$.
d)	Compute displacement and nonlinear force data in the reduced modal space, $\mathbf{r}_{\mathrm{st}} = \kappa_{\mathrm{disp}}$ and $\mathbf{f}_{r,\mathrm{st}} = \boldsymbol{\Phi}_r^{\intercal}\mathbf{F}_{\mathrm{st}} - \boldsymbol{\Lambda}_r \kappa_{\mathrm{disp}}$.	Compute displacement and nonlinear force data in the reduced modal space, $\mathbf{r}_{\mathrm{st}} = \boldsymbol{\Phi}_r^{\intercal}\mathbf{M}\mathbf{x}_{\mathrm{st}}$ and $\mathbf{f}_{r,\mathrm{st}} = \kappa_{\mathrm{force}} - \boldsymbol{\Lambda}_r \mathbf{r}_{\mathrm{st}}$.
→ Estimate the nonlinear ROM coefficients, $\mathbf{A}^{(2)}$ and $\mathbf{A}^{(3)}$, by fitting quadratic and cubic polynomial functions to the $\{\mathbf{f}_{r,\mathrm{st}}, \mathbf{r}_{\mathrm{st}}\}$ dataset (see equation (2.10)).		

Despite the similarities between displacement-based and force-based indirect reduction methods, several important differences have been noted. Firstly, the displacement-based approach is fundamentally an *identification* process, i.e. the estimated ROM parameters approximate the *true parameters* of the full-order model that correspond to the reduced modes (Tartaruga *et al.*, 2019). In other words, a ROM constructed using this approach is equivalent to the ROM that would be obtained through a linear projection onto the reduced modeshapes, i.e. using equation (2.8), if the full-order coefficients were known. As a result, the estimated ROM parameters are largely *insensitive to the displacement scale factors* used to obtain the static solution dataset, as long as:

1. the displacement amplitudes are large enough to excite non-negligible amounts of geometric nonlinearity, in order to circumvent numerical errors;

2. the displacement amplitudes are not *extremely* large so as to invalidate equation (2.2), in which case, higher-order nonlinear terms would need to be included in the dynamics of the FE model (Givois *et al.*, 2019; Tartaruga *et al.*, 2019).

The main drawback of the displacement-based approach lies in the fact that, when only the low-frequency, dynamically important modes are included in the reduction basis, the ROM fails to capture the effect of membrane stretching, resulting in overly stiff behaviour (Shi and Mei, 1996; Mignolet *et al.*, 2013; Tartaruga *et al.*, 2019). To account for the induced in-plane motions, a number of membrane modes whose natural frequencies lie well beyond the bandwidth of interest, must be explicitly included in the reduction basis (Rizzi and Przekop, 2008; Kuether *et al.*, 2015). Similarly, other strategies aim to capture the effect of membrane stretching by augmenting the reduction basis with the so-called *dual* or *companion* modes, which are generated using a set of nonlinear static or dynamic solutions of the FE model (Hollkamp *et al.*, 2003, 2005; Przekop and Rizzi, 2006; Wang *et al.*, 2009; Kim *et al.*, 2013). As a result, not only is the identification of the relevant membrane/dual/companion modes a cumbersome procedure, but the reduction basis becomes relatively large, thus limiting the computational savings.

On the other hand, force-based indirect reduction methods do not aim to recover the true coefficients of the full-order model. Instead, the reduced dynamics obtained using this approach, lie on a distinct subspace in which the unmodelled modes are *im-*

plicitly condensed;[7] this subspace is sometimes referred to as *stress manifold* (Frangi and Gobat, 2019). In other words, by applying a static force in the shape of the reduced modeshapes, rather than enforcing a modal displacement, the unmodelled modes are excited through the nonlinear coupling terms, and the effect of membrane stretching is encoded implicitly within the stress manifold (Gordon and Hollkamp, 2011; Mignolet *et al.*, 2013). The condensation of the in-plane modes into the transverse motions is realised by assuming that in-plane inertia may be neglected, supported by the fact that the natural frequencies of in-plane modes are significantly larger than those of the transverse modes (Mignolet *et al.*, 2013). As a result, the in-plane modes need not be included as independent DOFs in the reduction basis; instead, the reduction basis can be constructed with only a few low-frequency transverse modes, resulting in more efficient ROMs, relative to their displacement-based counterparts.

In some cases, the response of the in-plane modes is reconstructed in a post-processing step, by approximating the in-plane displacements as quadratic functions of the reduced coordinates (Hollkamp and Gordon, 2008; Kuether *et al.*, 2015), i.e.

$$\mathbf{s} \approx \mathbf{g}(\mathbf{r}) = \mathbf{B}\mathbf{r}\mathbf{r}, \tag{2.16}$$

where $\mathbf{s}$ is the $S \times 1$ vector containing the coordinates of the statically coupled modes, S is the number of statically coupled modes of interest, and $\mathbf{g}$ is a vector of *quasi-static coupling functions*. The quadratic coupling coefficients contained in the rank-3 tensor $\mathbf{B}$, are approximated via regression analysis, using the same static solution dataset that is used to approximate the stress manifold. In this case, the dataset is projected into the $\{\mathbf{s}_{\text{st}}, \mathbf{r}_{\text{st}}\}$ space, where $\mathbf{s}_{\text{st}} = \boldsymbol{\Phi}_s^{\intercal}\mathbf{M}\mathbf{x}_{\text{st}}$ is the static displacement of the condensed modes, and $\boldsymbol{\Phi}_s$ is the $N \times S$ matrix containing the condensed modeshapes in its columns. Then, the quasi-static coupling functions may be used to better approximate the response of the full-order model, i.e.

$$\mathbf{x} \approx \boldsymbol{\Phi}_r\mathbf{r} + \boldsymbol{\Phi}_s\mathbf{g}(\mathbf{r}). \tag{2.17}$$

This extended version of IC is referred to as *implicit condensation and expansion* (ICE) (Hollkamp and Gordon, 2008).

Nevertheless, a major drawback of force-based methods such as the ICE, is that the quality of the ROM is greatly dependent on the choice of force scale factors used to

[7] The term *implicit* condensation refers to the non-intrusive counterpart of *static* condensation (Mignolet *et al.*, 2013), with the latter achieved through direct manipulation of the coefficients of the full-order model.

obtain the static solution dataset. As such, scale factors are often chosen on an *ad hoc* basis guided by empirical rules which predict the combinations of forces necessary to exercise a "sufficient" amount of geometric nonlinearity, which often involves a trial and error process (Gordon and Hollkamp, 2011; Kuether *et al.*, 2015).

2.4 Thesis contributions and outline

This thesis aims to improve on the current state-of-the-art of reduced-order modelling techniques for geometrically nonlinear dynamic structures modelled using commercial finite element software. Specifically, the scientific contributions and outline of the thesis are as follows:

Chapter 3: Accounting for quasi-static coupling (Nicolaidou *et al.*, 2020b)
This chapter explores the quasi-static coupling between low- and high-frequency modes in geometrically nonlinear dynamical systems, using a 2-DOF oscillator. As discussed in section 2.3.2, force-based indirect reduction methods, such as the ICE, can implicitly capture the response of the statically coupled modes within the stress manifold; however, the resulting ROMs are sensitive to the scaling of the static solution dataset used to calibrate them, which can lead to significantly inaccurate response predictions if the relevant scaling factors are not carefully tuned. It is demonstrated that the lack of invariance of the ROMs is a result of quasi-static coupling, which introduces higher-order nonlinear terms in the reduced dynamics, compared to the order of nonlinearity in the full-order model. Novel ROMs, with higher-order nonlinear terms, are then shown to be more accurate, and significantly more robust to scaling of the calibration dataset, compared to the traditional cubic ROMs. The robustness of these novel ROMs is further demonstrated using an FE model of a clamped-clamped beam.

Chapter 4: Capturing in-plane inertia (Nicolaidou *et al.*, 2020a)
The applicability of the ICE method, regardless of whether higher orders of nonlinearity are included in the reduced dynamics, is limited to structures which undergo small in-plane displacements, such as the clamped-clamped beam considered in Chapter 3. It is shown that this limitation arises from the fact that, in the traditional approach, the kinetic energy of the condensed in-plane modes is assumed to be negligible. For structures such as plates and beams with fixed/pinned boundary conditions, this is often reasonable, but in structures with free boundary conditions (e.g. cantilever

beams), this assumption is violated. This chapter bridges the gap between direct and indirect reduction methods, by exploiting the concept of nonlinear manifolds to show how in-plane kinetic energy can be accounted for in a non-intrusive manner. This new insight enables indirect reduction methods to be applied to a far wider range of structures while maintaining accuracy to higher deflection amplitudes. The accuracy of the proposed method is validated using an FE model of a cantilever beam.

Chapter 5: Detecting internal resonances (Nicolaidou *et al.*, 2021)
Chapters 3 and 4 consider how, for a given reduction basis, a nonlinear system may be reduced based on a static condensation. Nevertheless, selecting an appropriate reduction basis without *a priori* knowledge of the full-order dynamics remains a challenge. Retaining redundant modes will lead to computationally suboptimal ROMs, whilst omitting dynamically significant modes will lead to inaccurate results, and important features such as internal resonances may not be captured. This chapter demonstrates how the error associated with the static condensation approximation can be efficiently estimated during model order reduction. This approximate error can then be used as the basis of a method for predicting when dynamic modal interactions will occur, which will guide the reduction basis selection process. Equivalently, this may serve as a tool for verifying the accuracy of ROMs without the need for full-order simulations. The proposed method is demonstrated using a simple oscillator and an FE model of a clamped-clamped beam, for which it predicts the existence of a 1:3 and a 1:5 internal resonance, respectively.

Chapter 6: Nonconservative structures (Nicolaidou *et al.*, 2022)
In Chapters 3–5, the quality of the computed ROMs is assessed using backbone curves, i.e. based on the response of the underlying conservative structure. Whilst backbone curves provide invaluable insight into the nonlinear behaviour of the structure and are closely related to forced response curves, it is often useful to compute forced response curves directly. This chapter demonstrates how indirect reduced-order modelling techniques can be extended to nonconservative structures, using a nonlinear mapping of the physical DOFs into the reduced coordinates. The proposed method is contrasted with the traditional approach, which relies on a linear projection of the nonconservative forces onto the reduced subspace; as a result, only the forces acting directly on the reduced modes can be captured, whilst any energy gained or dissipated by the statically condensed modes is neglected. This can lead

to significant inaccuracies in the ROM predictions, which is demonstrated using a 2-DOF oscillator, an FE model of an axially-excited inclined cable, and an FE model of a cantilever beam. The proposed method enables the nonconservative forces acting on the statically condensed modes to be accounted for in the reduced dynamics. Excellent agreement is observed between the forced response curves of the full-order models and those of the proposed ROMs.

Chapter 7: Conclusions and future work

This final chapter summarises the conclusions of the thesis, and discussion is also devoted to potential avenues of future research.

Chapter 3

Accounting for quasi-static coupling

As discussed in section 2.3.2, the main difference between displacement-based and force-based indirect reduction methods lies in how the quasi-static coupling between low-frequency transverse modes and high-frequency in-plane modes is captured. Displacement-based methods require that in-plane modes are directly included in the reduction basis, thus increasing the size and computational complexity of the ROM. On the other hand, force-based methods can implicitly capture the response of the in-plane modes within the stress manifold; however, the resulting ROMs are sensitive to the scaling of the static solution dataset used to calibrate them, which may introduce significant errors if the relevant scale factors are not carefully tuned. In this chapter, quasi-static coupling is first investigated using a simple oscillator with nonlinearities up to the cubic order. Reduced-order models obtained using the Implicit Condensation and Expansion method include quadratic and cubic nonlinear terms; however, here it is demonstrated mathematically that the ROM describing the oscillator requires higher-order nonlinear terms to capture the modal coupling. Novel ROMs, with higher-order nonlinear terms, are then shown to be more accurate, and significantly more robust to scaling of the calibration dataset, compared to the traditional cubic ROMs. The robustness of these novel ROMs is further demonstrated using an FE model of a clamped-clamped beam.

Publication resulting from this work

Nicolaidou, E., Melanthuru, V. R., Hill, T. L., and Neild, S. A. (2020). Accounting for quasi-static coupling in nonlinear dynamic reduced-order models. *Journal of Computational and Nonlinear Dynamics*, 15(7):071002

3.1 Introduction

This chapter investigates the mechanism that underpins the quasi-static coupling between low- and high-frequency modes in nonlinear dynamical systems. Membrane stretching is an example of quasi-static coupling, i.e. the response of in-plane/axial modes in beams and plates, may be assumed to be a function of the response of transverse/bending modes. Here, the more general term is employed to account for similar effects in systems without membrane-like features, such as the simple oscillator which will be considered as a motivating example in section 3.2. The effect of quasi-static coupling is investigated in detail using a force-based indirect reduction procedure, and it is demonstrated that a ROM that is insensitive to the selection of force scale factors may exist. Specifically, it is demonstrated that, for a general, geometrically nonlinear structure, quasi-static coupling causes the order of the nonlinearity in the reduced dynamics to increase. In other words, even though the full-order system contains nonlinearities only up to the cubic order, the ROM must include higher-order nonlinear terms in order to accurately capture its response. This is in contrast to existing approaches, whereby reduction is achieved via a linear projection, such that the nonlinearity in the ROMs is limited to cubic order (Mignolet *et al.*, 2013). It is shown that, using a higher order of nonlinearity in the ROM, not only leads to a more robust parametric fitting procedure, but the resulting ROMs can be significantly more accurate.

The rest of this chapter is structured as follows. Section 3.2 introduces a simple, 2-DOF oscillator which exhibits quasi-static coupling between its two modes; this is used as a motivating example to demonstrate the effect of including higher orders of nonlinearity in the ROMs. After formalising the definition of quasi-static coupling in section 3.3, the oscillator is used to demonstrate that a ROM which is invariant to the force scale factors does exist, but requires a higher order of nonlinearity in the reduced dynamics. In section 3.4, the approach is demonstrated using an FE model of a clamped-clamped beam. Finally, the conclusions are summarised in section 3.5.

3.2 Motivating example

Quasi-static coupling describes the coupling between the linear normal modes of a system, whereby the response of one mode may be expressed as a function of the response of another mode or set of modes. For example, as shown in figure 3.1,

the tip of a thin cantilever beam will move towards the root of the beam as the bending amplitude increases; this may be viewed as an axial displacement of the beam. However, this axial motion is a function of the vertical deflection, rather than an independent DOF, provided that the axial stiffness is much greater than the bending stiffness. A beam is considered in section 3.4, however, first, a conceptually simple system is used to demonstrate the quasi-static coupling effects and examine their influence on the process of reduced-order modelling.

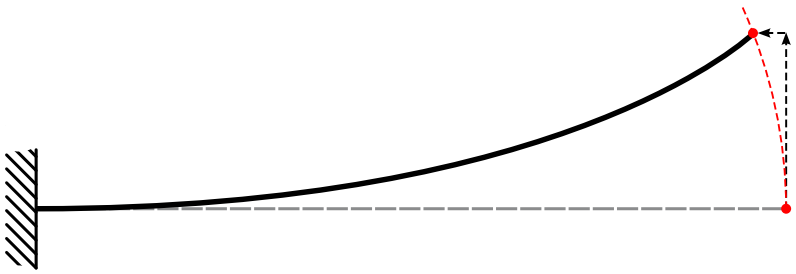

Figure 3.1. Schematic diagram depicting the axial motion of the tip of a cantilever beam undergoing a large deflection. The dashed red line shows the path of the tip of the beam.

3.2.1 Two-DOF oscillator

In this section, a simple, 2-DOF oscillator is used to investigate the effects of quasi-static coupling. The oscillator consists of a single mass $m = 0.1\,\mathrm{kg}$, and is constrained by two springs of length $\ell = 0.1\,\mathrm{m}$, which are undeformed and oriented along the x- and y-directions at the equilibrium configuration, as shown in figure 3.2 (a). The springs are linearly elastic, with stiffness coefficients $k_1 = 10\,\mathrm{N\,m^{-1}}$ and $k_2 = 1000\,\mathrm{N\,m^{-1}}$, respectively, and obey a linear strain–displacement relationship. A similar model, which involves springs with a quadratic strain–displacement relationship, has previously been considered in the context of reduced-order modelling by Touzé *et al.* (2004a; 2006).

As the two springs are orthogonal and have no pretension, the first linear mode of the system is captured by a purely horizontal (x-direction) motion, whilst the motion of the second mode is purely vertical (y-direction). As $k_2 \gg k_1$, the second natural frequency is considerably greater than the first, i.e. $\omega_2 = 10\,\omega_1$. Additionally, if the mass is deflected horizontally (i.e. in the first mode), the strong coupling between the modes will cause a deflection in the vertical direction (i.e. the second mode). For small dynamic displacements in the first mode, the mass will follow an arced path, as

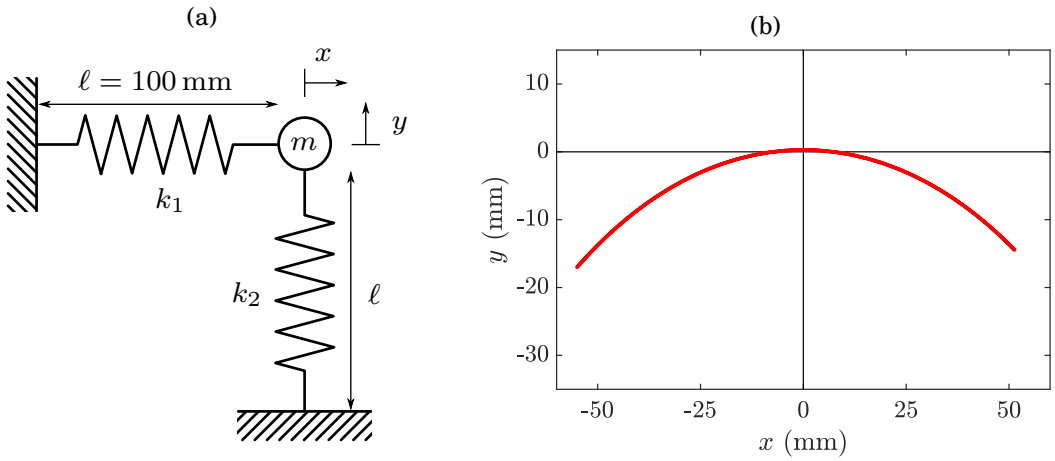

Figure 3.2. (a) Schematic diagram of the single-mass, 2-DOF oscillator at its equilibrium position. (b) A free, periodic response of the 2-DOF oscillator, shown in the projection of horizontal displacement against vertical displacement, parameterised in time.

shown in figure 3.2 (b).[1] This response clearly shows a displacement in the vertical direction; however, rather than being an independent DOF, the vertical displacement may be considered to be a function of the horizontal displacement, i.e. $y = f(x)$. This is analogous to the cantilever beam shown in figure 3.1, which also exhibits strong coupling between modes with a large separation in their natural frequencies. Note that, in the extreme case of $k_2 \to \infty$, this oscillator represents a pendulum — a system with only one DOF, which exhibits a response similar to that shown in figure 3.2 (b).

The equations of motion of the 2-DOF oscillator are written as

$$m\ddot{x} + F_x(x,y) = 0, \tag{3.1a}$$

$$m\ddot{y} + F_y(x,y) = 0, \tag{3.1b}$$

where F_x and F_y describe the restoring forces acting on the oscillator along the x- and y-direction, respectively. These restoring forces lead to coupling between motions in the x- and y-directions; however, as previously discussed, they do not generate a linear coupling force. Therefore, the linear modal coordinates may be written as $q_1 = mx$

[1] As this is a periodic response of the conservative system, this motion represents a nonlinear normal mode, i.e. a point on the first backbone curve of the oscillator, which emanates from the first natural frequency.

and $q_2 = my$ which, when substituted into equations (3.1) may be approximated to

$$\ddot{q}_1 + \omega_1^2 q_1 + \alpha_1 q_1^2 + \alpha_2 q_1 q_2 + \alpha_3 q_2^2 + \alpha_4 q_1^3 + \alpha_5 q_1^2 q_2 + \alpha_6 q_1 q_2^2 + \alpha_7 q_2^3 = 0, \tag{3.2a}$$

$$\ddot{q}_2 + \omega_2^2 q_2 + \beta_1 q_1^2 + \beta_2 q_1 q_2 + \beta_3 q_2^2 + \beta_4 q_1^3 + \beta_5 q_1^2 q_2 + \beta_6 q_1 q_2^2 + \beta_7 q_2^3 = 0, \tag{3.2b}$$

where the parameters are given in table 3.1. Note that, for the sake of simplicity, the nonlinear terms have been truncated to the cubic order, using a Taylor series expansion. Although this approximate model is no longer an exact reflection of the dynamics of the system, it does still exhibit the strong quasi-static coupling between the modes, which allows this effect to be investigated for a mathematically simple model. As such, the cubic approximation of the oscillator is referred to as the full-order model throughout this chapter, whilst a geometrically exact model is considered later in Chapter 6.

Table 3.1. Coefficients of the truncated equations of motion of the 2-DOF oscillator, equations (3.2).

Coefficient	Value	Coefficient	Value
ω_1	10	ω_2	100
α_1	0	β_1	5×10^5
α_2	10^6	β_2	10^4
α_3	5000	β_3	0
α_4	5×10^7	β_4	0
α_5	0	β_5	-1.01×10^8
α_6	-1.01×10^8	β_6	0
α_7	0	β_7	5×10^5

3.2.2 Overview of nonlinear reduced-order modelling

A nonlinear reduced-order model has fewer degrees-of-freedom than the original, full-order model; in this case, equations (3.2) are treated as the full-order model. The ROM must accurately reproduce the dynamic behaviour of the full-order model over a specific region, such as a range of response frequencies. For the case of the simple oscillator, the region of interest is defined as responses in the vicinity of the first natural frequency.[2] The reduced-order modelling approach developed here assumes that the full-order equations of motion are unknown, which is often the case when

[2] As discussed later, the region of interest corresponds to NNMs represented by the first backbone curve of the system.

a nonlinear structure is modelled using commercial FE software. Therefore, the reduction methodology should not require access to the full-order equations of motion. For the simple example considered here, the coefficients describing the full-order equations of motion are known, however these will not be explicitly used to compute the ROMs.

The reduced-order modelling procedure used here is the force-based indirect method described in section 2.3.2, known as Implicit Condensation and Expansion, which is implemented as follows:

1. Select the reduction basis and compute the linear reduced coefficients.
2. Apply a series of static forces to the full-order model, and extract the corresponding static displacements. For each load case, the applied force is a linear combination of the reduced modeshapes.
3. Estimate the parameters of the reduced nonlinear functions (i.e. the stress manifold) using the static force and displacement dataset.

Note that the number of load cases must be at least equal to the number of unknown parameters in the nonlinear functions. Therefore, a larger ROM (i.e. with a larger number of DOFs) or a higher order of nonlinearity, will require a larger number of static load cases. Traditionally, the nonlinear functions in the ROM are expressed as quadratic and cubic polynomials of the reduced coordinates, as discussed in section 2.3.2, equation (2.10) (Hollkamp and Gordon, 2008; Mignolet *et al.*, 2013).

3.2.3 Motivating results

The ICE method is now used to compute ROMs of the full-order model of the oscillator, equations (3.2). As previously discussed, the responses in the region of the first natural frequency are of interest, hence the ROM consists of a single mode, q_1. A typical ROM, with nonlinearities up to the cubic order, is written in the form

$$\ddot{q}_1 + \omega_1^2 q_1 + A_2 q_1^2 + A_3 q_1^3 = 0\,, \tag{3.3}$$

where the nonlinear coefficients, A_2 and A_3, are to be estimated using the static solution dataset, whilst the linear natural frequency, ω_1, is obtained using the linear mass and stiffness matrices of the full-order model. Equation (3.3) is referred to as the third-order ROM and may be considered as the standard approach used in the literature. An additional, and novel, ROM with nonlinear terms up to the ninth order[3]

[3]The motivation for this particular order of ROM is discussed in section 3.3.

is also used for comparison. This is termed the ninth-order ROM, and is written as

$$\ddot{q}_1 + \omega_1^2 q_1 + \sum_{k=2}^{9} A_k q_1^k = 0. \tag{3.4}$$

The ninth-order ROM has six additional parameters that must be estimated, and hence requires the computation of additional static solutions.

For both ROMs, the force-displacement dataset is obtained by applying a static force to the first mode of the oscillator, i.e. solving

$$\omega_1^2 q_1 + \alpha_1 q_1^2 + \alpha_2 q_1 q_2 + \alpha_3 q_2^2 + \alpha_4 q_1^3 + \alpha_5 q_1^2 q_2 + \alpha_6 q_1 q_2^2 + \alpha_7 q_2^3 = \kappa F_{q1}, \tag{3.5a}$$

$$\omega_2^2 q_2 + \beta_1 q_1^2 + \beta_2 q_1 q_2 + \beta_3 q_2^2 + \beta_4 q_1^3 + \beta_5 q_1^2 q_2 + \beta_6 q_1 q_2^2 + \beta_7 q_2^3 = 0, \tag{3.5b}$$

for q_1 and q_2, where F_{q1} is a normalised force applied to the first mode, and κ is a *force scale factor*. For each load case, the static force applied to the first mode is evenly spaced between $-\kappa$ and $+\kappa$, and the number of load cases matches the number of unknown parameters in the ninth-order ROM,[4] i.e.

$$F_{q1} = \left\{-1, -\frac{5}{7}, -\frac{3}{7}, -\frac{1}{7}, \frac{1}{7}, \frac{3}{7}, \frac{5}{7}, 1\right\}. \tag{3.6}$$

Once the static displacements corresponding to each load case are computed, the ROM parameters are estimated in a least-squares manner. For the third-order ROM, the nonlinear coefficients, A_2 and A_3, are computed as

$$\begin{pmatrix} A_2 \\ A_3 \end{pmatrix} = \mathbf{Q}^{-1}\mathbf{c_1}, \tag{3.7}$$

where the i^{th} rows of $\mathbf{Q}$ and $\mathbf{c_1}$ are populated with the results of the i^{th} load case, i.e.

$$\mathbf{Q} = \begin{pmatrix} \left[\begin{array}{cc} q_1^2 & q_1^3 \end{array}\right]_{F_{q1}=-1} \\ \left[\begin{array}{cc} q_1^2 & q_1^3 \end{array}\right]_{F_{q1}=-5/7} \\ \vdots \\ \left[\begin{array}{cc} q_1^2 & q_1^3 \end{array}\right]_{F_{q1}=+1} \end{pmatrix}, \tag{3.8a}$$

$$\mathbf{c_1} = \begin{pmatrix} \left[\begin{array}{c} \kappa F_{q1} - \omega_1^2 q_1 \end{array}\right]_{F_{q1}=-1} \\ \left[\begin{array}{c} \kappa F_{q1} - \omega_1^2 q_1 \end{array}\right]_{F_{q1}=-5/7} \\ \vdots \\ \left[\begin{array}{c} \kappa F_{q1} - \omega_1^2 q_1 \end{array}\right]_{F_{q1}=+1} \end{pmatrix}. \tag{3.8b}$$

[4]Note that, typically, ROMs are calibrated using a minimum number of load cases, e.g. 2 for a single-DOF third-order ROM. Here, each ROM utilises 8 load cases, which allows for a direct comparison between ROMs with different orders of nonlinearity.

A similar expression is used to estimate the parameters of the ninth-order ROM, where $\mathbf{Q}$ and $\mathbf{c_1}$ measure 8×8 and 8×1, respectively.

Figure 3.3 (a) shows how the cubic parameter, A_3, of the third- and ninth-order ROMs, varies with the force scale factor, κ.[5] The maximum force scale factor considered here, $\kappa = 0.16$, corresponds to an absolute static displacement of approximately 0.17 ℓ and 0.02 ℓ in the x- and y-directions, respectively. As previously noted in studies of the ICE method (Gordon and Hollkamp, 2011; Kuether, 2014), the values of the ROM parameters are dependent on the force scale factor. This is clearly seen in figure 3.3 (a) where, for the third-order ROM, A_3 varies significantly. As a result, the force scale factor must be carefully chosen to obtain an accurate model of the system. This large variation in A_3 illustrates a fundamental issue with the structure of the nonlinear function in the ROM. The cubic parameter of the ninth-order ROM,

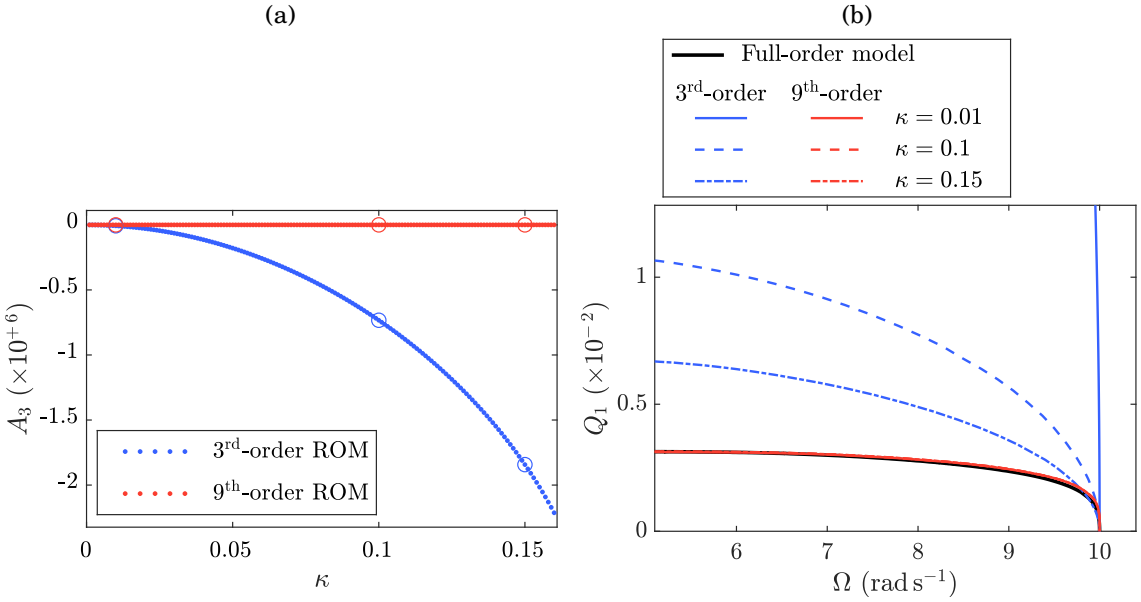

Figure 3.3. (a) Estimated value of the cubic parameter, A_3, of the third- and ninth-order ROMs, as the force scale factor varies. The circles denote specific force scale factors, at $\kappa = \{0.01, 0.10, 0.15\}$, that are used to compute the backbone curves shown on the right. (b) Comparison between the backbone curves of the third- and ninth-order ROMs, calibrated using different force scale factors. These are compared to the first backbone curve of the full-order model, shown in the projection of the response frequency, Ω, against the amplitude of displacement of the first mode, Q_1.

[5] Note that, typically, only one force scale factor is chosen to calibrate the ROM. Here, multiple scale factors are used in order to demonstrate the effect of this choice on the ROM parameters.

however, appears to be less sensitive, indicating that this model is more robust to the choice of force scale factor.

A backbone curve is a locus of periodic responses of the conservative system, and captures the fundamental dynamic behaviour of a nonlinear system (Kerschen *et al.*, 2009). As such, backbone curves may be used as a means of assessing the accuracy of ROMs (Kuether *et al.*, 2015). The backbone curves of the two ROMs, calibrated using three different force scale factors, are shown in figure 3.3 (b), along with the first backbone curve of the full-order model.[6] It can be seen that the ninth-order ROMs are not only more accurate than the corresponding third-order ROMs, but they are also significantly more robust to the choice of force scale factor. As shown in figure 3.3 (a), the cubic parameter of the third- and ninth-order ROMs becomes equivalent at low force scale factors, demonstrating that the difference between the backbone curves of these ROMs is driven by the higher-order terms.These results motivate the need for higher-order nonlinear terms in the ROM.

Recalling that the nonlinearities of the full-order system, equations (3.2), are truncated at the third order, it may seem counter-intuitive that the dynamics are best captured by a ninth-order ROM. The following section explores how the quasi-static coupling between the two modes leads to a ROM that requires a higher order of nonlinearity than the full-order system.

3.3 Accounting for quasi-static coupling

3.3.1 Effect of quasi-static coupling on the order of nonlinearity

When a force is applied in the first mode of the 2-DOF oscillator, the resulting static deflection in the first mode is accompanied by a static deflection in the highly stiff second mode, such that the oscillator follows an arced path, as previously illustrated in figure 3.2 (b). This modal coupling may be approximated as quasi-static, i.e. the second mode may respond dynamically,[7] but is constrained by the coupling with the first mode, which may be captured statically. Therefore, the reduction procedure cannot rely on the assumption that q_2 is small; in other words, removing all q_2-dependent terms in the first modal equation of motion of the full-order model,

[6] All backbone curves have been computed using the MATLAB-based numerical continuation package Continuation Core (COCO), which solves boundary-value problems using a collocation method with piecewise polynomials (Dankowicz and Schilder, 2013; Schilder and Dankowicz, 2015).

[7] In the presence of a dynamic interaction (e.g. internal resonance), the participating modes must be included as independent DOFs in the reduction basis — this will be explored in Chapter 5.

equation (3.2a), will lead to inaccurate results. Instead, reducing the number of DOFs of the full-order model relies on the assumption that the inertial term, $\ddot{q}_2$, is small relative to the stiffness components in the second modal equation of motion, equation (3.2b). This allows the *dynamics* of the second mode to be neglected, without requiring the displacement to be negligible. When the second natural frequency is significantly larger than the first, i.e. $\omega_2 \gg \omega_1$, and the response frequency of the system is in the vicinity of ω_1, this assumption is reasonable, and does not require q_2 to be small relative to q_1. This is because the inertial term in the second equation of motion is in the order of $\omega_1^2 q_2$, whilst the linear stiffness term is $\omega_2^2 q_2$. By assuming that $\ddot{q}_2 \approx 0$, the second equation of the static full-order system, equation (3.5b), allows the response of the second mode to be written as a function of q_1, i.e.

$$q_2 = f\left(q_1, \omega_2, \beta_1, \beta_2, \ldots\right), \tag{3.9}$$

where ω_2 and β_i are the linear and nonlinear parameters of equation (3.5b), respectively. This may be approximated as a J^{th}-order polynomial function of q_1, i.e.

$$q_2 \approx \sum_{j=2}^{J} B_j q_1^j, \tag{3.10}$$

where the coefficients, B_j, are a function of the parameters in the second equation of motion of the full-order model, but are independent of q_1 or the force applied to the system, i.e. $B_j = B_j\left(\omega_2, \beta_1, \beta_2, \ldots\right)$. As such, the values B_j are fixed for a given set of system parameters. Note that no linear term is included in equation (3.10), as q_1 and q_2 are, by definition, linearly uncoupled. Substituting equation (3.10) into the first equation of motion of the full-order model, equation (3.2a), leads to the reduced equation of motion

$$\ddot{q}_1 + \omega_1^2 q_1 + \sum_{j=2}^{3J} A_j q_1^j = 0, \tag{3.11}$$

where

$$A_2 = \alpha_1, \tag{3.12a}$$

$$A_3 = \alpha_4 + B_2\alpha_2, \tag{3.12b}$$

$$A_4 = B_2\alpha_5 + B_2^2\alpha_3 + B_3\alpha_2, \tag{3.12c}$$

$$A_5 = B_2^2\alpha_6 + 2B_2B_3\alpha_3 + B_3\alpha_5 + B_4\alpha_2, \tag{3.12d}$$

$$A_6 = B_2^3\alpha_7 + 2B_2B_3\alpha_6 + 2B_2B_4\alpha_3 + B_3^2\alpha_3 + B_4\alpha_5 + B_5\alpha_2, \tag{3.12e}$$

$$A_7 = 3B_2^2B_3\alpha_7 + 2B_2B_4\alpha_6 + 2B_2B_5\alpha_3 + B_3^2\alpha_6 + 2B_3B_4\alpha_3 + B_5\alpha_5 + B_6\alpha_2, \tag{3.12f}$$

$$\vdots \quad \vdots$$

Note that when $J = 3$, equation (3.11) is equivalent to the ninth-order ROM considered earlier, equation (3.4).

Equations (3.12) show that the ROM parameters, A_i, are only dependent on the quasi-static coupling parameters, B_j, and the nonlinear full-order parameters, α_k. As such, the ROM parameters are *independent of the force scale factor*. Recalling that the nonlinear terms in the full-order model do not go beyond the cubic order, it should be highlighted that this ROM has a significantly higher order of nonlinearity than the full-order equations of motion. In general, assuming that q_2 is a function of q_1 will lead to higher-order nonlinear terms in the ROM, as this quasi-static coupling function must be nonlinear.

As the lowest order of nonlinearity in the full-order system is quadratic, the quasi-static coupling parameter B_j cannot contribute to the parameter A_i, where $i < j+1$. This can be seen in equations (3.12), where B_2 does not contribute to A_2, and B_3 does not contribute to A_2 or A_3, etc. As such, the ROM parameters up to A_9 can be computed precisely by finding q_2 as a function of q_1 up to order $J = 8$, from equation (3.10). These parameters are given in table 3.2.

Table 3.2. Values of parameters of the quasi-static coupling function, and the function of reduced nonlinear restoring forces.

Coefficient	Value	Coefficient	Value
B_2	-50	A_2	0
B_3	$+50$	A_3	0
B_4	-5.051×10^5	A_4	$+6.250 \times 10^7$
B_5	$+1.010 \times 10^6$	A_5	-7.576×10^{11}
B_6	-5.096×10^9	A_6	$+1.768 \times 10^{12}$
B_7	$+1.528 \times 10^{10}$	A_7	-1.020×10^{16}
B_8	-5.129×10^{13}	A_8	$+3.440 \times 10^{16}$
		A_9	-1.285×10^{20}

Table 3.2 shows that the quadratic and cubic parameters, A_2 and A_3, of the reduced-order model are both zero. Recalling that the full-order equations of motion contain quadratic and cubic terms, this may seem surprising and further highlights the importance of considering higher-order terms during the fitting procedure. This also demonstrates why, for low force scale factors, the third-order ROM tends towards a linear system, as seen in figure 3.3 (b). Note, however, that $A_2 = A_3 = 0$ is not a

feature that is common to all ROMs; this is demonstrated in section 3.4, where an FE model of a clamped-clamped beam is considered.

In all but the simplest of systems, computing the ROM parameters *directly* as a function of the coefficients of the full-order model is impractical, and often altogether infeasible, e.g. when considering structures modelled using commercial FE software. For more complex systems, these parameters may still be estimated in a least-squares manner, as shown in section 3.2.3, which will require a truncation of the order of the nonlinearity in the ROM. This will introduce an error, which is likely to increase as the force scale factor is increased; this is because the neglected higher-order terms become relatively more significant as the response amplitude increases. However, this may be viewed as an *approximation error*, rather than a *tuning* of the model, as the ROM parameters are invariant with respect to the force scale factor.

3.3.2 Reduced-order models of the oscillator

Figure 3.4 shows the relative errors between the true (equation (3.12)) and estimated parameters (equations (3.7) and (3.8)) of the third- and ninth-order ROMs. The relative error is defined as $\left(\hat{A}_i - \bar{A}_i\right)/\bar{A}_i$, where $\bar{A}_i$ and $\hat{A}_i$ denote the true and estimated values of A_i, respectively. For the quadratic and cubic coefficients, the estimated values are shown, rather that the relative errors, since $\bar{A}_2 = \bar{A}_3 = 0$. Note that the plot of the estimated values of A_3, for the two different ROMs, was shown previously in figure 3.3 (a).

Figure 3.4 further demonstrates that the ninth-order ROM is significantly more robust with respect to the force scale factor, κ, than the third-order model. However, figure 3.4 does reveal that there is some error associated with the estimation of the ninth-order parameters, and that this error increases with κ. As previously discussed, this is due to the higher-order terms becoming relatively more significant at higher force scale factors. The magnitude of these errors appears to increase as the order of the nonlinear terms increases; however, for the range of force scale factors considered here, these errors remain small. This is because the relative significance of the corresponding polynomial term is small, as discussed in the following section and shown in figure 3.6. Assuming that the terms above the ninth-order are negligible, this suggests that the ninth-order fit should give consistently accurate results, even at low force scale factors.

The dynamics of the condensed mode, q_2, can be approximated by means of

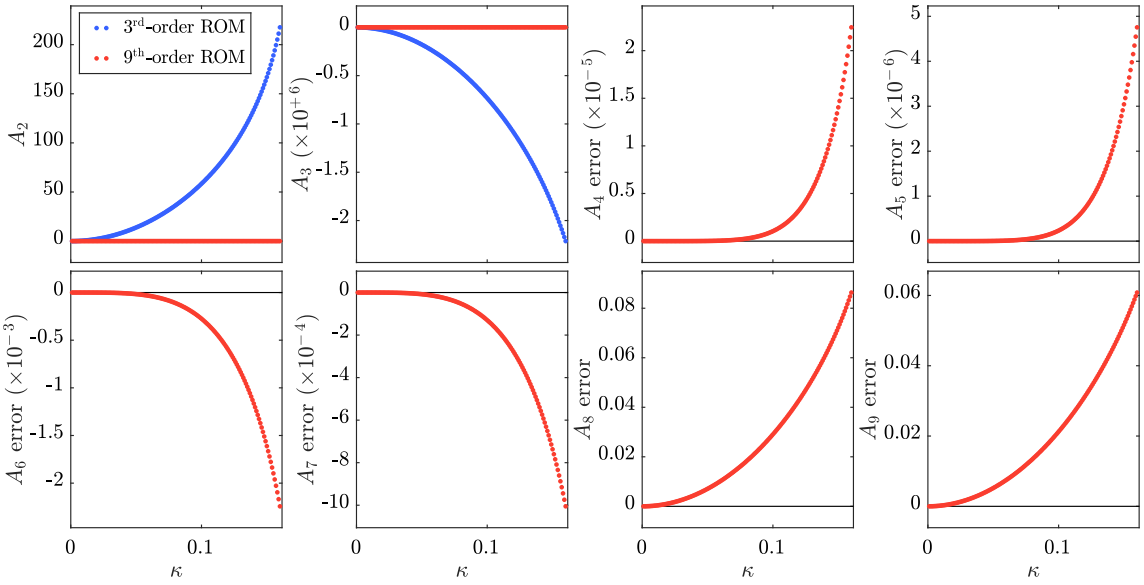

Figure 3.4. Relative errors of the estimated parameters of the third- and ninth-order ROMs, as the force scale factor varies. For the quadratic and cubic parameters, A_2 and A_3, the estimated values are shown, rather than the relative errors, as the true parameters are equal to zero (see table 3.2).

the quasi-static coupling function. The quasi-static coupling coefficients may be approximated in a least-squares manner, as with the function of reduced nonlinear restoring forces, using the existing static solution dataset. For the third-order ROM, these may be computed as

$$\begin{pmatrix} B_2 \\ B_3 \end{pmatrix} = \mathbf{Q}^{-1}\mathbf{c_2}, \tag{3.13}$$

where

$$\mathbf{c_2} = \begin{pmatrix} \begin{bmatrix} q_2 \end{bmatrix}_{F_{q1}=-1} \\ \begin{bmatrix} q_2 \end{bmatrix}_{F_{q1}=-5/7} \\ \vdots \\ \begin{bmatrix} q_2 \end{bmatrix}_{F_{q1}=+1} \end{pmatrix}, \tag{3.14}$$

and $\mathbf{Q}$ is as defined in equation (3.8). A similar expression is used for the ninth-order ROM.

Figure 3.5 shows the first backbone curve of the oscillator in terms of the amplitudes of the first and second modes, Q_1 and Q_2. The response of the first mode is

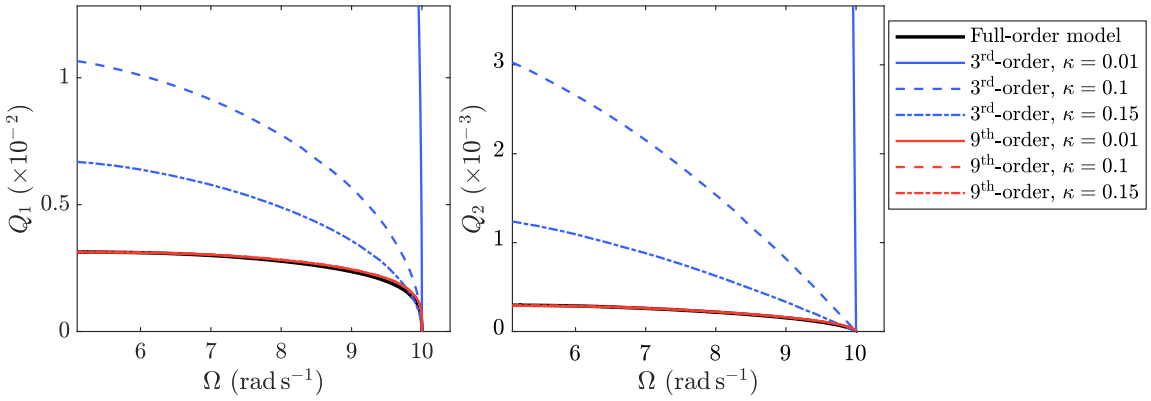

Figure 3.5. Comparison between the backbone curves of the third- and ninth-order ROMs, calibrated using different force scale factors. These are compared to the first backbone curve of the full-order model.

computed directly based the reduced equation of motion, equation (3.11), whilst the amplitude of the condensed mode is computed in a post-processing step, using the quasi-static coupling function, equation (3.10). The values of parameters B_j differ between the force scale factors and ROMs. As previously discussed for the Q_1-projection in figure 3.3 (b), the backbone curve of the ninth-order ROMs (red lines) show a much better agreement with that of the full-order model (black line) than that of the third-order ROMs (blue lines); this trend is also seen in the projection of the second modal amplitude, Q_2. In both projections, the backbone curves of the ninth-order ROMs overlap, demonstrating the robustness of the ROM with respect to the force scale factor. It should be acknowledged that, to some degree, it is unsurprising that a higher-order polynomial enables a better approximation of the static solution dataset; however, it is the physical justification for this that is paramount.

3.3.3 Comparing the accuracy of different truncation orders

The ninth-order ROM has been shown to be significantly more accurate in capturing the response of the full-order model, and significantly more robust with respect to the force scale factor, in comparison with the third-order ROM. This demonstrates the advantages of including a high order of nonlinearity in the ROM, even when the full-order model contains nonlinear terms only up to the cubic order. As previously discussed, the ninth-order of nonlinearity captures the effects of all terms in the quasi-static coupling function, equation (3.10), up to the third order, i.e. for $J = 3$. However, it has also been noted that the terms in the ROM with a very high order are

likely to be less significant. This implies that a lower order of nonlinearity (i.e. lower than ninth-order) in the ROM may still be able to accurately capture the dynamics of the full-order system. This is first investigated by inspecting the magnitudes of the terms in the ninth-order ROM at different response amplitudes.

Figure 3.6 compares the magnitudes of each monomial in the ROM for three different points on the backbone curve. The magnitude of the n^{th}-order term is defined as $\max\{|A_n q_1^n|\}$, where the true value of A_n is used, from table 3.2, and the backbone curve is computed using the full-order model. The labels on the axes of the inset panels denote the term order. Note that the second- and third-order terms are not shown as $A_2 = A_3 = 0$, hence their magnitudes must be zero. Figure 3.6 clearly demonstrates that, for the three points shown here, the fifth-order term is dominant. The seventh-order term becomes more significant at higher amplitudes, whilst the ninth-order term is negligible at lower amplitudes, and very small at higher amplitudes. Of the even-valued terms, the fourth-order term is relatively significant, particularly at low amplitudes, whilst the sixth- and eighth-order terms are negligible for all three points shown.[8]

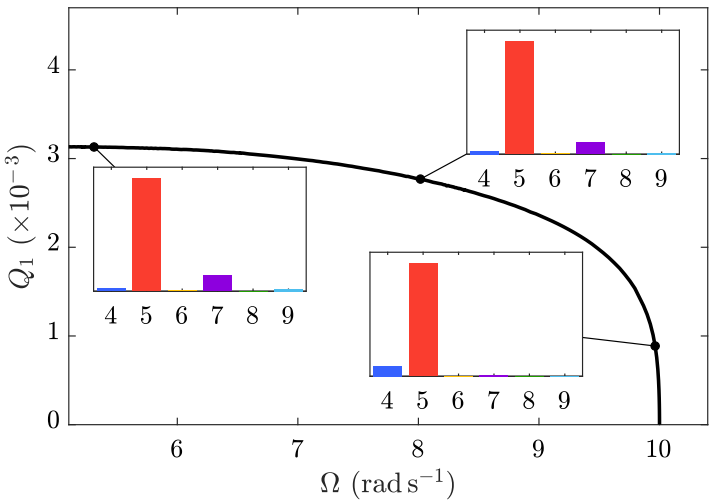

Figure 3.6. Comparison of the relative magnitudes of the nonlinear terms in the ROM, for three different points on the backbone curve. The black line shows the backbone curve of the full-order system and the three black dots denote the three responses used for comparison. The inset panels show the relative magnitude of each term, where the n^{th} term is given by $\max\{|A_n q_1^n|\}$.

[8]Note that this analysis requires the true parameters of the ROM to be known, and hence the significance of each nonlinear term cannot typically be determined *a priori*.

The observation that the magnitudes of the high-order terms appear to be small, implies that a lower-order (i.e. lower than ninth-order, but higher than third-order) ROM may be able to produce accurate results. This is now investigated by comparing all orders of ROM, from the third to the ninth. As before, each ROM uses 8 evenly distributed load cases.

Figure 3.7 shows the backbone curves obtained using ROMs truncated to different orders of nonlinearity, all found using a force scale factor of $\kappa = 0.1$. The top panels compare the third- and fourth-order ROMs, represented by dashed blue and solid red lines, respectively, to the full-order model, represented by a solid black line. It can be seen that the addition of the fourth-order term only allows for a small improvement to the accuracy of the backbone curve. This is to be expected as, from figure 3.6, the fifth-order monomial is the most significant term, but is not included in either the third- or fourth-order ROM.

The bottom panels in figure 3.7 compare the backbone curves of the fifth- to ninth-order ROMs, to that of the full-order model. These are significantly more accurate than the third- and fourth-order ROMs; this is primarily due to the presence of a fifth-order nonlinearity, which was previously identified as the most significant term.

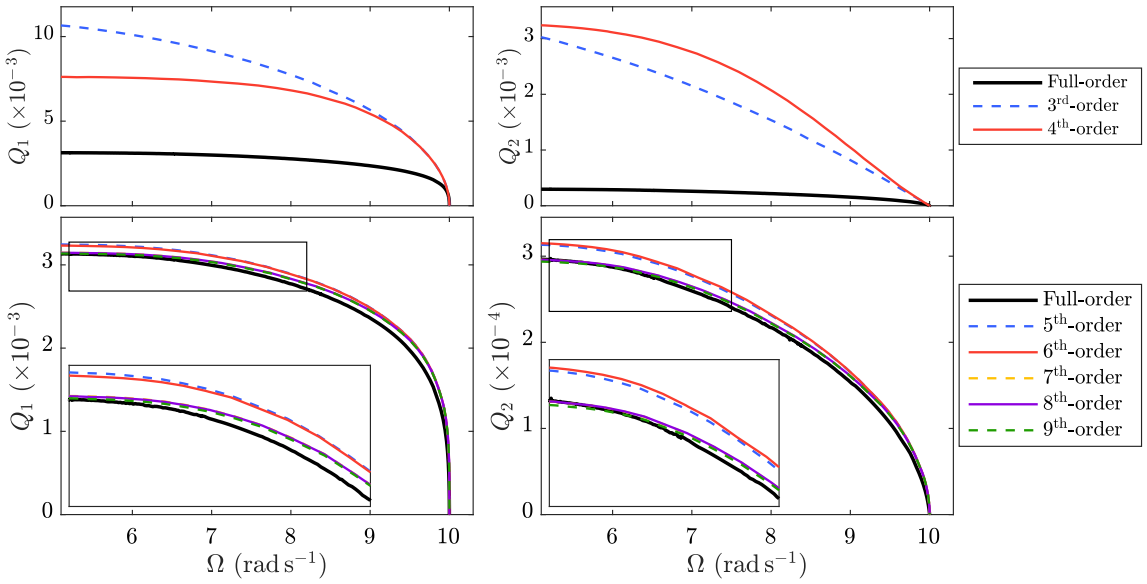

Figure 3.7. Comparison between the backbone curves of ROMs truncated to different orders of nonlinearity, for $\kappa = 0.1$. Top: third- and fourth-order ROMs; bottom: fifth- to ninth-order ROMs. These are compared to the first backbone curve of the full-order model.

Comparing the fifth- and sixth-order ROMs reveals that the addition of the sixth-order term results in a small improvement, reflecting the observation from figure 3.6 that the sixth-order term is negligible. Likewise, the seventh- and eighth-order backbone curves are indistinguishable, as the eighth-order term is also negligible. However, as the seventh-order term is significant, the seventh- and eighth-order ROMs do show a significant improvement compared to the lower orders. Finally, the ninth-order ROM leads to an improvement in accuracy; however, this improvement is minor, due to the relative magnitude of the ninth-order term.

It can be concluded that, whilst the ninth-order ROM is required to fully capture the cubic enslavement of the second mode to the reduced mode (i.e. for $J = 3$), the effect of the ninth-order term is negligible. A very good fit in the backbone curve may still be achieved with a seventh-order model, and a fifth-order model also provides a good fit. Overall, this demonstrates that a higher-order will lead to a greater accuracy but, if a lower-order is desired (for example, if a limited number of load cases, and hence parameters, are available) then a good accuracy may still be achieved.

In summary, this section has demonstrated that the quasi-static coupling between the two linear modes of the simple, 2-DOF oscillator leads to a higher order of nonlinearity in the ROM than in the full-order equations of motion. Whilst a higher-order ROM does require additional parameters to be estimated, it is significantly more robust to the force scale factor and produces significantly more accurate results. The following section extends this analysis to an FE model of a clamped-clamped beam.

3.4 Application to FE model of a clamped-clamped beam

The third- and ninth-order single-mode ROMs of a geometrically nonlinear clamped-clamped beam, modelled using the FE software Abaqus[9] (Dassault Systèmes, 2017), are now considered. The beam has a length, width and thickness (h) of 650 mm, 30 mm and 2 mm, respectively, and is constructed of steel with a Young's modulus, shear modulus and density of 210 GPa, 80 GPa and 7850 kg m^{-3}, respectively. The beam is discretised using 130 three-node quadratic beam elements (Timoshenko type, B32 (Dassault Systèmes, 2017)), resulting in 1554 DOFs. Its first mode, which is the only mode retained in the ROMs, corresponds to the first bending mode of the beam

[9] All numerical modelling throughout this thesis is implemented in MATLAB, with the aid of the Abaqus2Matlab toolbox (Papazafeiropoulos *et al.*, 2017).

and has a linear natural frequency of $\omega_1 \approx 158\,\mathrm{rad\,s^{-1}}$. Note that the single-mode ROMs computed here, aim to capture the salient behaviour of the beam in the vicinity of the first backbone curve, and are used to investigate the coupling between the low-frequency (bending) and high-frequency (axial) modes; they are not intended to fully describe the dynamics of the system, for example by capturing internal resonances.

The static solution data used to construct the ROMs are obtained by applying a static force proportional to the first modeshape, and projecting the resulting physical displacement of the beam, onto the mass-normalised linear modeshapes. Similar to the approach described in section 3.2.3, both the third- and ninth-order ROMs constructed for each force scale factor, utilise 8 pairs of force–displacement data, in which the reduced modal force applied to the beam is equally distributed between $-\kappa$ and $+\kappa$. The minimum force scale factor considered here, $\kappa = 8.7$, corresponds to the force required to achieve a maximum displacement of $\sim 1\,\mathrm{mm} = 0.5\,h$ in the underlying linear system, which occurs at the midspan of the beam. This value was found to produce optimal results for a single-mode ROM of a clamped-clamped beam in Kuether *et al.* (2015), where the sensitivity to the scale factor was demonstrated using the *Constant Linear Displacement* method of scaling, originally proposed by Gordon and Hollkamp (2011). The maximum force scale factor considered here, $\kappa = 100$, extends beyond the optimal value, and corresponds to a linear maximum displacement of $\sim 11.5\,\mathrm{mm} = 5.75\,h$, and an actual (nonlinear) maximum displacement of $w_{\max} \sim 3.64\,\mathrm{mm} = 1.82\,h$.

3.4.1 Modal coupling

Figure 3.8 (a) shows the displacement of the first and second axial modes, q_{59} and q_{101}, against the displacement of the first (bending) mode, q_1. These modal displacements are reached when forces are applied in only the first mode, hence the axial displacements are only induced due to the coupling with the first mode. As these modes are significantly stiffer than the first (i.e. $\omega_{59}/\omega_1 \approx 316$ and $\omega_{101}/\omega_1 \approx 632$), this coupling may be assumed to be quasi-static, as seen in the simple oscillator considered previously. There is a clear similarity between the free periodic response of the simple oscillator, shown previously in figure 3.2 (b), and the response of the beam shown in figure 3.8 (a).

Figure 3.8 (b) shows the corresponding elastic potential energy of the two axial modes as a percentage of the energy of the first mode, plotted against the displace-

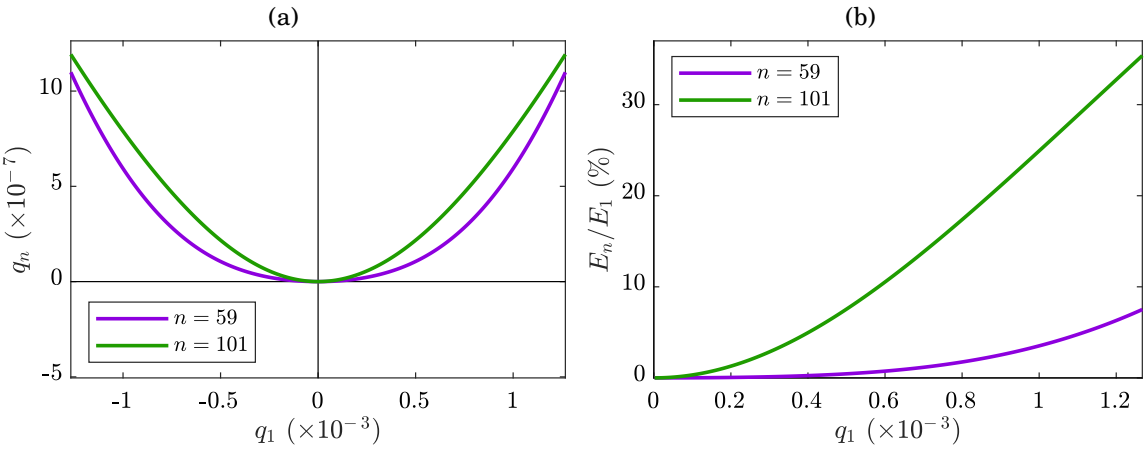

Figure 3.8. (a) Static displacements of the first bending mode, q_1, and two axial modes, q_{59} and q_{101}, when a force is applied in the first mode of the clamped-clamped beam. (b) Elastic potential energy of the two axial modes, E_{59} and E_{101}, as a fraction of the energy of the first mode, E_1, plotted against the static displacement of the first mode.

ment of the first mode.[10] These are calculated using a linear energy integral, i.e. $E_n = 0.5\omega_n^2 q_n^2$, for $n = 1, 59, 101$. Even though the force was only applied to the first mode of the beam, the amount of energy induced in the highly stiff axial modes is relatively large. This highlights the significance of the axial modes in the response of the beam, even when operating at frequencies much lower than their natural frequencies.

3.4.2 Single-mode ROM results

Figure 3.9 shows the estimated parameters of the third- and ninth-order ROMs of the clamped-clamped beam, for force scale factors in the range $\kappa = [8.7, 100]$. It can be seen that both the third- and ninth-order ROMs predict a quadratic parameter, A_2, that is close to zero, regardless of the scale of the load applied. This is expected, as the structure is symmetric.

The cubic parameter, A_3, of the third-order ROM (represented by blue dots) varies significantly as the force scale factor is increased. The cubic parameter in the ninth-order ROM, meanwhile, remains close to a fixed value, suggesting that it is less sensitive to the force scale factor. This agrees with the findings of the simple oscillator

[10] As the response of the axial modes is symmetric, only positive displacements are shown here.

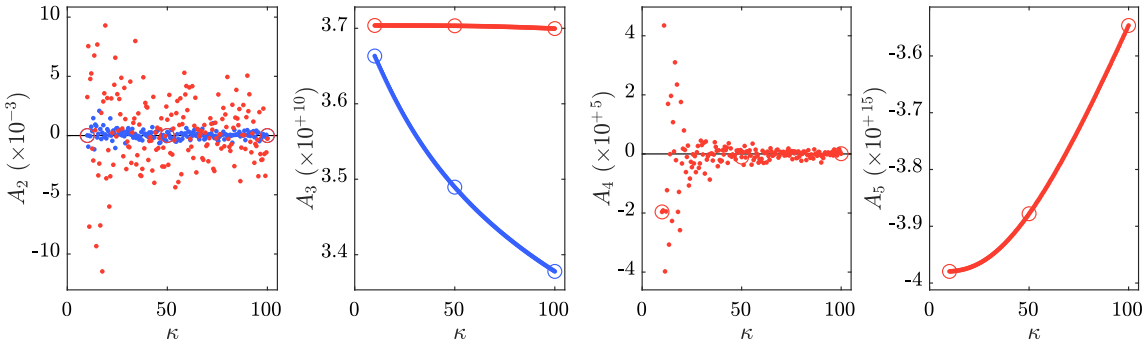

Figure 3.9. Estimated values of the parameters of the third- and ninth-order ROMs, as the force scale factor varies. The circles denote specific force scale factors, at $\kappa = \{8.7, 50, 100\}$, that are used to compute the backbone curves shown in figure 3.10.

considered in previous sections.

The even-valued parameter A_4 (only present in the ninth-order ROM) fluctuates around relatively small values.[11] The term corresponding to this parameter may be considered negligible, which, again, is expected due to the symmetric nature of the beam.

In contrast, the odd-valued parameter A_5 is more than 10 orders of magnitude larger than A_4, and the trend it exhibits is qualitatively similar to that of A_3. The significance of this term is also later verified in figure 3.11, further justifying the need for nonlinear terms of order higher than cubic. Given the magnitude of the quintic monomial in the ROM, relative to the cubic one, the effect of the variation in A_5 is small, resulting in a robust ROM as the force scale factor varies.

Figure 3.10 shows a comparison of the backbone curves of the third- and ninth-order ROMs, calibrated using three different force scale factors ($\kappa = \{8.7, 50, 100\}$). Note that, as the backbone curve of the full-order FE model is unknown, it is not compared to that of the ROMs in this case. The figure demonstrates the sensitivity of the third-order ROMs to the force scale factor, which can lead to inaccurate response predictions when the scaling of the static solution dataset is not carefully tuned. In contrast, the ninth-order ROMs result in backbone curves that remain practically indistinguishable as the scale factor varies.

It should also be highlighted that the ninth-order ROMs produce results similar

[11] Note that, whilst $A_4 = \mathcal{O}(10^4)$, the corresponding ROM term will be insignificant, i.e. $A_4 q_1^4 = \mathcal{O}(10^{-8})$, since $q_1 = \mathcal{O}(10^{-3})$.

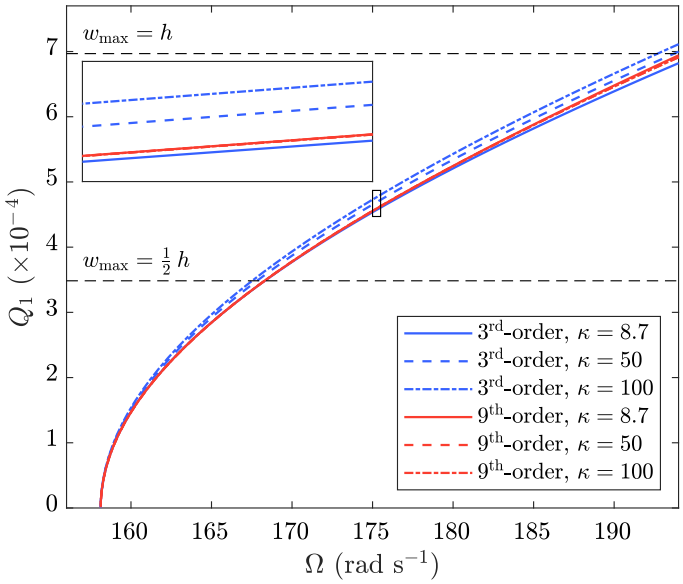

Figure 3.10. Comparison between the backbone curves of the third- and ninth-order ROMs, calibrated using different force scale factors.

to those obtained using the optimal third-order ROM ($\kappa = 8.7$), as reported in Kuether *et al.* (2015). This highlights the accuracy, as well as robustness of the ninth-order ROMs, which can eliminate the need for carefully tuning the force scale factors for each specific application and set of operating conditions.

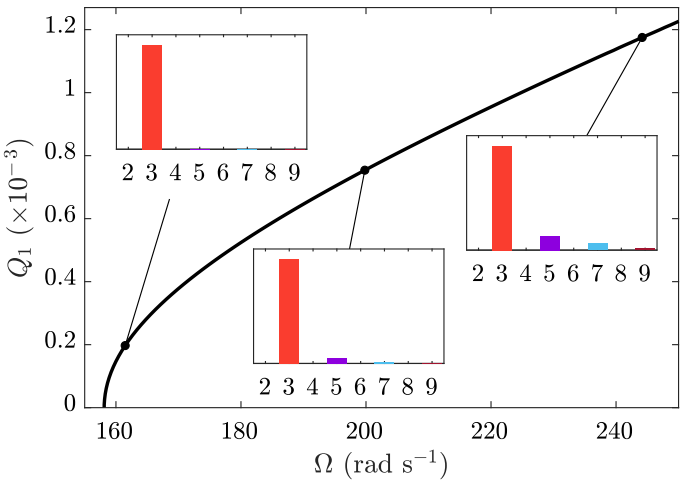

Figure 3.11. Comparison of the relative magnitudes of the nonlinear terms in the ROM, for three different points on the backbone curve. The black line shows the backbone curve of the ninth-order ROM and the three black dots denote the three responses used for comparison. The inset panels show the relative magnitude of each term.

Figure 3.11 shows the backbone curve predicted by the ninth-order ROM, calibrated using a force scale factor of $\kappa = 100$. Similar to figure 3.6, the inset panels represent the magnitude of the nonlinear term for three different points on the backbone curve. The figure demonstrates that the cubic terms are dominant in all three responses, which largely justifies the use of third-order ROMs in similar studies in the literature, especially for lower response amplitudes. However, it is highlighted that the odd-valued higher-order nonlinearities become increasingly significant at higher amplitudes. This indicates that, as with the simple oscillator, a ROM with an order of nonlinearity that is higher than cubic, is required to robustly and accurately capture the backbone curve of the full-order model as the response amplitude increases.

3.5 Summary

This chapter has demonstrated that the coupling between high- and low-frequency modes in a nonlinear dynamical system may be approximated as a *quasi-static* interaction. If this coupling is sufficiently strong, the response of the statically coupled modes must be accounted for in the reduced-order model, but they do not need to be modelled as independent DOFs. Specifically, it has been shown that quasi-static coupling introduces higher orders of nonlinearity in the reduced dynamics, beyond the order of nonlinearity present in the full-order model. It has been demonstrated that including higher-order nonlinear terms leads to a significant increase in the accuracy of the ROMs, determined by comparing the backbone curves of a conceptually simple, 2-DOF oscillator. Furthermore, these higher-order ROMs are significantly more robust to the force scale factor used to estimate the reduced parameters. These findings have also been validated by computing ROMs of a clamped-clamped beam, modelled using commercial FE software.

Even though ROMs with higher orders of nonlinearity require a larger number of parameters to be estimated, their invariance to force scale factor renders them more robust and removes the need for any tuning of the force scale factor. Additionally, ROMs may be calibrated using larger force scale factors, thus removing the need to extrapolate the responses of the models beyond their calibrated domain. This further adds to the robustness and trustworthiness of the higher-order ROMs.

Chapter 4

Capturing in-plane inertia

The applicability of force-based indirect reduced-order modelling methods, regardless of whether higher orders of nonlinearity are included in the reduced dynamics, is typically limited to structures in which: (a) the main source of nonlinearity is the quasi-static coupling between transverse and in-plane modes; and (b) the amount of in-plane displacement is limited. The second requirement arises from the fact that, in existing methods, in-plane inertia/kinetic energy is assumed to be negligible. For structures such as thin plates and slender beams with fixed/pinned boundary conditions, such as the clamped-clamped beam considered in Chapter 3, this approximation is often reasonable; however, in structures with free boundary conditions (e.g. cantilever beams), this assumption is violated. This chapter bridges the gap between direct and indirect reduction methods, by exploiting the concept of nonlinear manifolds to show how in-plane kinetic energy can be accounted for in a non-intrusive manner, without requiring any additional information from the FE model. This new insight enables indirect reduction methods to be applied to a far wider range of structures whilst maintaining accuracy to higher deflection amplitudes. The accuracy of the proposed method is validated using an FE model of a cantilever beam.

Publication resulting from this work

Nicolaidou, E., Hill, T. L., and Neild, S. A. (2020). Indirect reduced-order modelling: using nonlinear manifolds to conserve kinetic energy. *Proceedings of the Royal Society A: Mathematical, Physical and Engineering Sciences*, 476(2243):20200589

4.1 Introduction

Direct and indirect reduced-order modelling methods, which were previously discussed in section 2.3, are often considered as largely distinct research areas. Methods in the former class, and specifically approaches based on the theory of invariant manifolds, are supported by a rigorous mathematical framework, but due to their high analytical complexity and intrusive nature, they cannot readily be employed for the reduction of large-scale FE models built within commercial software. On the other hand, indirect methods are much more applicable in practice; however, their approximate nature often means that the resulting ROMs are not necessarily optimal. The aim of this chapter is to bridge the gap between the two classes of methods, by exploiting the concept of underlying nonlinear manifolds whilst retaining the non-intrusive nature of indirect methods. Specifically, a Lagrangian approach to deriving ROMs of geometrically nonlinear structures is proposed, which aligns with the theory of NNMs defined as invariant manifolds in phase space for structures characterised by slow/fast dynamics; the proposed method may be considered as an extension to force-based indirect methods such as the ICE.

In the standard ICE method, the static solution dataset that is used to compute the stress manifold, is also used to approximate a set of quasi-static coupling functions, which relate the response of the condensed (in-plane) modes to that of the reduced (transverse) modes. These are only used in post-processing to recover physical deformations, stresses and strains of the FE model, but they do not influence the reduced dynamics. In the proposed method, the same information is utilised to enrich the reduced dynamics by accounting for the kinetic energy of the statically coupled modes, which the standard approach neglects; this additional treatment is referred to as *inertial compensation*.

The rest of this chapter is structured as follows. Section 4.2 introduces the theory behind force-based indirect reduction methods, and demonstrates the effectiveness and limitations of the ICE method using FE models of a clamped-clamped beam and a cantilever beam. In addition, it is shown that the inaccuracy of the ICE method, when considering the cantilever beam, is related to the kinetic energy of the in-plane modes. Section 4.3 introduces the proposed method of deriving nonlinear ROMs such that the kinetic energy of the statically coupled modes is retained, and in section 4.4 we revisit the cantilever beam example to compare ROMs computed using the traditional and the proposed method. Finally, conclusions are summarised in section 4.5.

4.2 The standard ICE method

4.2.1 Theory

Note that force-based indirect reduction methods, such as the ICE, were previously introduced in section 2.3.2 and utilised in Chapter 3, however the relevant equations are recalled here for completeness. The equations of motion of an undamped, continuous structure, discretised into N DOFs using the FE method, can be written as

$$\mathbf{M}\ddot{\mathbf{x}} + \mathbf{K}\mathbf{x} + \mathbf{f}(\mathbf{x}) = \mathbf{F} \tag{4.1}$$

in the physical space, and

$$\ddot{\mathbf{q}} + \mathbf{\Lambda}\mathbf{q} + \mathbf{f}_q(\mathbf{q}) = \mathbf{F}_q \tag{4.2}$$

in the modal space. Here, the linear normal modes of the FE model are separated into three distinct classes:

1. a small set of dynamically important, low-frequency transverse modes;
2. a small set of high-frequency in-plane modes, which may be assumed to be statically coupled to the transverse modes (Hollkamp and Gordon, 2008; Mignolet *et al.*, 2013);
3. the remaining modes, which are neither dynamically relevant nor statically coupled, and whose response is small enough to be neglected.

Modes from each group are denoted, respectively, by the subscripts $\bullet_r$ (reduced), $\bullet_s$ (statically coupled), and $\bullet_u$ (unmodelled), such that equation (4.2) can be rewritten as

$$\begin{bmatrix} \ddot{\mathbf{q}}_r \\ \ddot{\mathbf{q}}_s \\ \ddot{\mathbf{q}}_u \end{bmatrix} + \begin{bmatrix} \mathbf{\Lambda}_r & \mathbf{0} & \mathbf{0} \\ \mathbf{0} & \mathbf{\Lambda}_s & \mathbf{0} \\ \mathbf{0} & \mathbf{0} & \mathbf{\Lambda}_u \end{bmatrix} \begin{bmatrix} \mathbf{q}_r \\ \mathbf{q}_s \\ \mathbf{q}_u \end{bmatrix} + \begin{bmatrix} \tilde{\mathbf{f}}_r(\mathbf{q}_r, \mathbf{q}_s, \mathbf{q}_u) \\ \tilde{\mathbf{f}}_s(\mathbf{q}_r, \mathbf{q}_s, \mathbf{q}_u) \\ \tilde{\mathbf{f}}_u(\mathbf{q}_r, \mathbf{q}_s, \mathbf{q}_u) \end{bmatrix} = \begin{bmatrix} \mathbf{F}_r \\ \mathbf{F}_s \\ \mathbf{F}_u \end{bmatrix}, \tag{4.3}$$

where the lengths of vectors $\mathbf{q}_r$, $\mathbf{q}_s$ and $\mathbf{q}_u$ are R, S and U, respectively, such that $R+S+U=N$ and $R, S \ll N$. The corresponding modeshapes are contained in matrices $\mathbf{\Phi}_r$, $\mathbf{\Phi}_s$ and $\mathbf{\Phi}_u$, whose dimensions are $N \times R$, $N \times S$ and $N \times U$, respectively.

In the ICE method (Hollkamp and Gordon, 2008), the reduced equations of motion are obtained using the linear transform $\mathbf{x} = \mathbf{\Phi}_r \mathbf{r}$, such that $\mathbf{r} \approx \mathbf{q}_r$, i.e. the reduced coordinates aim to approximate the first group of modes. Then, the reduced dynamics are written as

$$\ddot{\mathbf{r}} + \mathbf{\Lambda}_r \mathbf{r} + \mathbf{f}_r(\mathbf{r}) = \mathbf{F}_r, \tag{4.4}$$

where $\mathbf{f}_r(\mathbf{r})$ is the $R \times 1$ vector of nonlinear restoring forces which must be approximated using the a static solution dataset from the full-order FE model. The coupling between $\mathbf{q}_s$ and $\mathbf{q}_r$ is approximated as *quasi-static*, and is here denoted by the $S \times 1$ vector function $\mathbf{g}$, i.e.

$$\mathbf{s} = \mathbf{g}(\mathbf{r}), \tag{4.5}$$

such that $\mathbf{s} \approx \mathbf{q}_s$. Physically, this may be interpreted as meaning that the displacement of the quasi-statically coupled modes may be determined from the displacement of the reduced modes. Then, the physical displacement of the FE model is approximated as a superposition of the reduced and the statically coupled modes, while the remaining modes are neglected ($\mathbf{u} = \mathbf{0} \approx \mathbf{q}_u$), i.e.

$$\mathbf{x} \approx \mathbf{\Phi}_r \mathbf{r} + \mathbf{\Phi}_s \mathbf{g}(\mathbf{r}). \tag{4.6}$$

As such, a reduction from N to R DOFs is achieved. It should be highlighted that, in the standard ICE method, the quasi-static coupling functions are utilised in a post-processing step to better approximate the physical deformation of the structure (equation (4.6)), yet they are not explicitly taken into account when deriving the reduced dynamics (equation (4.4)).

For the identification of $\mathbf{f}_r(\mathbf{r})$, it is typically assumed that the nonlinearities in the ROM take the same form as the nonlinearities in the full-order system; in the case of a linearly elastic FE model characterised by a quadratic strain–displacement relationship, each entry in $\mathbf{f}_r(\mathbf{r})$ then becomes a quadratic and cubic polynomial spanning the reduced modes (Mignolet *et al.*, 2013). However, as discussed in Chapter 3, to account for the effect of the statically coupled in-plane modes, the order of nonlinearity in the ROM must generally exceed that of the full-order model, such that a more robust form for $\mathbf{f}_r(\mathbf{r})$ is given by

$$\mathbf{f}_r(\mathbf{r}) = \sum_{k=2}^{K} \mathbf{A}_k \mathbf{r}^{(k)}, \tag{4.7}$$

where $\mathbf{r}^{(k)}$ is the $n_k \times 1$ vector containing all combinations of k^{th}-order monomials[1] involving the elements of $\mathbf{r}$, $\mathbf{A}_k$ is the $R \times n_k$ matrix containing the corresponding k^{th}-order coefficients in each reduced equation, $K > 3$ is the truncation order, and $n_k = \dfrac{(k+R-1)!}{k!(R-1)!}$ is the number of k^{th}-order terms in each reduced equation. Similarly,

[1] For example, for $R = 2$ i.e. $\mathbf{r} = [r_1 \quad r_2]^\mathsf{T}$: $\mathbf{r}^{(2)} = [r_1^2 \quad r_1 r_2 \quad r_2^2]^\mathsf{T}$; $\mathbf{r}^{(3)} = [r_1^3 \quad r_1^2 r_2 \quad r_1 r_2^2 \quad r_2^3]^\mathsf{T}$ etc. This notation is employed here, rather than the tensor notation introduced earlier, in order to avoid the use of very high-dimensional arrays as higher orders of nonlinearity are considered.

the quasi-static coupling functions, $\mathbf{g}(\mathbf{r})$, can be approximated as K^{th}-order polynomial functions[2] of the reduced modes, i.e.

$$\mathbf{g}(\mathbf{r}) = \sum_{k=2}^{K} \mathbf{B}_k \mathbf{r}^{(k)}, \tag{4.8}$$

where $\mathbf{B}_k$ is the $S \times n_k$ matrix containing the k^{th}-order coupling coefficients for each statically coupled mode.[3]

The linear properties in the reduced equations of motion, equations (4.4), can be computed directly using the mass and stiffness matrices of the FE model; however, the coefficients in the reduced nonlinear restoring forces, $\mathbf{f}(\mathbf{r})$, and in the quasi-static coupling functions, $\mathbf{g}(\mathbf{r})$, are computed indirectly using a set of static solution data, as detailed in Gordon and Hollkamp (2011). Each solution is obtained by applying a static force, $\mathbf{F}_{\text{st}}$, that is a linear combination of the reduction basis, $\mathbf{\Phi}_r$, and computing the corresponding static displacement, $\mathbf{x}_{\text{st}}$. The physical force to be applied is given by

$$\mathbf{F}_{\text{st}} = \mathbf{M}\mathbf{\Phi}_r \boldsymbol{\kappa} \tag{4.9}$$

where $\boldsymbol{\kappa}$ is the $R \times 1$ vector of force scaling factors, which is equivalent to the force applied in the reduced modes. After applying the static force and extracting the resulting physical displacement vector from the FE model, using a standard nonlinear solver, this may projected into the modal space using

$$\begin{bmatrix} \mathbf{r}_{\text{st}} \\ \mathbf{s}_{\text{st}} \\ \mathbf{u}_{\text{st}} \end{bmatrix} = \mathbf{\Phi}^{-1} \mathbf{x}_{\text{st}}. \tag{4.10}$$

Finally, the coefficients in $\mathbf{A}_k$ and $\mathbf{B}_k$, for $k = \{2, \ldots, K\}$, are computed in a least-squares manner according to equations (4.7) and (4.8), using datasets of $\{\boldsymbol{\kappa} - \mathbf{\Lambda}_r \mathbf{r}_{\text{st}}, \mathbf{r}_{\text{st}}\}$ and $\{\mathbf{s}_{\text{st}}, \mathbf{r}_{\text{st}}\}$, respectively. The number of unique static solutions in the datasets must be at least equal to the number of unknown coefficients in each equation. The number of unknown coefficients in equation (4.7) can be reduced by enforcing linear dependencies between elements of $\mathbf{A}_k$ such that the resulting equations of motion are consistent with an underlying elastic potential energy function.

[2] In the standard ICE method, a quadratic relationship is assumed.

[3] Note that $\mathbf{B}_1 = \mathbf{0}$ as $\mathbf{q}_r$ and $\mathbf{q}_s$ are linearly independent.

4.2.2 Motivating examples

In order to demonstrate the effectiveness as well as the shortcomings of the ICE method described above, it is used here to reduce two different FE models of a linearly elastic, geometrically nonlinear beam: one with clamped-clamped (C-C) and one with clamped-free (C-F) end conditions. The beams have a length, width and thickness of $\ell = 300\,\text{mm}$, $w = 25\,\text{mm}$ and $h = 1\,\text{mm}$, respectively, and are made of steel with a Young's modulus of 205 GPa, density of $7800\,\text{kg}\,\text{m}^{-3}$ and Poisson's ratio of 0.3. The models are constructed in the FE software Abaqus (Dassault Systèmes, 2017), and meshed with 120 three-node quadratic beam elements (Timoshenko type, B32), resulting in 1434 and 1440 DOFs for the C-C and the C-F beam, respectively. The shapes of the first three (symmetric) bending modes and the first two (symmetric) axial modes of the C-F (C-C) beam, as well as the corresponding natural frequencies, are shown in figure 4.1. The significance of these modes will be discussed later in this section.

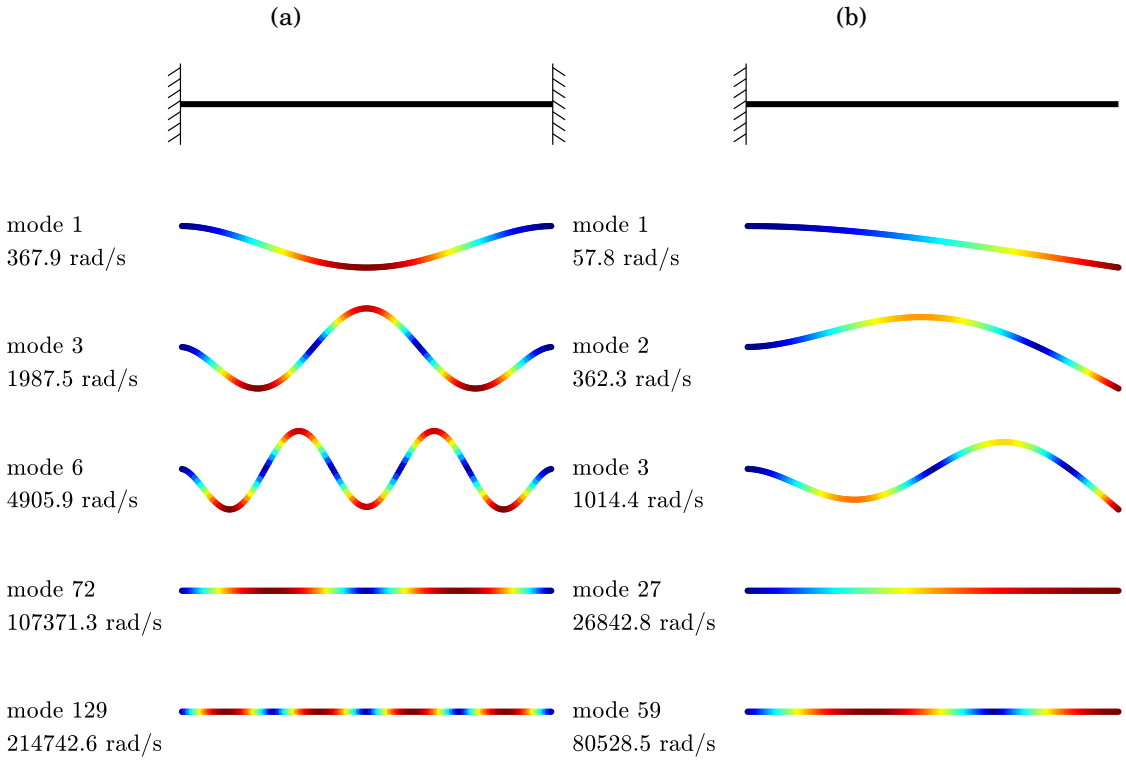

Figure 4.1. Modeshapes and natural frequencies of three bending and two axial modes of (a) the clamped-clamped beam and (b) the cantilever beam.

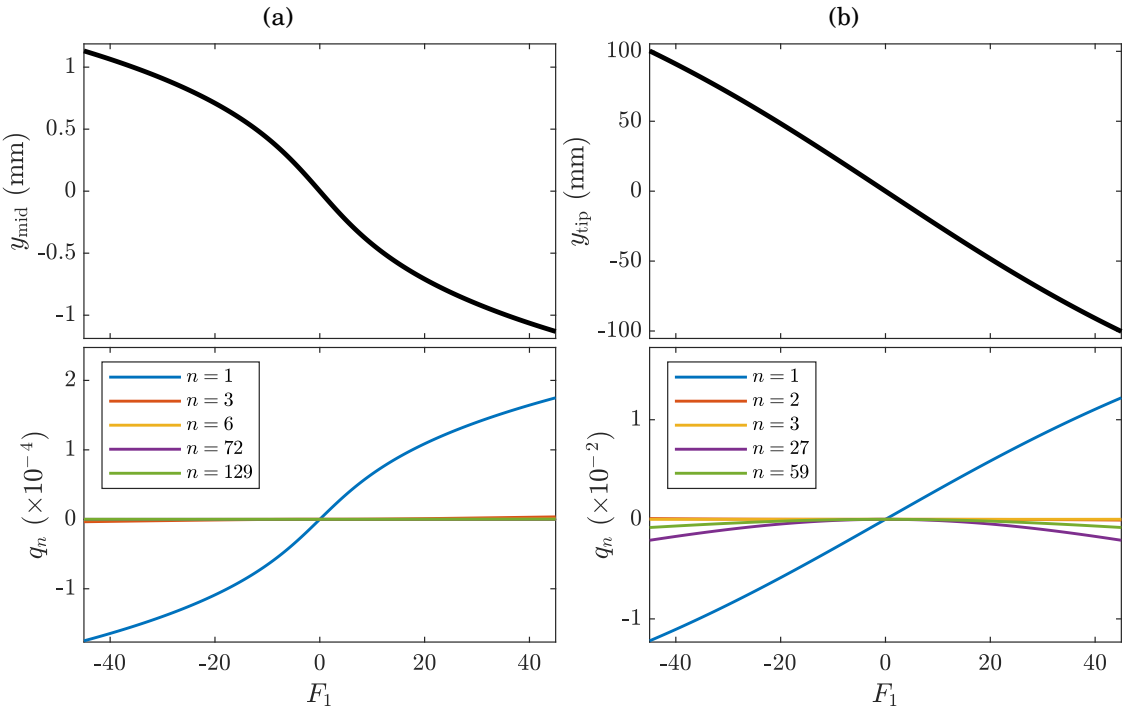

Figure 4.2. Quasi-static response of the beams as a function of the force applied in the first mode. The response is shown in the modal space (bottom panel) in terms of the reduced mode and the two most strongly coupled bending and axial modes, and in the physical space (top panel) in terms of the vertical displacement of (a) the centre node for the C-C beam, and (b) the tip node for the C-F beam.

For each FE model, a single-DOF quintic ROM of the first bending mode is constructed, according to equations (4.4) and (4.7) ($R = 1$, $\mathbf{r} \approx [q_1]$, $K = 5$), i.e.

$$\ddot{r}_1 + \omega_1^2 r_1 + A_2 r_1^2 + A_3 r_1^3 + A_4 r_1^4 + A_5 r_1^5 = F_1. \tag{4.11}$$

The static solution dataset used to identify the nonlinear coefficients, A_k, consists of four load cases, in which the force applied to the first mode, F_1, is equal to $\{-45, -22.5, +22.5, +45\}$. The quasi-static response of the beams for the range of applied loads is shown in figure 4.2, both in the physical (top) and in the modal space (bottom).[4] The maximum vertical deflection of the tip (centre) node of the C-F (C-C) beam is $y_{\text{tip}} = 100\,\text{mm} = \ell/3$ ($y_{\text{mid}} = 1.13\,\text{mm} = 1.13h$). This corresponds to a maximum von Mises stress of 421 MPa (51.3 MPa) occurring at the clamped end(s), at which point the material approaches the limit of the linearly elastic regime.

[4]Note that, in the modal space, only the response of the reduced mode and the two most strongly coupled bending and axial modes is shown.

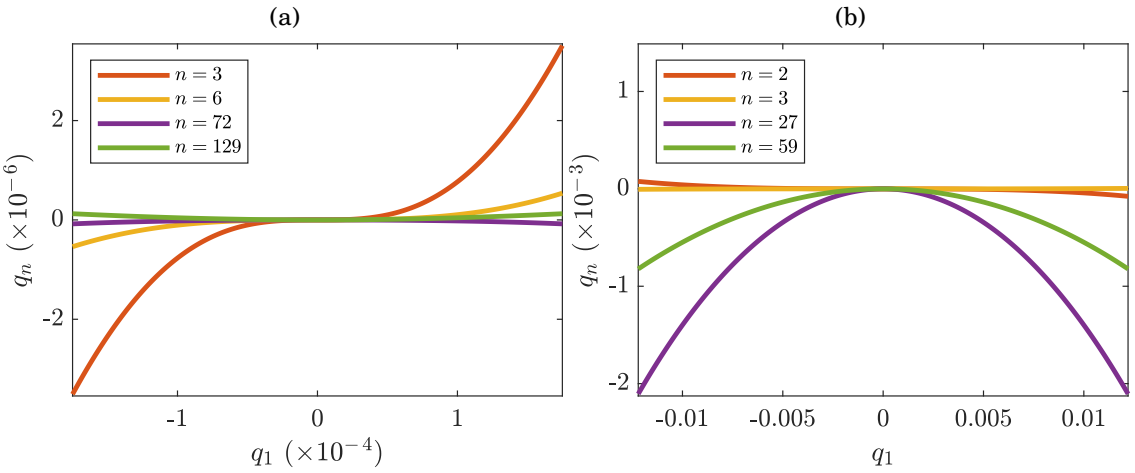

Figure 4.3. Static displacement of the relevant bending and axial modes as a function of the displacement in the first mode for (a) the C-C and (b) the C-F beam, when a force is applied in the first mode.

Figure 4.3 shows the quasi-static coupling between the reduced mode, q_1, and the two most strongly coupled bending modes, q_2 and q_3 (q_3 and q_6), as well as the two most strongly coupled axial modes, q_{27} and q_{59} (q_{72} and q_{129}), for the C-F (C-C) beam. The modal displacement amplitudes resulting from the maximum applied static force, $F_1 = 45$, normalised with respect to the largest amplitude, are listed in table 4.1. It can be seen that the first mode of the C-C beam is most strongly coupled with the third bending mode, whilst the coupling with the axial modes is less significant. Conversely, the first mode of the C-F beam exhibits weaker coupling with other bending modes, but significantly stronger coupling with axial modes; this is to be expected, as the free end of the cantilever beam allows for large in-plane displacements.

Table 4.1. Relative modal displacement amplitudes of the two most strongly coupled bending and axial modes, when a static force $F_1 = 45$ is applied in the first mode.

C-C beam	Mode no.	1	3	6	72	129
	Rel. amp.	1.0×10^{0}	2.0×10^{-2}	3.1×10^{-3}	4.5×10^{-4}	7.1×10^{-4}
C-F beam	Mode no.	1	2	3	27	59
	Rel. amp.	1.0×10^{0}	6.3×10^{-3}	3.8×10^{-4}	1.7×10^{-1}	6.7×10^{-2}

Figures 4.4 (a) and (b) show the backbone curves of the computed single-DOF ROMs of the C-C and the C-F beams, respectively, in the projection of reduced modal amplitude, R_1, against the fundamental response frequency, Ω. Both models exhibit

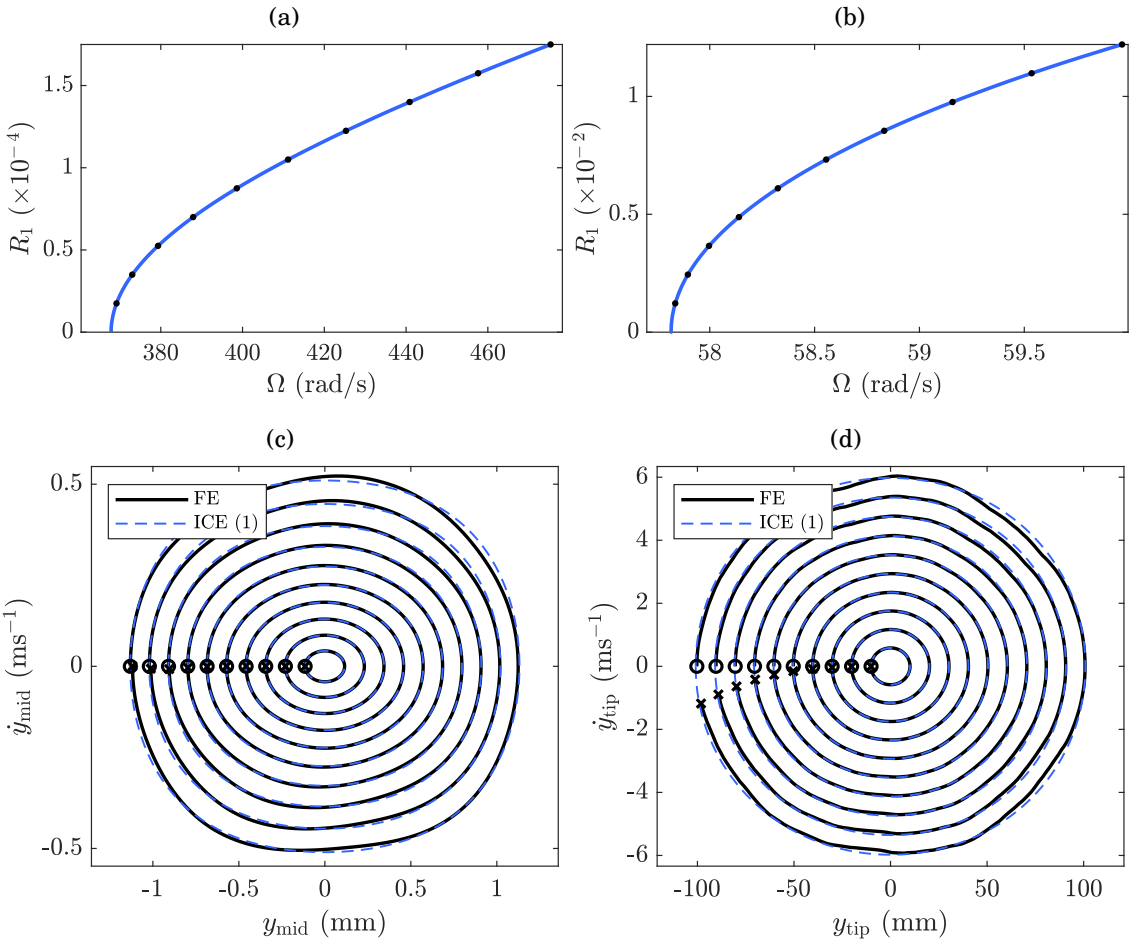

Figure 4.4. Top: first backbone curve of (a) the C-C and (b) the C-F beam, predicted by the quintic single-DOF ICE ROMs. These are plotted in the projection of response frequency against amplitude. Bottom: comparison between the periodic response predicted by the ROMs (dashed lines) and the response of the FE model (solid black line), plotted in the physical phase space, for (c) the C-C and (d) the C-F beam. Ten different sets of initial conditions are considered for each ROM, and these are marked with black dots on the backbone curves. For each free response, the FE states at time $t = 0$ and $t = T_\Omega$ are marked with circles and crosses, respectively.

hardening nonlinearities due to the effect of membrane stretching induced by the large transverse displacements. It should be highlighted that the quintic ROMs presented here were found to be robust with respect to the scaling of the static solution dataset, suggesting that a higher truncation order is not necessary, at least for the range of response amplitudes considered here. The accuracy of the ROMs is assessed by comparing different periodic solutions of the ROM, to the corresponding full-order free response of the FE model. The initial conditions of the FE model are

set using the *applied modal force* method proposed in Kuether and Allen (2014). For each ROM solution, the initial modal displacement, $\mathbf{r}_0$, which occurs at zero initial velocity, is used to compute the corresponding static modal force, i.e.

$$\mathbf{F}_{r0} = \mathbf{\Lambda}_r \mathbf{r}_0 + \mathbf{f}_r(\mathbf{r}_0). \tag{4.12}$$

This force, projected into the physical space, is then applied to the FE model, before the structure is released from its static equilibrium at time $t = 0$ and allowed to undergo free oscillation for one period of the ROM, $T_\Omega = 2\pi/\Omega$. If the state of the FE model after one ROM period coincides with its initial state, then a periodic solution is obtained and the ROM may be considered ideal. Here, the initial and final states of the FE model are compared, in order to qualitatively assess the accuracy of each ROM.

Figures 4.4 (c) and (d) show the FE response of the C-C and the C-F beam, respectively, obtained from ten different sets of initial conditions over one period based on the frequency predicted by the ROM (solid black line); the FE states at $t = 0$ and $t = T_\Omega$ are marked with black circles and crosses, respectively. The corresponding periodic ROM solutions are represented by dashed blue lines. The initial reduced modal displacements used are equally spaced and marked with black dots on the backbone curves. It can be seen that the ROM of the C-C beam can very accurately predict the response frequency of the full-order NNMs for the whole range of amplitudes considered here.[5] On the other hand, the ROM of the C-F beam appears to overestimate the frequency of the NNMs; the period predicted by the ROM is not sufficient to allow the FE model to reach its initial state and "close" the loop in the phase space. In addition, the ROM predictions become increasingly inaccurate as the response amplitude increases.

The fact that the coupling between the first and higher bending modes in the C-F beam is less significant compared to that in the C-C beam (see figure 4.3 and table 4.1), suggests that the inaccuracy of the C-F ROM is unlikely to stem from any unmodelled dynamic interaction with other low-frequency transverse modes. Instead, we suggest it is due to the classical observation for the cantilever beam, that there is competing action between the geometric nonlinearity, which is of the hardening type, and the in-plane inertia, which has a softening effect (Haight and King, 1972; Pai

[5] Note that for larger force scaling factors, which are not shown here, the modal interaction between the first mode and other bending modes, particularly the third one, becomes relatively more significant. In such cases, and/or when internal resonances are of interest, additional modes must be included in the reduction basis; this is explored in Chapter 5.

and Nayfeh, 1990; Hsieh *et al.*, 1994; Nayfeh and Mook, 1995). Since the ICE method is unable to capture the latter effect, it is perhaps not surprising that the resulting ROM leads to overpredictions of the response frequency.

To quantify the significance of the inertia of the statically coupled modes, the kinetic energy (KE) in each mass-normalised mode, which is directly related to the resulting inertial force acting on it, is considered. The normalised maximum KE in each mode during a free response of the FE model is defined as

$$\overline{\mathcal{T}}_n := \frac{\max[\mathcal{T}_n(t)]}{\max[\mathcal{T}_1(t)]} = \frac{\max\left[\dot{q}_n^2(t)\right]}{\max\left[\dot{q}_1^2(t)\right]}, \tag{4.13}$$

where $\mathcal{T}_n$ is the KE in the n^{th} mode.

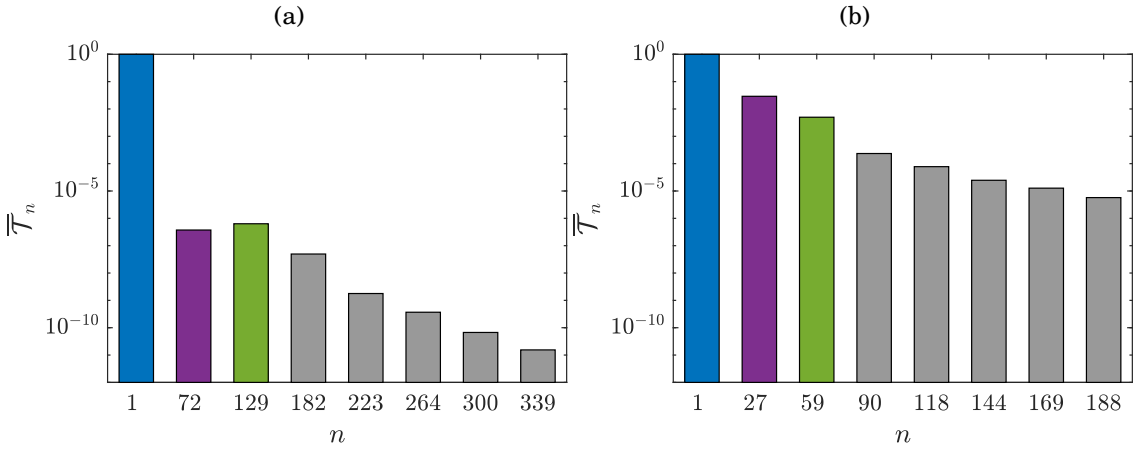

Figure 4.5. Normalised maximum kinetic energy in the first bending mode and the first seven axial modes, for (a) the C-C and (b) the C-F beam. These were computed from the free response of the FE model, where the initial conditions correspond to a static force of $F_1 \approx 45$.

Figure 4.5 shows the normalised maximum KE of the first seven axial modes of the C-C and C-F beams, for the free response with the maximum initial static force applied to the FE model. It can be seen that, for the C-C beam, the KE in the axial modes is more than six orders of magnitude smaller than that in the reduced mode. As such, the condition that in-plane inertia can be neglected, which the ICE method imposes, is a fairly good approximation. Conversely, the KE in the first axial modes of the C-F beam is much more significant; in this case, neglecting the effect of in-plane inertia leads to erroneous predictions. In the next section, a Lagrangian-based approach for deriving nonlinear reduced-order models is proposed, such that the KE of the statically coupled modes is accounted for in the reduced dynamics.

4.3 Accounting for the kinetic energy of the condensed modes

4.3.1 Proposed method

The point of departure is equation (4.3), i.e. the equations of motion of the FE model, split into the reduced, statically coupled, and unmodelled, mass-normalised modal coordinates. It is assumed that Lagrangian of the system, which underpins equation (4.3), can be expressed in terms of the categorised modal coordinates as

$$\begin{aligned}\mathcal{L} &\equiv \mathcal{T}(\dot{\mathbf{q}}_r, \dot{\mathbf{q}}_s, \dot{\mathbf{q}}_u) - \mathcal{V}(\mathbf{q}_r, \mathbf{q}_s, \mathbf{q}_u) \\ &= \frac{1}{2}(\dot{\mathbf{q}}_r)^\mathsf{T}\dot{\mathbf{q}}_r + \frac{1}{2}(\dot{\mathbf{q}}_s)^\mathsf{T}\dot{\mathbf{q}}_s + \frac{1}{2}(\dot{\mathbf{q}}_u)^\mathsf{T}\dot{\mathbf{q}}_u - \mathcal{V}(\mathbf{q}_r, \mathbf{q}_s, \mathbf{q}_u),\end{aligned} \tag{4.14}$$

where $\mathcal{T}$ and $\mathcal{V}$ denote kinetic and potential energy functions, respectively, such that

$$\frac{\partial \mathcal{V}}{\partial \mathbf{q}_r} = \mathbf{\Lambda}_r\mathbf{q}_r + \tilde{\mathbf{f}}_r(\mathbf{q}_r, \mathbf{q}_s, \mathbf{q}_u), \tag{4.15a}$$

$$\frac{\partial \mathcal{V}}{\partial \mathbf{q}_s} = \mathbf{\Lambda}_s\mathbf{q}_s + \tilde{\mathbf{f}}_s(\mathbf{q}_r, \mathbf{q}_s, \mathbf{q}_u), \tag{4.15b}$$

$$\frac{\partial \mathcal{V}}{\partial \mathbf{q}_u} = \mathbf{\Lambda}_u\mathbf{q}_u + \tilde{\mathbf{f}}_u(\mathbf{q}_r, \mathbf{q}_s, \mathbf{q}_u). \tag{4.15c}$$

Assuming that the response of the unmodelled modes ($\mathbf{q}_u$) can be neglected, the Lagrangian can be approximated as

$$\mathcal{L} \approx \hat{\mathcal{L}} = \frac{1}{2}(\dot{\mathbf{r}})^\mathsf{T}\dot{\mathbf{r}} + \frac{1}{2}(\dot{\mathbf{s}})^\mathsf{T}\dot{\mathbf{s}} - \hat{\mathcal{V}}(\mathbf{r}, \mathbf{s}), \tag{4.16}$$

where $\hat{\mathcal{V}}(\mathbf{r}, \mathbf{s}) := \mathcal{V}(\mathbf{r}, \mathbf{s}, \mathbf{0})$, such that $\mathbf{r} \approx \mathbf{q}_r$, $\mathbf{s} \approx \mathbf{q}_s$, $\mathbf{u} = \mathbf{0} \approx \mathbf{q}_u$, and

$$\frac{\partial \hat{\mathcal{V}}}{\partial \mathbf{r}} = \mathbf{\Lambda}_r\mathbf{r} + \hat{\mathbf{f}}_r(\mathbf{r}, \mathbf{s}), \tag{4.17a}$$

$$\frac{\partial \hat{\mathcal{V}}}{\partial \mathbf{s}} = \mathbf{\Lambda}_s\mathbf{s} + \hat{\mathbf{f}}_s(\mathbf{r}, \mathbf{s}), \tag{4.17b}$$

where $\hat{\mathbf{f}}_r(\mathbf{r}, \mathbf{s}) := \tilde{\mathbf{f}}_r(\mathbf{r}, \mathbf{s}, \mathbf{0})$ and $\hat{\mathbf{f}}_s(\mathbf{r}, \mathbf{s}) := \tilde{\mathbf{f}}_s(\mathbf{r}, \mathbf{s}, \mathbf{0})$. Using the quasi-static coupling approximation, $\mathbf{s} = \mathbf{g}(\mathbf{r})$, as given in equation (4.5), and noting that $\dot{\mathbf{s}} = \dfrac{\partial \mathbf{g}}{\partial \mathbf{r}}\dot{\mathbf{r}}$, equation (4.16) can be rewritten in terms of the reduced coordinates as

$$\hat{\mathcal{L}} = \frac{1}{2}(\dot{\mathbf{r}})^\mathsf{T}\dot{\mathbf{r}} + \frac{1}{2}(\dot{\mathbf{r}})^\mathsf{T}\left(\frac{\partial \mathbf{g}}{\partial \mathbf{r}}\right)^\mathsf{T}\frac{\partial \mathbf{g}}{\partial \mathbf{r}}\dot{\mathbf{r}} - \hat{\mathcal{V}}(\mathbf{r}, \mathbf{g}(\mathbf{r})). \tag{4.18}$$

From this, the partial derivatives of $\hat{\mathcal{L}}$ with respect to $\dot{\mathbf{r}}$ and $\mathbf{r}$, can be written, respectively, as

$$\frac{\partial \hat{\mathcal{L}}}{\partial \dot{\mathbf{r}}} = \dot{\mathbf{r}} + \left(\frac{\partial \mathbf{g}}{\partial \mathbf{r}}\right)^\mathsf{T}\frac{\partial \mathbf{g}}{\partial \mathbf{r}}\dot{\mathbf{r}} \tag{4.19a}$$

$$\frac{\partial \hat{\mathcal{L}}}{\partial \mathbf{r}} = \left(\frac{\partial \mathbf{g}}{\partial \mathbf{r}}\right)^\mathsf{T}\frac{\partial^2 \mathbf{g}}{\partial \mathbf{r}^2}\dot{\mathbf{r}}\dot{\mathbf{r}} - \left(\mathbf{\Lambda}_r\mathbf{r} + \hat{\mathbf{f}}_r(\mathbf{r}, \mathbf{g})\right) - \left(\frac{\partial \mathbf{g}}{\partial \mathbf{r}}\right)^\mathsf{T}\left(\mathbf{\Lambda}_s\mathbf{g} + \hat{\mathbf{f}}_s(\mathbf{r}, \mathbf{g})\right). \tag{4.19b}$$

According to the Euler-Lagrange equation, the reduced equations of motion can be written as

$$\frac{\mathrm{d}}{\mathrm{d}t}\left(\frac{\partial \hat{\mathcal{L}}}{\partial \dot{\mathbf{r}}}\right) - \frac{\partial \hat{\mathcal{L}}}{\partial \mathbf{r}} = \mathbf{F}_r. \tag{4.20}$$

Substituting equations (4.19) into equation (4.20) leads to, after some algebraic manipulation,

$$\ddot{\mathbf{r}} + \left(\frac{\partial \mathbf{g}}{\partial \mathbf{r}}\right)^{\mathsf{T}} \frac{\partial \mathbf{g}}{\partial \mathbf{r}}\ddot{\mathbf{r}} + \left(\frac{\partial \mathbf{g}}{\partial \mathbf{r}}\right)^{\mathsf{T}} \frac{\partial^2 \mathbf{g}}{\partial \mathbf{r}^2}\dot{\mathbf{r}}\dot{\mathbf{r}} + \boldsymbol{\Lambda}_r \mathbf{r} + \mathbf{f}_r(\mathbf{r}) = \mathbf{F}_r, \tag{4.21}$$

where $\mathbf{f}_r(\mathbf{r}) := \hat{\mathbf{f}}_r(\mathbf{r},\mathbf{g}) + \left(\frac{\partial \mathbf{g}}{\partial \mathbf{r}}\right)^{\mathsf{T}} \left(\boldsymbol{\Lambda}_s \mathbf{g} + \hat{\mathbf{f}}_s(\mathbf{r},\mathbf{g})\right)$. By definition, $\mathbf{g}(\mathbf{r})$ must satisfy

$$\boldsymbol{\Lambda}_s \mathbf{g} + \hat{\mathbf{f}}_s(\mathbf{r},\mathbf{g}) = \mathbf{0}, \tag{4.22}$$

as it is computed based on static solution data where only the reduced modes are directly forced, while the response of the quasi-statically coupled modes is captured implicitly. As such, the second term in $\mathbf{f}_r(\mathbf{r})$ may be neglected, i.e. $\mathbf{f}_r(\mathbf{r}) = \hat{\mathbf{f}}_r(\mathbf{r},\mathbf{g})$. As with the ICE method (equation (4.4)), the reduced coordinates are related to the FE coordinates through equation (4.6), such that the number of DOFs is reduced from N to R. As with equation (4.4), equation (4.21) can be solved using numerical tools such as continuation.

4.3.2 Indirect methods and nonlinear manifolds

The ROM obtained using the proposed method, equation (4.21), may be considered as a natural extension to the ICE ROM, equation (4.4). In both cases, the expressions for the nonlinear restoring forces, $\mathbf{f}_r(\mathbf{r})$, are equivalent and can be approximated as polynomial functions in $\mathbf{r}$ (see equation (4.7)), whose order may generally exceed the order of nonlinearity in the full-order model.[6] However, when the kinetic energy of the in-plane modes is taken into account, two additional terms emerge in the reduced equations of motion: a configuration-dependent inertial term, $\left(\frac{\partial \mathbf{g}}{\partial \mathbf{r}}\right)^{\mathsf{T}} \frac{\partial \mathbf{g}}{\partial \mathbf{r}}\ddot{\mathbf{r}}$, and a convective term, $\left(\frac{\partial \mathbf{g}}{\partial \mathbf{r}}\right)^{\mathsf{T}} \frac{\partial^2 \mathbf{g}}{\partial \mathbf{r}^2}\dot{\mathbf{r}}\dot{\mathbf{r}}$. The coefficients of both terms can be expressed in terms of the precomputed quasi-static coupling coefficients, $\mathbf{B}_k$, which define the relationship between the reduced and the statically coupled coordinates (equation (4.8)). As such, the proposed reduction method does not require that any additional information be

[6] The higher-order nonlinear terms may be necessary to accurately capture the effect of the geometric nonlinearity related to the quasi-static coupling between the low-frequency transverse modes and the high-frequency in-plane modes, as discussed in Chapter 3.

extracted from the FE model; instead, the existing information is used, after some computationally cheap post-processing, to enrich the reduced dynamics. The inclusion of these additional terms in the reduced dynamics will be referred to as *inertial compensation*, and the corresponding model, i.e. equation (4.21), will be referred to as ICE-IC ROM. A schematic of the ROM generation procedure using the ICE-IC method is shown in figure 4.6, where the extension proposed here is represented in red.

The importance of retaining the effect of in-plane inertia, compared to the static condensation approach, has previously been demonstrated using the concept of modal derivatives and the quadratic manifold (Rutzmoser *et al.*, 2014; Jain *et al.*, 2017). In the quadratic manifold approach, reduction is achieved through a nonlinear mapping between the FE coordinates and a small set of modal coordinates; the mapping is quadratic, and it is defined such that its gradient is given by linear modeshapes, and its curvature is given by modal derivatives. Whilst this approach was found to provide excellent accuracy in some cases, its applicability is limited to structures characterised by von Kármán kinematics, and in which the dominant source of nonlinearity is membrane stretching (Rutzmoser *et al.*, 2017; Jain *et al.*, 2017). Compared to the quadratic manifold approach, the merits of the ICE-IC method are twofold. Firstly, the relationship between the reduced and the statically coupled modes is not limited to being quadratic, which allows the method to be applied to a broader range of structures. In addition, the proposed method is non-intrusive in nature, and can be applied using any commercial FE software package. Nevertheless, the inertial compensation approach aligns with the idea underpinning nonlinear manifolds; in fact, it can be shown that the reduced equations of motion derived through a general, not necessarily quadratic, nonlinear projection, are equivalent to equations (4.21); this is demonstrated in section 4.3.2.1 below.

The more general concept of invariant manifolds based on the theory of normal forms has been utilised, under its asymptotic formulation, for the reduction of thin shells and beams (Shaw and Pierre, 1993, 1994; Hsieh *et al.*, 1994; Shaw *et al.*, 1999; Pesheck *et al.*, 2001; Touzé *et al.*, 2004b,a, 2008; Touzé and Thomas, 2004; Touzé and Amabili, 2006). The invariant manifold approach has the added capacity to allow for coupling between modal displacements and modal velocities, whereas in the proposed method, quasi-static coupling is assumed. However, it has been observed that, for non-gyroscopic, conservative systems, any velocity dependence can be neglected without much loss of accuracy (Hsieh *et al.*, 1994; Shaw *et al.*,

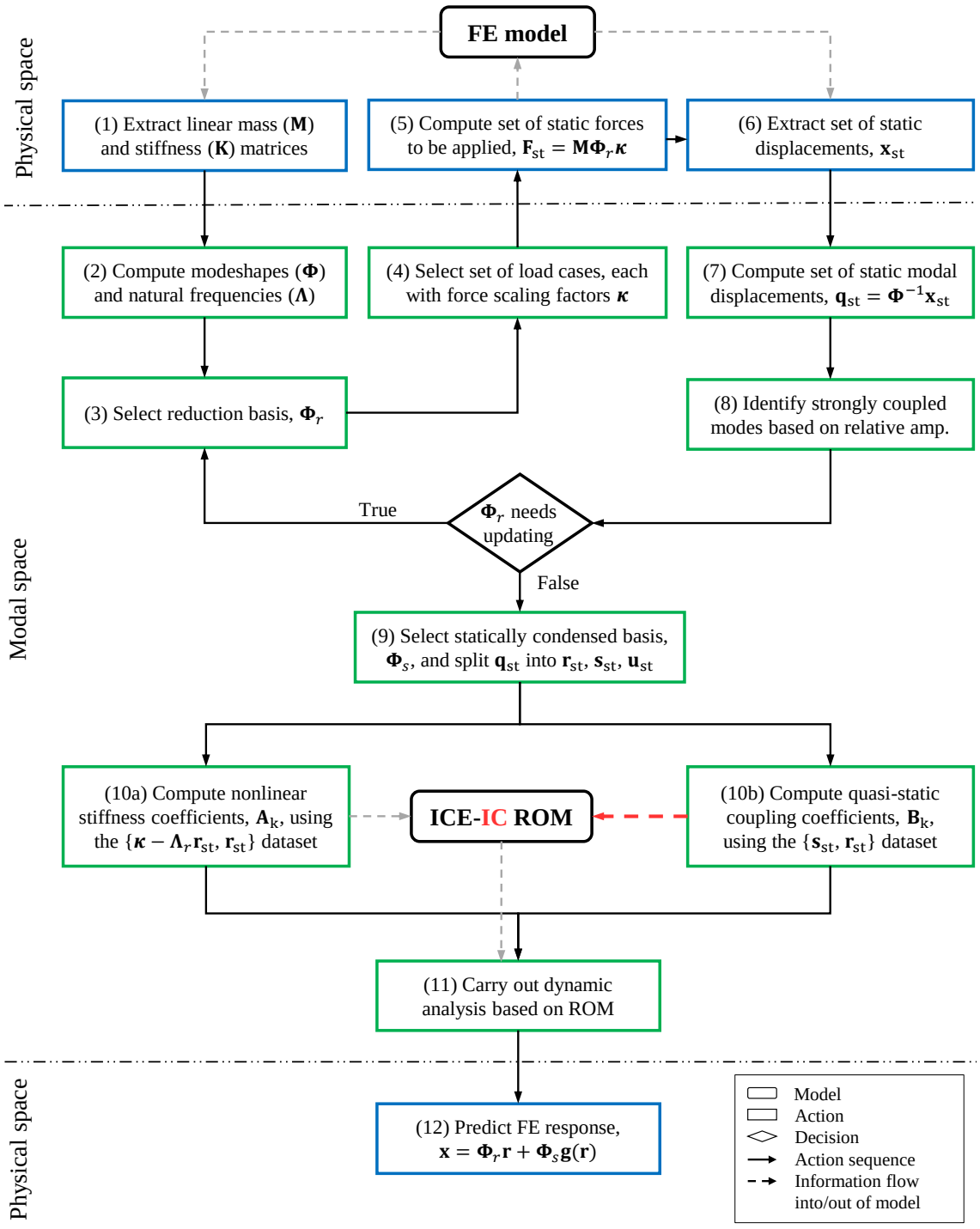

Figure 4.6. Schematic of the ROM generation procedure using the ICE method, with the schematically modest, but dynamically significant, proposed changes to incorporate inertial compensation shown in red.

1999), making the aforementioned assumption a good approximation. On the other hand, the main limitation of the invariant manifold approach is its high algebraic complexity, which makes the derivation of expressions for manifolds of order higher than cubic, intractable (Touzé *et al.*, 2004b). Even though third-order invariant manifolds can very accurately capture the NNMs of the full-order system at moderate amplitudes, the results deteriorate rapidly beyond a certain amplitude, where higher-order nonlinear terms are necessary to capture the reduced dynamics (Touzé and Thomas, 2004; Touzé *et al.*, 2004a,b). With the proposed method, this issue does not occur, since the coefficients of the nonlinear functions in the equations of motion are computed *indirectly* via regression analysis, using a set of static solutions of the full-order system. As a result, the expressions that *directly* relate the coefficients of the full-order system to those of the ROM need not be derived, and thus higher orders of nonlinearity can easily be considered.

4.3.2.1 Equivalence of approaches

This section demonstrates that the Lagrangian-based approach presented in section 4.3.1, is equivalent to projecting the equations of motion of the full-order system onto an underlying nonlinear manifold. We start by considering the equations of motion of the full-order model, split into the reduced, statically coupled, and unmodelled modal coordinates, i.e. equation (4.3). When the response of the third group of modes is neglected, the full-order equations of motion can be approximated[7] as

$$\begin{bmatrix} \ddot{\mathbf{r}} \\ \ddot{\mathbf{s}} \end{bmatrix} + \begin{bmatrix} \mathbf{\Lambda}_r & \mathbf{0} \\ \mathbf{0} & \mathbf{\Lambda}_s \end{bmatrix} \begin{bmatrix} \mathbf{r} \\ \mathbf{s} \end{bmatrix} + \begin{bmatrix} \hat{\mathbf{f}}_r(\mathbf{r},\mathbf{s}) \\ \hat{\mathbf{f}}_s(\mathbf{r},\mathbf{s}) \end{bmatrix} = \begin{bmatrix} \mathbf{F}_r \\ \mathbf{0} \end{bmatrix}. \tag{4.23}$$

Then, since the coordinates in $\mathbf{s}$ are assumed to be statically coupled to the coordinates in $\mathbf{r}$ (equation (4.5)), the system can be reduced using a nonlinear mapping $\mathbf{\Gamma}$, defined as

$$\begin{bmatrix} \mathbf{r} \\ \mathbf{s} \end{bmatrix} = \begin{bmatrix} \mathbf{r} \\ \mathbf{g}(\mathbf{r}) \end{bmatrix} = \mathbf{\Gamma}(\mathbf{r}). \tag{4.24}$$

[7] Note that this is equivalent to applying the Euler-Lagrange equation to the approximated Lagrangian, equation (4.16).

Differentiating this twice with respect to time, leads to

$$\begin{bmatrix} \dot{\mathbf{r}} \\ \dot{\mathbf{s}} \end{bmatrix} = \frac{\partial \boldsymbol{\Gamma}}{\partial \mathbf{r}} \dot{\mathbf{r}}, \tag{4.25a}$$

$$\begin{bmatrix} \ddot{\mathbf{r}} \\ \ddot{\mathbf{s}} \end{bmatrix} = \frac{\partial \boldsymbol{\Gamma}}{\partial \mathbf{r}} \ddot{\mathbf{r}} + \frac{\partial^2 \boldsymbol{\Gamma}}{\partial \mathbf{r}^2} \dot{\mathbf{r}} \dot{\mathbf{r}}, \tag{4.25b}$$

where $\dfrac{\partial \boldsymbol{\Gamma}}{\partial \mathbf{r}}$ and $\dfrac{\partial^2 \boldsymbol{\Gamma}}{\partial \mathbf{r}^2}$ are arrays with dimensions of $(R+S)\times R$ and $(R+S)\times R \times R$, respectively. These can be expressed as

$$\frac{\partial \boldsymbol{\Gamma}}{\partial \mathbf{r}} = \begin{bmatrix} \mathbf{I} \\ \dfrac{\partial \mathbf{g}}{\partial \mathbf{r}} \end{bmatrix}, \tag{4.26a}$$

$$\frac{\partial^2 \boldsymbol{\Gamma}}{\partial \mathbf{r}^2} = \begin{bmatrix} \mathbf{0} \\ \dfrac{\partial^2 \mathbf{g}}{\partial \mathbf{r}^2} \end{bmatrix}, \tag{4.26b}$$

where $\dfrac{\partial \mathbf{g}}{\partial \mathbf{r}}[i,j] = \dfrac{\partial g_i}{\partial r_j}$, $\dfrac{\partial^2 \mathbf{g}}{\partial \mathbf{r}^2}[i,j,k] = \dfrac{\partial^2 g_i}{\partial r_j \partial r_k}$, $\mathbf{I}$ is the $R \times R$ identity matrix and $\mathbf{0}$ is the $R \times R \times R$ zero tensor. Substituting equations (4.24) and (4.25) into equation (4.23) and premultiplying by the transpose of the tangent subspace,[8] $\left(\dfrac{\partial \boldsymbol{\Gamma}}{\partial \mathbf{r}}\right)^{\mathsf{T}}$, leads to

$$\left(\frac{\partial \boldsymbol{\Gamma}}{\partial \mathbf{r}}\right)^{\mathsf{T}} \left[\frac{\partial \boldsymbol{\Gamma}}{\partial \mathbf{r}} \ddot{\mathbf{r}} + \left(\frac{\partial^2 \boldsymbol{\Gamma}}{\partial \mathbf{r}^2} \dot{\mathbf{r}}\right) \dot{\mathbf{r}}\right] + \left(\frac{\partial \boldsymbol{\Gamma}}{\partial \mathbf{r}}\right)^{\mathsf{T}} \begin{bmatrix} \boldsymbol{\Lambda}_r & \mathbf{0} \\ \mathbf{0} & \boldsymbol{\Lambda}_s \end{bmatrix} \boldsymbol{\Gamma} + \left(\frac{\partial \boldsymbol{\Gamma}}{\partial \mathbf{r}}\right)^{\mathsf{T}} \begin{bmatrix} \hat{\mathbf{f}}_r(\mathbf{r},\mathbf{g}) \\ \hat{\mathbf{f}}_s(\mathbf{r},\mathbf{g}) \end{bmatrix} = \left(\frac{\partial \boldsymbol{\Gamma}}{\partial \mathbf{r}}\right)^{\mathsf{T}} \begin{bmatrix} \mathbf{F}_r \\ \mathbf{0} \end{bmatrix}. \tag{4.27}$$

Finally, after substituting equations (4.26) into equation (4.27), and some algebraic manipulation, equation (4.21) is obtained.

4.4 Application to the cantilever beam

We now revisit the FE model of the cantilever beam considered in section 4.2.2 (figure 4.1 (b)), for which the standard ICE method resulted in inaccurate response predictions. Reduced-order models obtained using the standard ICE method, equation (4.4), are compared with those obtained using the extended ICE-IC method, equation (4.21). The first and second backbone curves of the cantilever beam are considered separately in the following subsections.

[8] This ensures that the residual introduced by the projection approximation is orthogonal to the kinematically admissible displacements (Jain *et al.*, 2017; Rutzmoser *et al.*, 2017).

4.4.1 First backbone curve

As in section 4.2.2, single-DOF quintic ROMs of the first mode are considered. The standard ICE ROM is described by equation (4.11), whilst the ICE-IC ROM includes some additional terms to account for the kinetic energy of the statically coupled modes, i.e.

$$\left[1+\sum_i\left(\frac{\partial g_i}{\partial r_1}\right)^2\right]\ddot{r}_1+\sum_i\frac{\partial g_i}{\partial r_1}\frac{\partial^2 g_i}{\partial r_1^2}\dot{r}_1^2+\omega_1^2 r_1+A_2r_1^2+A_3r_1^3+A_4r_1^4+A_5r_1^5=F_1, \quad (4.28)$$

where $g_i(r_1)=s_i=B_2^{(i)}r_1^2+B_3^{(i)}r_1^3+B_4^{(i)}r_1^4+B_5^{(i)}r_1^5$ and i spans the indices of the statically coupled modes. In this case, only the three most strongly coupled axial modes are included in the statically coupled basis (i.e. $S=3$, $\mathbf{s}\approx[q_{27}\quad q_{59}\quad q_{90}]^\intercal$). The coefficients in the quasi-static coupling functions, $\mathbf{B}_k$, are computed according to equation (4.8) using the same static solution dataset that is used to compute the nonlinear stiffness coefficients, $\mathbf{A}_k$. As before, this consists of four load cases, where the applied force in the first mode is $F_1=\{-45,-22.5,+22.5,+45\}$. The resulting quasi-static behaviour of the cantilever beam for the range of applied loads is shown in figures 4.2 (b) and 4.3 (b).

Figure 4.7 (a) shows the computed backbone curves of the ICE (blue) and ICE-IC (red) ROMs. It can be seen that the inertial compensation terms have a softening effect on the model, bringing the nonlinear response frequency very close to the underlying linear natural frequency even at large vibration amplitudes; this observation is consistent with results in the literature (Haight and King, 1972; Touzé and Thomas, 2004; Pai, 2007). As in section 4.2.2, the accuracy of each ROM is estimated by computing the free response of the FE model with the initial conditions and period of integration predicted by the ROM. The results obtained from ten different free response runs are shown in figures 4.7 (b) and (c) for the ICE and ICE-IC ROM, respectively. It can be seen that the novel ROM is able to predict the response frequency of the first NNM of the cantilever beam remarkably well, as it gives rise to nearly perfect free response loops in the phase space, for the whole range of amplitudes considered here. It should be noted that, for this system, the computational cost associated with solving the equations of motion of the ICE-IC ROM using the MATLAB built-in ode45 solver, is increased only by $\sim 4\%$ relative to the ICE ROM.

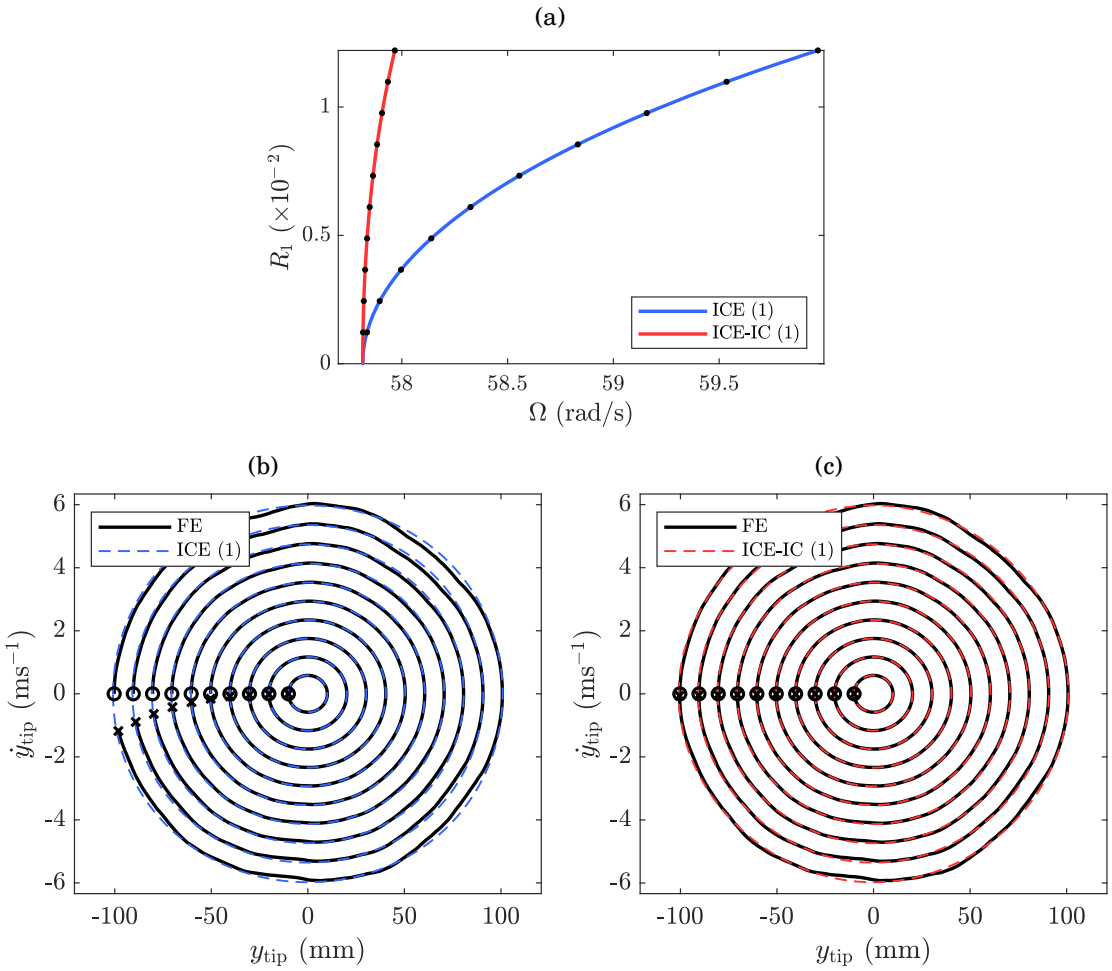

Figure 4.7. (a) First backbone curve of the C-F beam, predicted by the quintic single-DOF ROMs without (blue) and with (red) inertial compensation. These are plotted in the projection of response frequency against amplitude. Bottom: comparison between the periodic response predicted by the ROMs (dashed lines) and the response of the FE model (solid black line), plotted in the physical phase space, for (b) the ICE ROM and (c) the ICE-IC ROM. Ten different sets of initial conditions are considered for each ROM, and these are marked with black dots on the backbone curves. For each free response, the FE states at time $t = 0$ and $t = T_\Omega$ are marked with circles and crosses, respectively.

4.4.2 Second backbone curve

We now consider the second backbone curve of the cantilever beam by computing 2-DOF quintic ROMs. Since the natural frequencies of the first two modes are not well-separated, the dynamics of the first mode can be neither statically condensed nor neglected when computing the second backbone curve; as such, both modes must

be included in the reduction basis. As before, the statically coupled basis consists of the 27^{th}, 59^{th} and 90^{th} modes. The 2-DOF equations of motion for the ICE and ICE-IC ROMs are given, respectively, by

$$\begin{bmatrix} \ddot{r}_1 \\ \ddot{r}_2 \end{bmatrix} + \begin{bmatrix} \omega_1^2 & 0 \\ 0 & \omega_2^2 \end{bmatrix} \begin{bmatrix} r_1 \\ r_2 \end{bmatrix} + \begin{bmatrix} f_{r1}(r_1, r_2) \\ f_{r2}(r_1, r_2) \end{bmatrix} = \begin{bmatrix} F_1 \\ F_2 \end{bmatrix} \tag{4.29}$$

and

$$\begin{bmatrix} \ddot{r}_1 \\ \ddot{r}_2 \end{bmatrix} + \begin{bmatrix} \omega_1^2 & 0 \\ 0 & \omega_2^2 \end{bmatrix} \begin{bmatrix} r_1 \\ r_2 \end{bmatrix} + \begin{bmatrix} f_{r1}(r_1, r_2) \\ f_{r2}(r_1, r_2) \end{bmatrix} + \sum_i \begin{bmatrix} \left(\frac{\partial g_i}{\partial r_1}\right)^2 & \frac{\partial g_i}{\partial r_1}\frac{\partial g_i}{\partial r_2} \\ \frac{\partial g_i}{\partial r_1}\frac{\partial g_i}{\partial r_2} & \left(\frac{\partial g_i}{\partial r_2}\right)^2 \end{bmatrix} \begin{bmatrix} \ddot{r}_1 \\ \ddot{r}_2 \end{bmatrix}$$
$$+ \sum_i \begin{bmatrix} \frac{\partial g_i}{\partial r_1} \\ \frac{\partial g_i}{\partial r_2} \end{bmatrix} \left(\frac{\partial^2 g_i}{\partial r_1^2}\dot{r}_1^2 + 2\frac{\partial^2 g_i}{\partial r_1 \partial r_2}\dot{r}_1\dot{r}_2 + \frac{\partial^2 g_i}{\partial r_2^2}\dot{r}_2^2 \right) = \begin{bmatrix} F_1 \\ F_2 \end{bmatrix}, \tag{4.30}$$

where f_{r1}, f_{r2} and g_i are fifth-order nonlinear polynomial functions of r_1 and r_2.

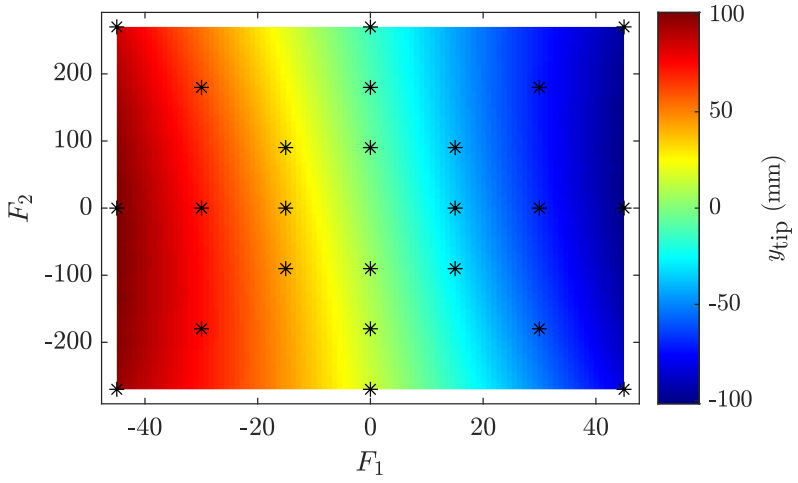

Figure 4.8. Plot of the vertical displacement of the tip of the C-F beam, as a function of the static forces applied to the first and second modes. The load cases used for calibrating the 2-DOF ROMs are marked with black asterisks.

The coefficients in the nonlinear stiffness functions and in the quasi-static coupling functions were computed using a set of 24 unique static solutions of the FE model. The distribution of the static loads applied in each mode, as well as the corresponding static displacement of the tip node, are shown in figure 4.8. The magnitude of the maximum load applied in the second mode, $F_2 = 270$, was set to four times that

in the first mode, $F_1 = 45$.[9] Table 4.2 shows the relative displacement amplitudes of the reduced modes (q_1, q_2), as well as the most strongly coupled bending mode (q_3) and axial modes (q_{27}, q_{59}), for four of the considered load cases. It can be seen that, when a force is applied in the second mode, the response of the first mode is significant, which suggests that it must be retained in the reduction basis. As before, the coupling with higher transverse modes is weak, whilst the lowest axial modes are strongly coupled and are thus included in the statically coupled basis.

Table 4.2. Relative modal displacement amplitudes of the most strongly coupled bending and axial modes, for different combinations of static forces applied in the first and second modes.

		Mode number				
F_1	F_2	1	2	3	27	59
0	270	1.2×10^{-1}	1.0×10^{0}	2.9×10^{-3}	1.5×10^{-1}	5.2×10^{-2}
45	0	1.0×10^{0}	6.3×10^{-3}	3.8×10^{-4}	1.7×10^{-1}	6.7×10^{-2}
45	-270	1.0×10^{0}	1.6×10^{-1}	1.4×10^{-3}	1.7×10^{-1}	2.3×10^{-2}
45	270	1.0×10^{0}	1.7×10^{-1}	5.9×10^{-3}	1.9×10^{-1}	1.2×10^{-1}

Figures 4.9 (a) and (b) show the second backbone curve of the computed 2-DOF ROMs of the C-F beam, shown in the projection of the amplitude of each retained mode against response frequency. It can be seen that, as expected, the traditional ICE ROM fails to capture the softening behaviour of the second NNM, which arises due to the effect of in-plane inertia. The dominance of the inertial over the geometric nonlinearities in the second backbone curve, as well as in all higher backbone curves of the cantilever beam, is a classical observation in the literature (Haight and King, 1972; Pai and Nayfeh, 1990; Hsieh *et al.*, 1994; Nayfeh and Mook, 1995; Touzé and Thomas, 2004; Pai, 2007).

Figures 4.9 (c) and (d) show the phase space plots of ten different free response runs of the FE model, with the initial conditions and period of integration predicted by the ICE and ICE-IC ROMs, respectively. In the case of the ICE ROM, it can be observed that not only is the response frequency overestimated, but the initial conditions predicted by the ROM are such that the full-order response is not periodic, regardless of the period of integration, i.e. the loops gradually shift in phase space.

[9] Even though the relative scaling of the applied loads was chosen semi-arbitrarily, *a posteriori* computations have confirmed that the ROMs are not greatly dependent on the precise tuning of force scaling factors; as discussed in Chapter 3, this is related to the higher orders of nonlinearity considered in the ROMs.

Conversely, the periodic solutions predicted by the ICE-IC ROM satisfy the FE model with excellent accuracy.

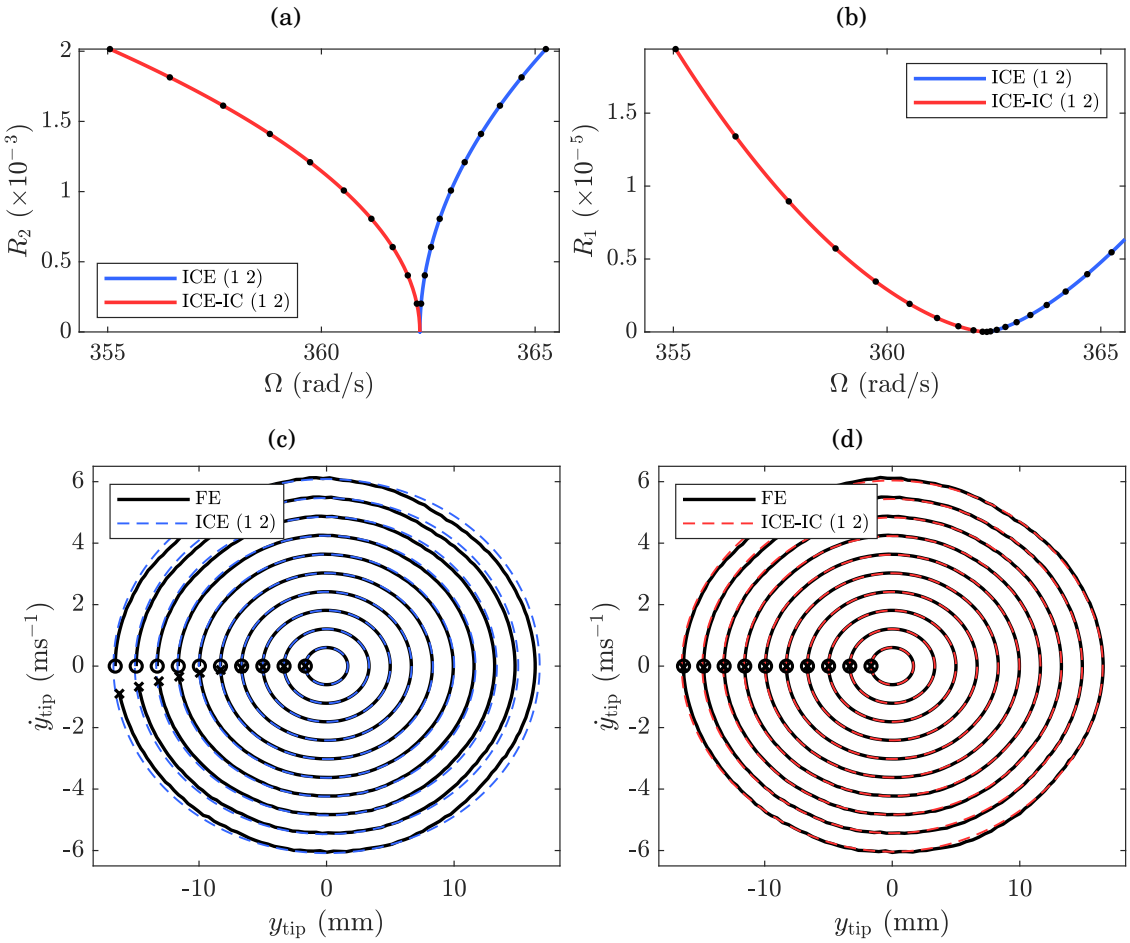

Figure 4.9. Top: second backbone curve of the C-F beam, predicted by the quintic 2-DOF ROMs without (blue) and with (red) inertial compensation. These are plotted in the projection of response frequency against (a) amplitude of the second mode, and (b) amplitude of the first mode. Bottom: comparison between the periodic response predicted by the ROMs (dashed lines) and the response of the FE model (solid black line), plotted in the physical phase space, for (c) the ICE ROM and (d) the ICE-IC ROM. Ten different sets of initial conditions are considered for each ROM, and these are marked with black dots on the backbone curves. For each free response, the FE states at time $t = 0$ and $t = T_\Omega$ are marked with circles and crosses, respectively. The numbers in brackets in the legends denote the modes included in the reduction basis.

4.5 Summary

This chapter has investigated a fundamental assumption underpinning force-based indirect reduction methods such as the ICE, which states that the inertia of the condensed modes is negligible. The effectiveness as well as the limitations of the ICE method, have been demonstrated using a clamped-clamped beam and a cantilever beam, respectively. It has been shown that, in the latter application, the large in-plane displacements can give rise to significant amounts of kinetic energy in the high-frequency, statically coupled axial modes. Due to this non-negligible in-plane inertia, the ICE method gives rise to results which are quantitatively and qualitatively inaccurate. Using a Lagrangian approach, it has been demonstrated that the effect of the in-plane kinetic energy can be accounted for in the reduced dynamics. This gives rise to additional terms in the reduced equations of motion, relative to the standard ICE ROM, which are referred to as *inertial compensation*; the proposed extended method is referred to as ICE-IC.

The additional functions in the ICE-IC ROM are formulated using the existing static solution dataset that is used to calibrate the standard ROM. Specifically, the additional terms are expressed in terms of the functions which describe the quasi-static coupling between the dynamically important transverse modes and the statically coupled in-plane modes; these are used in the *expansion* step of the standard ICE method in order to recover the physical displacement of the full-order model, but they do not influence the reduced dynamics. The proposed method has been demonstrated using an FE model of a cantilever beam, and excellent accuracy has been observed. In practical applications, the inertial compensation approach can significantly improve the accuracy and efficiency of ROMs of engineering structures which have similar properties to a cantilever beam, such as wind turbine blades and flexible wings, as well as any other structures where a significant amount of kinetic energy is present in the condensed modes.

Chapter 5

Detecting internal resonances

Previous chapters have considered how a geometrically nonlinear dynamical system can be reduced based on a static condensation procedure, whereby in-plane modes are assumed to be quasi-statically coupled to a small set of transverse modes, with the latter group forming the reduction basis. This approach is mathematically justifiable for structures characterised by slow/fast dynamics, such as thin plates and slender beams, and has been shown to provide highly accurate results. Nevertheless, selecting an appropriate reduction basis without *a priori* knowledge of the full-order dynamics remains a challenge. Retaining redundant modes will lead to computationally suboptimal reduced-order models, whilst omitting dynamically significant modes will lead to inaccurate results, and important features such as internal resonances may not be captured. This chapter demonstrates how the error associated with static condensation can be efficiently approximated during model order reduction. This approximate error can then be used as the basis of a method for predicting when dynamic modal interactions will occur, which will guide the reduction basis selection process. Equivalently, this may serve as a tool for verifying the accuracy of ROMs without the need for full-order simulations. The proposed method is demonstrated using a simple oscillator, as well as an FE model of a clamped-clamped beam.

Publication resulting from this work

Nicolaidou, E., Hill, T. L., and Neild, S. A. (2021). Detecting internal resonances during model reduction. *Proceedings of the Royal Society A: Mathematical, Physical and Engineering Sciences*, 477(2250):20210215

5.1 Introduction

As previously discussed in section 2.1, the modal couplings in nonlinear dynamical systems foster energy exchange between modes and can give rise to complex behaviours which have no linear counterparts, such as jump phenomena (Nayfeh and Mook, 1995; Brennan *et al.*, 2008), limit cycle oscillations (Patil *et al.*, 2001; Thothadri and Moon, 2005), and internal resonances (Amabili *et al.*, 2000; Vakakis *et al.*, 2001). An internal resonance is a phenomenon which occurs when the nonlinear response frequencies of different modes is commensurate, allowing for significantly enhanced energy transfer between them. This effect can be exploited for practical applications such as energy harvesting using electromagnetic and piezoelectric devices (Chen and Jiang, 2015; Lan *et al.*, 2015), and for enhanced stable micromechanical oscillators (Antonio *et al.*, 2012; Chen *et al.*, 2017). As such, the ability to reliably identify and model such behaviours during model order reduction is of great importance.

Chapters 3 and 4 have addressed some of the main limitations of force-based indirect reduction methods, which are associated with the lack of invariance of the reduced subspace. Specifically, it was shown how, for a given reduction basis, reduction can be achieved in a non-intrusive, accurate and efficient manner. Nevertheless, selecting an appropriate reduction basis without *a priori* knowledge of the full-order dynamics remains a challenge. Retaining redundant modes will lead to computationally suboptimal ROMs, whilst omitting dynamically significant modes will lead to inaccurate results, and important features such as internal resonances may not be captured. In other words, the ICE method relies on a slow/fast decomposition and is unable to capture any internal resonances between the reduced and condensed modes (Shen *et al.*, 2021).

This chapter aims to address this challenge by developing a method which can be used to predict the existence of internal resonances in conservative systems, and thus guide the reduction basis selection process, without the need for full-order simulations. Specifically, each condensed coordinate is represented as the superposition of two components: one that is statically coupled to the reduced coordinates, and one that is dynamically independent of them; the latter may be considered as the error associated with the static condensation of the mode in question. Using this framework, it can be shown that these errors may be approximated during model order reduction, in a computationally efficient manner. This may serve as a tool for predicting internal resonances between the reduced and condensed coordinates,

or, equivalently, for verifying the accuracy of ROMs by ensuring that that static condensation approximation is sufficiently accurate for all operating conditions of interest.

The rest of this chapter is structured as follows. In section 5.2, the nature of quasi-static and dynamic modal coupling in geometrically nonlinear systems is explored using a simple oscillator as a motivating example. Section 5.3 introduces a method for approximating the error associated with static condensation during model order reduction, which can be used to predict the existence of internal resonances. In sections 5.4 and 5.5, the proposed method is demonstrated using the simple oscillator, and an FE model of a clamped-clamped beam, respectively. Finally, conclusions are summarised in section 5.6.

5.2 Motivating example

In this section, the nature of modal coupling in general, conservative, geometrically nonlinear dynamical systems is explored. Specifically, the quasi-static coupling approximation, which is often used in reduced-order modelling frameworks, as well as its applicability in different scenarios, are investigated. To this end, a discrete 4-DOF system composed of two point masses, m, is considered as a motivating example. The masses are free to move in the x–y plane and are connected to a fixed frame and to each other through a set of linearly elastic springs, with stiffness $k_i \; \forall i \in \{1,2,3,4,5\}$ and unstretched length ℓ, as shown in figure 5.1. At the equilibrium position, all springs are undeformed and oriented either horizontally or vertically. This system may be considered an extension to the single-mass, 2-DOF oscillator previously studied in Touzé *et al.* (2004a); Touzé and Amabili (2006) and in Chapter 3.

The equations of motion of the oscillator can be found using the Euler-Lagrange equation, i.e.

$$\frac{\mathrm{d}}{\mathrm{d}t}\left(\frac{\partial \mathcal{L}}{\partial \dot{\mathbf{x}}}\right) - \frac{\partial \mathcal{L}}{\partial \mathbf{x}} = \mathbf{F}, \tag{5.1}$$

where all quantities have their usual meanings. The potential energy of spring i is given by

$$\mathcal{V}_i = \frac{1}{2} k_i (d_i - \ell)^2, \tag{5.2}$$

where d_i is its length in the deformed configuration. Then, the Lagrangian of the

system can be expressed as

$$\mathcal{L} = \mathcal{T}(\dot{\mathbf{x}}) - \mathcal{V}(\mathbf{x}) = \frac{1}{2} m \left(\dot{y}_1^2 + \dot{y}_2^2 + \dot{x}_1^2 + \dot{x}_2^2 \right) - \frac{1}{2} \sum_{i=1}^{5} k_i (d_i - \ell)^2 . \tag{5.3}$$

Substituting this into equation (5.1), allows the dynamics of the oscillator to be written in the form

$$\mathbf{M}\ddot{\mathbf{x}} + \mathbf{K}\mathbf{x} + \mathbf{f}(\mathbf{x}) = \mathbf{F}, \tag{5.4}$$

where

$$\mathbf{x} = \begin{pmatrix} y_1 \\ y_2 \\ x_1 \\ x_2 \end{pmatrix}, \quad \mathbf{M} = \begin{bmatrix} m & 0 & 0 & 0 \\ 0 & m & 0 & 0 \\ 0 & 0 & m & 0 \\ 0 & 0 & 0 & m \end{bmatrix}, \quad \mathbf{K} = \begin{bmatrix} k_4 & 0 & 0 & 0 \\ 0 & k_5 & 0 & 0 \\ 0 & 0 & k_1 + k_2 & -k_2 \\ 0 & 0 & -k_2 & k_2 + k_3 \end{bmatrix} \tag{5.5a}$$

$$\mathbf{f}(\mathbf{x}) = \begin{pmatrix} -\dfrac{k_4 \ell (\ell + y_1)}{d_4} - \dfrac{k_1 y_1 (\ell - d_1)}{d_1} - \dfrac{k_2 (y_1 - y_2)(\ell - d_2)}{d_2} + k_4 \ell \\ -\dfrac{k_5 \ell (\ell + y_2)}{d_5} - \dfrac{k_3 y_2 (\ell - d_3)}{d_3} - \dfrac{k_2 (y_2 - y_1)(\ell - d_2)}{d_2} + k_5 \ell \\ -\dfrac{k_4 x_1 (\ell - d_4)}{d_4} - \dfrac{k_1 \ell (\ell + x_1)}{d_1} - \dfrac{k_2 \ell (x_1 - x_2 - \ell)}{d_2} + (k_1 - k_2)\ell \\ -\dfrac{k_5 x_2 (\ell - d_5)}{d_5} - \dfrac{k_3 \ell (x_2 - \ell)}{d_3} - \dfrac{k_2 \ell (\ell + x_2 - x_1)}{d_2} + (k_2 - k_3)\ell \end{pmatrix} \tag{5.5b}$$

$$\begin{aligned} d_1 &= \sqrt{y_1^2 + (\ell + x_1)^2}, \quad d_2 = \sqrt{(y_1 - y_2)^2 + (\ell - x_1 + x_2)^2}, \quad d_3 = \sqrt{y_2^2 + (\ell - x_2)^2}, \\ d_4 &= \sqrt{(\ell + y_1)^2 + x_1^2}, \quad d_5 = \sqrt{(\ell + y_2)^2 + x_2^2}. \end{aligned} \tag{5.5c}$$

Using the transform $\mathbf{x} = \mathbf{\Phi}\mathbf{q}$, the equations of motion can be expressed in the modal space, where they are linearly uncoupled, in the form

$$\ddot{\mathbf{q}} + \mathbf{\Lambda}\mathbf{q} + \mathbf{f}_q(\mathbf{q}) = \mathbf{F}_q. \tag{5.6}$$

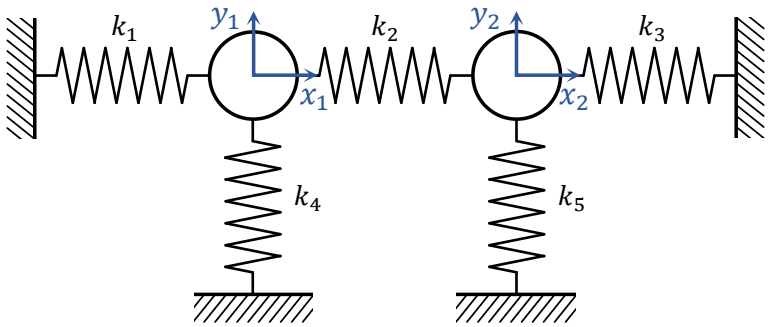

Figure 5.1. Schematic diagram of the 2-mass, 4-DOF oscillator used as a motivating example, shown at equilibrium with the springs unstretched.

For this motivating example, the physical parameters of the system are set to the following values: $m = 1\,\mathrm{kg}$, $\ell = 1\,\mathrm{m}$, $k_1 = 1000\,\mathrm{N\,m^{-1}}$, $k_2 = 10\,\mathrm{N\,m^{-1}}$, $k_3 = 1000\,\mathrm{N\,m^{-1}}$, $k_4 = 1\,\mathrm{N\,m^{-1}}$, $k_5 = 21.2\,\mathrm{N\,m^{-1}}$. Note that the horizontal grounding springs (k_1 and k_3) are significantly stiffer than the vertical grounding ones, which creates a dichotomy between the natural frequencies of the first two modes ($\omega_1 = 1.0\,\mathrm{rad\,s^{-1}}$, $\omega_2 = 4.6\,\mathrm{rad\,s^{-1}}$), and those of the other two modes ($\omega_3 = 31.6\,\mathrm{rad\,s^{-1}}$, $\omega_4 = 31.9\,\mathrm{rad\,s^{-1}}$). This system aims to emulate, in a highly simplified manner, the slow/fast dynamics that characterise the low-frequency transverse modes and high-frequency in-plane modes in plate- or beam-like structures.

Firstly, the quasi-static behaviour of the system when only the first mode is forced directly is considered. The static equations $\mathbf{\Lambda q} + \mathbf{f}_q(\mathbf{q}) = \mathbf{F}_q$ are numerically solved for $\mathbf{q}$, for a series of load cases where $F_1 \in [-3, +3]$ and $F_n = 0\,\forall n \in \{2,3,4\}$, where F_n denotes the n^{th} element in $\mathbf{F}_q$. Figures 5.2 (a) and (b) show the quasi-static modal response of the system against the static force applied to the first mode, and against the corresponding response of the first mode, respectively. As previously discussed, in reduced-order modelling methods such as the ICE(-IC) (Hollkamp and Gordon, 2008; Nicolaidou *et al.*, 2020a), this dataset, or more commonly a subset thereof, is used to approximate the functions describing the nonlinear stiffness of the reduced modes, as well as the quasi-static relationship between the condensed modes and the reduced modes. Specifically, the latter task is carried out only for a small set of high-frequency in-plane modes, for which the inertial forces are assumed to be

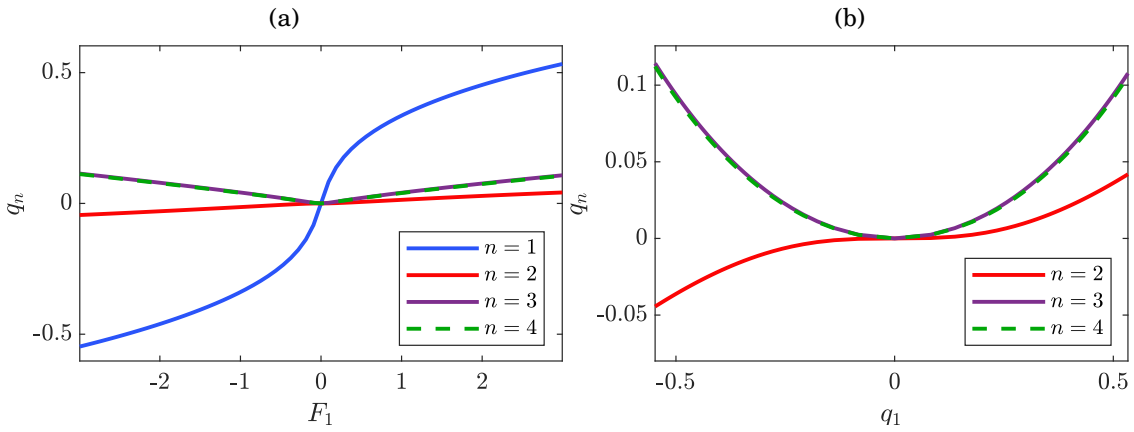

Figure 5.2. Quasi-static modal response of the 4-DOF oscillator, plotted against (a) the static force applied in the first mode and (b) the resulting response of the first mode.

small relative to the internal restoring forces. Here, this approach is generalised by treating all condensed modes equally, irrespective of their natural frequency or characteristics of their modeshapes. The quasi-static relationship between the n^{th} mode and the reduced mode is denoted using the function g_n, and approximate it as a K^{th}-order polynomial, i.e.

$$g_n(q_1) = \sum_{k=2}^{K} B_k^{(n)} q_1^k, \qquad \forall n \in \{2,3,4\}, \tag{5.7}$$

where the coefficients $B_k^{(n)}$ are identified via least-squares regression based on the static solution dataset, i.e. fitting to the curves shown in figure 5.2 (b).

Figure 5.3 (a) shows the first backbone curve of the 4-DOF oscillator, computed according to equations (5.4) and (5.5) (with $\mathbf{F} = \mathbf{0}$). The branch emerging near $\Omega = 1.55\,\text{rad}\,\text{s}^{-1}$ corresponds to a 1:3 internal resonance between the first and second modes. Figures 5.3 (b), (c) and (d) show the time history of the modal response of the system (solid black lines), for three different NNMs associated with the first backbone curve, which are represented by red dots in figure 5.3 (a) and correspond to fundamental response frequencies of $1.01\,\text{rad}\,\text{s}^{-1}$, $1.39\,\text{rad}\,\text{s}^{-1}$ and $1.53\,\text{rad}\,\text{s}^{-1}$, respectively. The quasi-static response of modes 2–4 is computed by evaluating the functions $g_n(q_1)$ during the NNM motion; this is represented by dash-dotted lines in figures 5.3 (b), (c) and (d). The difference between the dynamic and the quasi-static response of each mode, i.e. $q_n - g_n(q_1)$, is represented by dashed blue lines. This may be considered as the error arising from the quasi-static approximation/implicit condensation.

It can be seen that, as expected, the quasi-static approximation is sufficiently accurate when applied to the high-frequency modes, as $q_n \approx g_n(q_1)$, $\forall n \in \{3,4\}$, $\forall t$, $\forall \Omega$. However, in the case of the second, low-frequency mode, the quasi-static approximation is initially moderately accurate near the first linear natural frequency, but becomes increasingly inaccurate as the system approaches internal resonance. Interestingly, for all NNM solutions, the error arising from this approximation appears to be a single-harmonic signal of frequency 3Ω. This suggests that the response of each condensed mode may be naturally decomposed into two parts: a component that is *quasi-statically coupled* to the reduced mode(s), and a component that is *dynamically independent* of the reduced mode(s). In the next section, this idea is exploited in order to show how the existence of dynamic interactions can be predicted, and its relevance to reduced-order modelling is discussed.

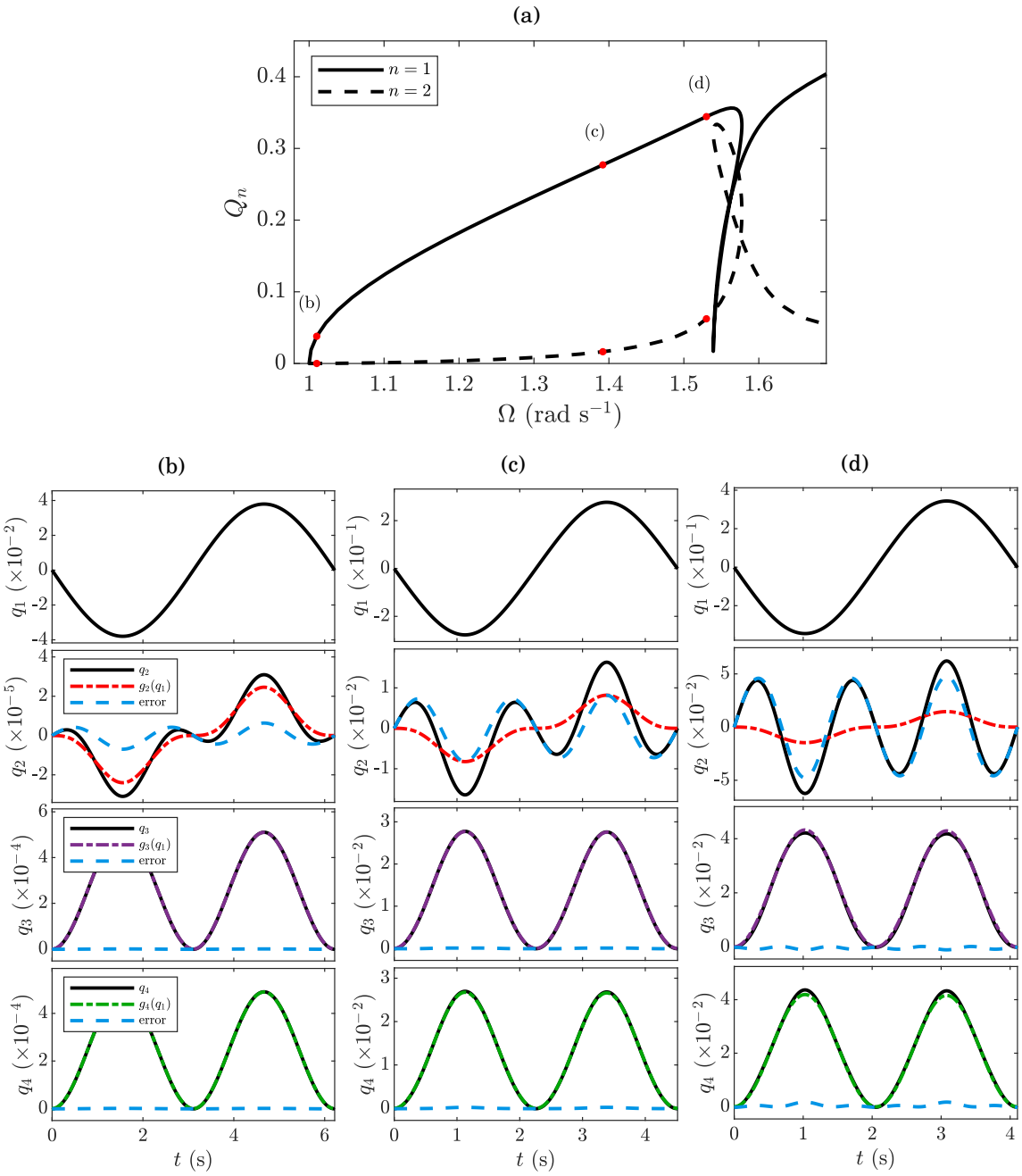

Figure 5.3. (a) First backbone curve of the 4-DOF oscillator, shown in the projections of the maximum amplitudes of the first two modes, Q_1 and Q_2, against the response frequency, Ω. Three nonlinear normal modes of the system, corresponding to fundamental response frequencies of (b) 1.01 rad s^{-1}, (c) 1.39 rad s^{-1} and (d) 1.53 rad s^{-1}, are also shown, and represented by red dots on the backbone curves. These are plotted as modal displacement, q_n, against time, t (solid black lines). The dash-dotted red, purple and green lines show the quasi-static component of modes 2, 3 and 4, respectively, and the dashed blue lines show the corresponding error, $q_n - g_n(q_1)$, $\forall n = \{2,3,4\}$.

5.3 Predicting dynamic interactions

5.3.1 Proposed method

We start by considering the equations of motion of the full-order FE model, with its linear normal modes separated into three distinct groups, as previously discussed in section 4.2.1. The first group of modes, denoted by the subscript $\bullet_r$ (reduced), consists of a small set of modes which, for a given set of operating conditions, contain the majority of the total energy in the system, and are dynamically independent — these modes must form the reduction basis. The number of modes in this class, $R \ll N$, dictates the lower limit to the number of DOFs that an accurate ROM must have. For a single backbone curve in the absence of any internal resonance, $R = 1$. The second group, denoted by the subscript $\bullet_s$ (statically coupled), is comprised of $S \ll N$ modes which may contain a substantial fraction of the energy of the full-order system, yet their response can be approximated as being quasi-statically coupled to the reduced modes. These modes need not be included as independent DOFs in the reduction basis, as their effects can be incorporated implicitly in the reduced dynamics, as discussed in previous chapters. Finally, the third group, denoted by the subscript $\bullet_u$ (unmodelled), contains the remaining $U = (N - R - S)$ modes which are very weakly coupled to the reduced modes, such that they always contain a negligible amount of energy under the operating conditions of interest. As such, it is assumed that these modes can be ignored during the reduction process with negligible loss of accuracy. Using this framework, the modal equations of motion of the FE model can be rewritten as

$$\begin{bmatrix} \ddot{\mathbf{q}}_r \\ \ddot{\mathbf{q}}_s \\ \ddot{\mathbf{q}}_u \end{bmatrix} + \begin{bmatrix} \boldsymbol{\Lambda}_r & \mathbf{0} & \mathbf{0} \\ \mathbf{0} & \boldsymbol{\Lambda}_s & \mathbf{0} \\ \mathbf{0} & \mathbf{0} & \boldsymbol{\Lambda}_u \end{bmatrix} \begin{bmatrix} \mathbf{q}_r \\ \mathbf{q}_s \\ \mathbf{q}_u \end{bmatrix} + \begin{bmatrix} \tilde{\mathbf{f}}_r(\mathbf{q}_r, \mathbf{q}_s, \mathbf{q}_u) \\ \tilde{\mathbf{f}}_s(\mathbf{q}_r, \mathbf{q}_s, \mathbf{q}_u) \\ \tilde{\mathbf{f}}_u(\mathbf{q}_r, \mathbf{q}_s, \mathbf{q}_u) \end{bmatrix} = \begin{bmatrix} \mathbf{F}_r \\ \mathbf{0} \\ \mathbf{0} \end{bmatrix}, \tag{5.8}$$

which was previously given in equation (4.3). Ignoring the third group of weakly-coupled modes, these can be approximated as

$$\begin{bmatrix} \ddot{\mathbf{r}} \\ \ddot{\mathbf{s}} \end{bmatrix} + \begin{bmatrix} \boldsymbol{\Lambda}_r & \mathbf{0} \\ \mathbf{0} & \boldsymbol{\Lambda}_s \end{bmatrix} \begin{bmatrix} \mathbf{r} \\ \mathbf{s} \end{bmatrix} + \begin{bmatrix} \hat{\mathbf{f}}_r(\mathbf{r}, \mathbf{s}) \\ \hat{\mathbf{f}}_s(\mathbf{r}, \mathbf{s}) \end{bmatrix} = \begin{bmatrix} \mathbf{F}_r \\ \mathbf{0} \end{bmatrix}, \tag{5.9}$$

where $\hat{\mathbf{f}}_r(\mathbf{r}, \mathbf{s}) := \tilde{\mathbf{f}}_r(\mathbf{r}, \mathbf{s}, \mathbf{0})$ and $\hat{\mathbf{f}}_s(\mathbf{r}, \mathbf{s}) := \tilde{\mathbf{f}}_s(\mathbf{r}, \mathbf{s}, \mathbf{0})$, such that $\mathbf{q}_r \approx \mathbf{r}$, $\mathbf{q}_s \approx \mathbf{s}$, $\mathbf{q}_u \approx \mathbf{u} = \mathbf{0}$, and $\mathbf{x} \approx \boldsymbol{\Phi}_r \mathbf{r} + \boldsymbol{\Phi}_s \mathbf{s}$. Equivalently, the kinetic energy of the full-order system can be approximated as

$$\hat{\mathcal{T}}(\mathbf{r}, \mathbf{s}) = \frac{1}{2} (\dot{\mathbf{r}})^{\mathsf{T}} \dot{\mathbf{r}} + \frac{1}{2} (\dot{\mathbf{s}})^{\mathsf{T}} \dot{\mathbf{s}}, \tag{5.10}$$

whilst the potential energy function is such that

$$\frac{\partial \hat{\mathcal{V}}}{\partial \mathbf{r}} = \mathbf{\Lambda}_r \mathbf{r} + \hat{\mathbf{f}}_r(\mathbf{r}, \mathbf{s}), \tag{5.11a}$$

$$\frac{\partial \hat{\mathcal{V}}}{\partial \mathbf{s}} = \mathbf{\Lambda}_s \mathbf{s} + \hat{\mathbf{f}}_s(\mathbf{r}, \mathbf{s}). \tag{5.11b}$$

As discussed in Chapter 4, when the modes in the second group, $\mathbf{s}$, can be expressed as functions of the reduced modes, $\mathbf{r}$, i.e. $\mathbf{s} = \mathbf{g}(\mathbf{r})$, then equation (5.9) can be *exactly* reduced to

$$\ddot{\mathbf{r}} + \left(\frac{\partial \mathbf{g}}{\partial \mathbf{r}}\right)^{\mathsf{T}} \frac{\partial \mathbf{g}}{\partial \mathbf{r}} \ddot{\mathbf{r}} + \left(\frac{\partial \mathbf{g}}{\partial \mathbf{r}}\right)^{\mathsf{T}} \frac{\partial^2 \mathbf{g}}{\partial \mathbf{r}^2} \dot{\mathbf{r}}\dot{\mathbf{r}} + \mathbf{\Lambda}_r \mathbf{r} + \mathbf{f}_r(\mathbf{r}) = \mathbf{F}_r. \tag{5.12}$$

Reduced-order models based on equation (5.12) were found to produce remarkably accurate results for systems where a clear slow/fast dynamic behaviour can be observed, e.g. between the low-frequency transverse modes and the highly stiff in-plane modes in thin plates and slender beams.

In this chapter, we aim to broaden the scope of the implicit condensation approach, and seek to quantify the error introduced by the static condensation. This error is denoted by the $S \times 1$ time-dependent vector $\mathbf{h}(t)$, i.e.

$$\mathbf{s} = \mathbf{g}(\mathbf{r}) + \mathbf{h}. \tag{5.13}$$

Using equation (5.13), and noting that $\dot{\mathbf{s}} = \dfrac{\partial \mathbf{g}}{\partial \mathbf{r}} \dot{\mathbf{r}} + \dot{\mathbf{h}}$, the Lagrangian of the system can be expressed as

$$\begin{aligned} \hat{\mathcal{L}}(\mathbf{r}, \mathbf{h}) &= \hat{\mathcal{T}}(\mathbf{r}, \mathbf{g} + \mathbf{h}) - \hat{\mathcal{V}}(\mathbf{r}, \mathbf{g} + \mathbf{h}) \\ &= \frac{1}{2} (\dot{\mathbf{r}})^{\mathsf{T}} \dot{\mathbf{r}} + \frac{1}{2} (\dot{\mathbf{r}})^{\mathsf{T}} \left(\frac{\partial \mathbf{g}}{\partial \mathbf{r}}\right)^{\mathsf{T}} \frac{\partial \mathbf{g}}{\partial \mathbf{r}} \dot{\mathbf{r}} + (\dot{\mathbf{r}})^{\mathsf{T}} \left(\frac{\partial \mathbf{g}}{\partial \mathbf{r}}\right)^{\mathsf{T}} \dot{\mathbf{h}} + \frac{1}{2} \left(\dot{\mathbf{h}}\right)^{\mathsf{T}} \dot{\mathbf{h}} - \hat{\mathcal{V}}(\mathbf{r}, \mathbf{g} + \mathbf{h}). \end{aligned} \tag{5.14}$$

The partial derivatives of the Lagrangian with respect to $\dot{\mathbf{r}}$, $\dot{\mathbf{h}}$, $\mathbf{r}$ and $\mathbf{h}$ can be written, respectively, as

$$\frac{\partial \hat{\mathcal{L}}}{\partial \dot{\mathbf{r}}} = \dot{\mathbf{r}} + \left(\frac{\partial \mathbf{g}}{\partial \mathbf{r}}\right)^{\mathsf{T}} \frac{\partial \mathbf{g}}{\partial \mathbf{r}} \dot{\mathbf{r}} + \left(\frac{\partial \mathbf{g}}{\partial \mathbf{r}}\right)^{\mathsf{T}} \dot{\mathbf{h}}, \tag{5.15a}$$

$$\frac{\partial \hat{\mathcal{L}}}{\partial \dot{\mathbf{h}}} = \frac{\partial \mathbf{g}}{\partial \mathbf{r}} \dot{\mathbf{r}} + \dot{\mathbf{h}}, \tag{5.15b}$$

$$\begin{aligned} \frac{\partial \hat{\mathcal{L}}}{\partial \mathbf{r}} = &\left(\frac{\partial \mathbf{g}}{\partial \mathbf{r}}\right)^{\mathsf{T}} \left(\frac{\partial^2 \mathbf{g}}{\partial \mathbf{r}^2} \dot{\mathbf{r}}\right) \dot{\mathbf{r}} + \left(\frac{\partial^2 \mathbf{g}}{\partial \mathbf{r}^2} \dot{\mathbf{r}}\right)^{\mathsf{T}} \dot{\mathbf{h}} - \left(\mathbf{\Lambda}_r \mathbf{r} + \hat{\mathbf{f}}_r(\mathbf{r}, \mathbf{g} + \mathbf{h})\right) \\ &- \left(\frac{\partial \mathbf{g}}{\partial \mathbf{r}}\right)^{\mathsf{T}} \left(\mathbf{\Lambda}_s(\mathbf{g} + \mathbf{h}) + \hat{\mathbf{f}}_s(\mathbf{r}, \mathbf{g} + \mathbf{h})\right), \end{aligned} \tag{5.15c}$$

$$\frac{\partial \hat{\mathcal{L}}}{\partial \mathbf{h}} = -\left(\mathbf{\Lambda}_s(\mathbf{g} + \mathbf{h}) + \hat{\mathbf{f}}_s(\mathbf{r}, \mathbf{g} + \mathbf{h})\right). \tag{5.15d}$$

Differentiating equations (5.15a) and (5.15b) with respect to time gives

$$\frac{\mathrm{d}}{\mathrm{d}t}\left(\frac{\partial \hat{\mathcal{L}}}{\partial \dot{\mathbf{r}}}\right) = \ddot{\mathbf{r}} + \left(\frac{\partial \mathbf{g}}{\partial \mathbf{r}}\right)^{\mathsf{T}} \frac{\partial \mathbf{g}}{\partial \mathbf{r}}\ddot{\mathbf{r}} + 2\left(\frac{\partial \mathbf{g}}{\partial \mathbf{r}}\right)^{\mathsf{T}} \frac{\partial^2 \mathbf{g}}{\partial \mathbf{r}^2}\dot{\mathbf{r}}\dot{\mathbf{r}} + \left(\frac{\partial^2 \mathbf{g}}{\partial \mathbf{r}^2}\dot{\mathbf{r}}\right)^{\mathsf{T}} \dot{\mathbf{h}} + \left(\frac{\partial \mathbf{g}}{\partial \mathbf{r}}\right)^{\mathsf{T}} \ddot{\mathbf{h}}, \tag{5.16a}$$

$$\frac{\mathrm{d}}{\mathrm{d}t}\left(\frac{\partial \hat{\mathcal{L}}}{\partial \dot{\mathbf{h}}}\right) = \frac{\partial \mathbf{g}}{\partial \mathbf{r}}\ddot{\mathbf{r}} + \left(\frac{\partial^2 \mathbf{g}}{\partial \mathbf{r}^2}\dot{\mathbf{r}}\right)\dot{\mathbf{r}} + \ddot{\mathbf{h}}. \tag{5.16b}$$

The equations of motion for $\mathbf{r}$ and $\mathbf{h}$ can be derived using the Euler-Lagrange equation, i.e.

$$\frac{\mathrm{d}}{\mathrm{d}t}\left(\frac{\partial \mathcal{L}}{\partial \dot{\mathbf{r}}}\right) - \frac{\partial \mathcal{L}}{\partial \mathbf{r}} = \mathbf{F}_r, \tag{5.17a}$$

$$\frac{\mathrm{d}}{\mathrm{d}t}\left(\frac{\partial \mathcal{L}}{\partial \dot{\mathbf{h}}}\right) - \frac{\partial \mathcal{L}}{\partial \mathbf{h}} = \mathbf{0}. \tag{5.17b}$$

Substituting equations (5.15) and (5.16) into equations (5.17) leads to

$$\begin{aligned} &\ddot{\mathbf{r}} + \left(\frac{\partial \mathbf{g}}{\partial \mathbf{r}}\right)^{\mathsf{T}} \frac{\partial \mathbf{g}}{\partial \mathbf{r}}\ddot{\mathbf{r}} + \left(\frac{\partial \mathbf{g}}{\partial \mathbf{r}}\right)^{\mathsf{T}} \ddot{\mathbf{h}} + \left(\frac{\partial \mathbf{g}}{\partial \mathbf{r}}\right)^{\mathsf{T}} \left(\frac{\partial^2 \mathbf{g}}{\partial \mathbf{r}^2}\dot{\mathbf{r}}\right)\dot{\mathbf{r}} \\ &\qquad + \mathbf{\Lambda}_r \mathbf{r} + \hat{\mathbf{f}}_r(\mathbf{r}, \mathbf{g}+\mathbf{h}) + \left(\frac{\partial \mathbf{g}}{\partial \mathbf{r}}\right)^{\mathsf{T}} \left(\mathbf{\Lambda}_s(\mathbf{g}+\mathbf{h}) + \hat{\mathbf{f}}_s(\mathbf{r}, \mathbf{g}+\mathbf{h})\right) = \mathbf{F}_r \end{aligned} \tag{5.18a}$$

$$\ddot{\mathbf{h}} + \frac{\partial \mathbf{g}}{\partial \mathbf{r}}\ddot{\mathbf{r}} + \left(\frac{\partial^2 \mathbf{g}}{\partial \mathbf{r}^2}\dot{\mathbf{r}}\right)\dot{\mathbf{r}} + \left(\mathbf{\Lambda}_s(\mathbf{g}+\mathbf{h}) + \hat{\mathbf{f}}_s(\mathbf{r}, \mathbf{g}+\mathbf{h})\right) = \mathbf{0}. \tag{5.18b}$$

Using a Taylor series expansion about $\mathbf{s} = \mathbf{g}$, the stiffness expressions in equations (5.18) can be approximated as

$$\mathbf{\Lambda}_r \mathbf{r} + \hat{\mathbf{f}}_r(\mathbf{r}, \mathbf{g}+\mathbf{h}) = \mathbf{\Lambda}_r \mathbf{r} + \hat{\mathbf{f}}_r(\mathbf{r}, \mathbf{g}) + \mathbf{B}(\mathbf{r})\mathbf{h} + \mathcal{O}(\mathbf{h}^2) \tag{5.19a}$$

$$\begin{aligned} \mathbf{\Lambda}_s(\mathbf{g}+\mathbf{h}) + \hat{\mathbf{f}}_s(\mathbf{r}, \mathbf{g}+\mathbf{h}) &= \mathbf{\Lambda}_s \mathbf{g} + \hat{\mathbf{f}}_s(\mathbf{r}, \mathbf{g}) + \mathbf{C}(\mathbf{r})\mathbf{h} + \mathcal{O}(\mathbf{h}^2) \\ &= \mathbf{C}(\mathbf{r})\mathbf{h} + \mathcal{O}(\mathbf{h}^2), \end{aligned} \tag{5.19b}$$

where

$$\mathbf{B}(\mathbf{r}) = \left.\frac{\partial \hat{\mathbf{f}}_r(\mathbf{r}, \mathbf{s})}{\partial \mathbf{s}}\right|_{\mathbf{s}=\mathbf{g}} \tag{5.20a}$$

$$\mathbf{C}(\mathbf{r}) = \mathbf{\Lambda}_s + \left.\frac{\partial \hat{\mathbf{f}}_s(\mathbf{r}, \mathbf{s})}{\partial \mathbf{s}}\right|_{\mathbf{s}=\mathbf{g}}. \tag{5.20b}$$

Note that, by definition, $\mathbf{\Lambda}_s \mathbf{g} + \hat{\mathbf{f}}_s(\mathbf{r}, \mathbf{g}) = \mathbf{0}$, as $\mathbf{g}(\mathbf{r})$ is computed based on the *static* response of the system, with a static force only applied to the reduced modes (i.e. $\mathbf{F}_s = \mathbf{0}$). Substituting equations (5.19) into equations (5.18), and noting that $\mathbf{B} + \left(\frac{\partial \mathbf{g}}{\partial \mathbf{r}}\right)^{\mathsf{T}} \mathbf{C} = \mathbf{0}$ as shown in section 5.3.3, leads to

$$\ddot{\mathbf{r}} + \left(\frac{\partial \mathbf{g}}{\partial \mathbf{r}}\right)^{\mathsf{T}} \frac{\partial \mathbf{g}}{\partial \mathbf{r}}\ddot{\mathbf{r}} + \left(\frac{\partial \mathbf{g}}{\partial \mathbf{r}}\right)^{\mathsf{T}} \frac{\partial^2 \mathbf{g}}{\partial \mathbf{r}^2}\dot{\mathbf{r}}\dot{\mathbf{r}} + \mathbf{\Lambda}_r \mathbf{r} + \mathbf{f}_r(\mathbf{r}) = \mathbf{F}_r - \left(\frac{\partial \mathbf{g}}{\partial \mathbf{r}}\right)^{\mathsf{T}} \ddot{\mathbf{h}} + \mathcal{O}(\mathbf{h}^2) \tag{5.21a}$$

$$\ddot{\mathbf{h}} + \mathbf{C}(\mathbf{r})\mathbf{h} + \mathcal{O}(\mathbf{h}^2) = \mathbf{p}(\mathbf{r}, \dot{\mathbf{r}}, \ddot{\mathbf{r}}), \tag{5.21b}$$

where

$$\mathbf{p}(\mathbf{r},\dot{\mathbf{r}},\ddot{\mathbf{r}}) = -\frac{\partial \mathbf{g}}{\partial \mathbf{r}}\ddot{\mathbf{r}} - \frac{\partial^2 \mathbf{g}}{\partial \mathbf{r}^2}\dot{\mathbf{r}}\dot{\mathbf{r}}. \tag{5.22}$$

It can be seen that, as expected, when $\mathbf{h} = \mathbf{0}$, equation (5.21a) is equivalent to the reduced dynamics obtained for the perfectly statically coupled case (equation (5.12)) — this is referred to as the ICE-IC ROM. The additional $\mathbf{h}$- and $\ddot{\mathbf{h}}$-dependent terms that appear on the right-hand side of equation (5.21a) may be considered as a forcing arising due to the *dynamic* coupling between $\mathbf{r}$ and $\mathbf{s}$. In addition, when the kinetic energy of the statically coupled modes is negligible (i.e. $\dot{\mathbf{s}}^\intercal\dot{\mathbf{s}} \approx 0$), the $\mathbf{g}$-dependent terms in equation (5.12) are negligible, and the reduced dynamics can be simply expressed as

$$\ddot{\mathbf{r}} + \boldsymbol{\Lambda}_r\mathbf{r} + \mathbf{f}_r(\mathbf{r}) = \mathbf{F}_r, \tag{5.23}$$

As discussed in Chapter 4, this more traditional form of the reduced equations of motion is suitable for structures in which in-plane displacements are limited, such that the effect of inertial compensation is negligible.

The remainder of this chapter demonstrates how the equations of motion for $\mathbf{h}$ (equation (5.21b)) may be used to efficiently predict the presence of dynamic coupling between the reduced modes ($\mathbf{r}$) and the condensed modes ($\mathbf{s}$). This allows features such as internal resonances to be predicted, and ROMs to be validated without the need for full-order FE simulations.

5.3.2 Use in reduced-order modelling frameworks

The linear properties of the ROM, $\boldsymbol{\Lambda}_r$, $\boldsymbol{\Phi}_r$ and $\boldsymbol{\Phi}_s$, can be computed directly using the linear mass and stiffness matrices of the FE model. The reduced nonlinear stiffness functions, $\mathbf{f}_r(\mathbf{r})$, and the quasi-static coupling functions, $\mathbf{g}(\mathbf{r})$, are approximated indirectly in a least-squares manner using a force-displacement dataset for a series of nonlinear static solutions extracted from the FE model; these are approximated as K^{th}-order polynomials of the reduced coordinates. Once the ROM parameters are identified, the reduced backbone curves can be computed, e.g. using numerical continuation, based on either equation (5.23) (ICE) or equation (5.12) (ICE-IC).

Using equation (5.21b), additional insight can now be gained by simulating the error dynamics for each NNM of the ROM. Given that the static modal coupling is well-captured through the functions $\mathbf{g}(\mathbf{r})$, then, in the absence or near the onset of a dynamic interaction, the error $\mathbf{h}$ is expected to be relatively small such that any

nonlinear monomials of $\mathbf{h}$ become negligible, i.e. $\mathcal{O}(\mathbf{h}^2) \approx \mathbf{0}$. As such, the linearised version of equation (5.21b) may be considered, which can be solved efficiently using, for example, the harmonic balance method (Nayfeh and Mook, 1995). To this end, each element in the $S \times S$ matrix $\mathbf{C}$ containing the linear coefficients of $\mathbf{h}$, must be approximated as a function of $\mathbf{r}$. As with $\mathbf{f}_r(\mathbf{r})$ and $\mathbf{g}(\mathbf{r})$, these can be computed based on least-squares polynomial regression. In this case, the tangent stiffness matrix, $\mathbf{K}_{\text{tan}}$, must be extracted for each nonlinear static load case, in addition to the vectors of applied forces and resulting displacement, which are needed for the standard ICE(-IC) method. The coefficients of each function in $\mathbf{C}(\mathbf{r})$ are then computed using the $\{\boldsymbol{\Phi}_s^{\intercal}\mathbf{K}_{\text{tan}}\boldsymbol{\Phi}_s, \mathbf{r}_{\text{st}}\}$ dataset evaluated at each load case. The practical implications of this are considered later in section 5.5, where the proposed technique is demonstrated using an FE model built using commercial software.

Once these functions are approximated, then the matrix $\mathbf{C}$, as well as the vector on the right-hand side of equation (5.21b), $\mathbf{p}$, can be evaluated during a periodic solution of the ROM. These can then be expressed as summations of sinusoidal components, i.e.

$$C_{ij} = a_0^{(ij)} + \sum_{n=1}^{N_h} \left[a_n^{(ij)} \cos(n\omega t) + b_n^{(ij)} \sin(n\omega t) \right], \tag{5.24a}$$

$$p_i = a_0^{(i)} + \sum_{n=1}^{N_h} \left[a_n^{(i)} \cos(n\omega t) + \beta_n^{(i)} \sin(n\omega t) \right], \tag{5.24b}$$

where N_h is the number of harmonics, and $a_n^{(ij)}$, $a_n^{(i)}$ $\forall n \in [0, N_h] \cap \mathbb{Z}$, and $b_n^{(ij)}$, $\beta_n^{(i)}$ $\forall n \in [1, N_h] \cap \mathbb{Z}$, are coefficients which can be identified via a discrete Fourier transform for each element in $\mathbf{C}$ and $\mathbf{p}$, during an NNM motion with fundamental response frequency ω. Similarly, each element in $\mathbf{h}$ can be expressed as a sum of its Fourier components, i.e.

$$h_i = A_0^{(i)} + \sum_{n=1}^{N_h} \left[A_n^{(i)} \cos(n\omega t) + B_n^{(i)} \sin(n\omega t) \right], \tag{5.25a}$$

$$\ddot{h}_i = -\sum_{n=1}^{N_h} (n\omega)^2 \left[A_n^{(i)} \cos(n\omega t) + B_n^{(i)} \sin(n\omega t) \right]. \tag{5.25b}$$

Using equations (5.24) and (5.25), the terms in equation (5.21b) can be expanded, the coefficients of like harmonic terms on either side of the equation equated, and the harmonic amplitudes of $\mathbf{h}$ computed by solving the resulting set of simultaneous linear equations. This can be expressed as

$$\mathbf{c}_h = \boldsymbol{\Upsilon}^{-1}\mathbf{c}_{\mathbf{p}}, \tag{5.26}$$

where $\mathbf{c}_h$ and $\mathbf{c}_\mathbf{p}$ are vectors containing the harmonic coefficients of $\mathbf{h}$ and $\mathbf{p}$, respectively, and Υ is a matrix which can be algorithmically populated with the harmonic coefficients of $\mathbf{C}$ — further details are given in section 5.3.4. Finally, the computed amplitudes in $\mathbf{c}_h$ are used to estimate the time history of the error corresponding to each condensed mode during a periodic motion of the ROM (equation (5.25a)).

As discussed in section 5.1, the main limitation of the ICE(-IC) method remains the fact that it relies on a slow/fast decomposition between the reduced and condensed modes. With the method proposed here this limitation is overcome, as the condensed basis can now be formed using any modes, irrespective of their natural frequency. This method can be used to monitor the error associated with the static condensation, and thus identify if/when a condensed mode becomes resonant. This would suggest the quasi-static coupling assumption is no longer appropriate for the mode in question, and instead the mode must be included as an independent DOF in the reduction basis ($\mathbf{\Phi}_r$). Equivalently, this method can be used as a tool for validating ROMs, by ensuring that the component of the condensed modes that is dynamically independent of the reduced modes (i.e. $\mathbf{h}$) remains sufficiently small for all operating conditions of interest.

5.3.3 Relationship between B and C

Starting from equation (5.9), it can be seen that the quasi-static coupling functions, $\mathbf{g}(\mathbf{r})$, are defined such that the following equation is satisfied:

$$\left(\mathbf{\Lambda}_s\mathbf{s}+\hat{\mathbf{f}}_s(\mathbf{r},\mathbf{s})\right)\Big|_{\mathbf{s}=\mathbf{g}}=\mathbf{0}. \tag{5.27}$$

Taking the partial derivative of equation (5.27) with respect to $\mathbf{r}$, leads to

$$\frac{\partial\hat{\mathbf{f}}_s(\mathbf{r},\mathbf{s})}{\partial\mathbf{r}}\bigg|_{\mathbf{s}=\mathbf{g}}+\left(\mathbf{\Lambda}_s+\frac{\partial\hat{\mathbf{f}}_s(\mathbf{r},\mathbf{s})}{\partial\mathbf{s}}\right)\bigg|_{\mathbf{s}=\mathbf{g}}\frac{\partial\mathbf{g}}{\partial\mathbf{r}}=\mathbf{0}. \tag{5.28}$$

Substituting equation (5.11b), i.e. $\hat{\mathbf{f}}_s(\mathbf{r},\mathbf{s})=\dfrac{\partial\hat{\mathcal{V}}}{\partial\mathbf{s}}-\mathbf{\Lambda}_s\mathbf{s}$, and equation (5.20b), i.e. $\mathbf{C}(\mathbf{r})=\mathbf{\Lambda}_s+\left.\dfrac{\partial\hat{\mathbf{f}}_s}{\partial\mathbf{s}}\right|_{\mathbf{s}=\mathbf{g}}$, into equation (5.28) leads to

$$\begin{aligned}\left.\frac{\partial^2\mathcal{V}}{\partial\mathbf{r}\partial\mathbf{s}}\right|_{\mathbf{s}=\mathbf{g}}+\mathbf{C}\frac{\partial\mathbf{g}}{\partial\mathbf{r}}&=\mathbf{0},\\ \left(\frac{\partial^2\mathcal{V}}{\partial\mathbf{s}\partial\mathbf{r}}\right)^{\mathsf{T}}\bigg|_{\mathbf{s}=\mathbf{g}}+\mathbf{C}\frac{\partial\mathbf{g}}{\partial\mathbf{r}}&=\mathbf{0}.\end{aligned} \tag{5.29}$$

Finally, substituting equation (5.11a), i.e. $\left(\frac{\partial \mathcal{V}}{\partial \mathbf{r}}\right) = \mathbf{\Lambda}_r \mathbf{r} + \hat{\mathbf{f}}_r(\mathbf{r},\mathbf{s})$, and equation (5.20a), i.e. $\mathbf{B}(\mathbf{r}) = \left.\frac{\partial \hat{\mathbf{f}}_r}{\partial \mathbf{s}}\right|_{\mathbf{s}=\mathbf{g}}$, into equation (5.29), gives

$$\begin{aligned} \left(\frac{\partial \hat{\mathbf{f}}_r(\mathbf{r},\mathbf{s})}{\partial \mathbf{s}}\right)^{\mathsf{T}}\Bigg|_{\mathbf{s}=\mathbf{g}} + \mathbf{C}\frac{\partial \mathbf{g}}{\partial \mathbf{r}} &= \mathbf{0} \\ \mathbf{B}^{\mathsf{T}} + \mathbf{C}\frac{\partial \mathbf{g}}{\partial \mathbf{r}} &= \mathbf{0}, \end{aligned} \tag{5.30}$$

This is equivalent to $\mathbf{B} + \left(\frac{\partial \mathbf{g}}{\partial \mathbf{r}}\right)^{\mathsf{T}} \mathbf{C} = \mathbf{0}$, since $\mathbf{C} = \mathbf{C}^{\mathsf{T}}$.

5.3.4 Estimation of the harmonic coefficients of h

Using equations (5.24a) and (5.25), and neglecting harmonics higher than $N_h\omega$, the left-hand side of equation (5.21b) can be expressed as

$$\begin{aligned} \ddot{h}_i + \sum_{j=1}^{S} C_{ij} h_j = \sum_{j=1}^{S} c_0^{(ij)} &+ \sum_{k=1}^{N_h} \cos(k\omega t)\left[-(k\omega)^2 A_k^{(i)} + \sum_{j=1}^{S} c_k^{(ij)}\right] \\ &+ \sum_{k=1}^{N_h} \sin(k\omega t)\left[-(k\omega)^2 B_k^{(i)} + \sum_{j=1}^{S} d_k^{(ij)}\right], \end{aligned} \tag{5.31}$$

where

$$c_0^{(ij)} = a_0^{(ij)} A_0^{(j)} + \frac{1}{2}\sum_{n=1}^{N_h}\left(a_n^{(ij)} A_n^{(j)} + a_n^{(ij)} B_n^{(j)}\right), \tag{5.32a}$$

$$\begin{aligned} c_k^{(ij)} = a_0^{(ij)} A_k^{(j)} + a_k^{(ij)} A_0^{(j)} &+ \frac{1}{2}\sum_{n=1}^{k-1}\left(a_{k-n}^{(ij)} A_n^{(j)} - b_{k-n}^{(ij)} B_n^{(j)}\right) \\ &+ \frac{1}{2}\sum_{n=1}^{N_h-k}\left(a_{n+k}^{(ij)} A_n^{(j)} + b_{n+k}^{(ij)} B_n^{(j)}\right) \\ &+ \frac{1}{2}\sum_{n=k+1}^{N_h}\left(a_{n-k}^{(ij)} A_n^{(j)} + b_{n-k}^{(ij)} B_n^{(j)}\right), \qquad \forall k \in [1, N_h] \cap \mathbb{Z} \end{aligned} \tag{5.32b}$$

$$\begin{aligned} d_k^{(ij)} = a_0^{(ij)} B_k^{(j)} + b_k^{(ij)} A_0^{(j)} &+ \frac{1}{2}\sum_{n=1}^{k-1}\left(a_{k-n}^{(ij)} B_n^{(j)} + b_{k-n}^{(ij)} A_n^{(j)}\right) \\ &+ \frac{1}{2}\sum_{n=1}^{N_h-k}\left(-a_{n+k}^{(ij)} B_n^{(j)} + b_{n+k}^{(ij)} A_n^{(j)}\right) \\ &+ \frac{1}{2}\sum_{n=k+1}^{N_h}\left(a_{n-k}^{(ij)} B_n^{(j)} - b_{n-k}^{(ij)} A_n^{(j)}\right), \qquad \forall k \in [1, N_h] \cap \mathbb{Z}. \end{aligned} \tag{5.32c}$$

Using equations (5.31) and (5.24b), the expressions on either side of equation (5.21b) can be directly compared. The coefficients of like harmonic terms are equated and expressed in the form

$$\boldsymbol{\Upsilon}\mathbf{c}_h = \mathbf{c}_p, \tag{5.33}$$

where the $S(2N_h+1)\times 1$ vectors $\mathbf{c}_h$ and $\mathbf{c}_p$ contain the harmonic amplitudes of $\mathbf{h}$ and $\mathbf{p}$ respectively, i.e.

$$\mathbf{c}_h^{(i)} = \begin{bmatrix} A_0^{(i)} & A_1^{(i)} & B_1^{(i)} & A_2^{(i)} & B_2^{(i)} & \dots & A_{N_h}^{(i)} & B_{N_h}^{(i)} \end{bmatrix}, \tag{5.34a}$$

$$\mathbf{c}_h = \begin{bmatrix} \mathbf{c}_h^{(1)} & \mathbf{c}_h^{(2)} & \dots & \mathbf{c}_h^{(S)} \end{bmatrix}^\mathsf{T}, \tag{5.34b}$$

$$\mathbf{c}_p^{(i)} = \begin{bmatrix} \alpha_0^{(i)} & \alpha_1^{(i)} & \beta_1^{(i)} & \alpha_2^{(i)} & \beta_2^{(i)} & \dots & \alpha_{N_h}^{(i)} & \beta_{N_h}^{(i)} \end{bmatrix}, \tag{5.34c}$$

$$\mathbf{c}_p = \begin{bmatrix} \mathbf{c}_p^{(1)} & \mathbf{c}_p^{(2)} & \dots & \mathbf{c}_p^{(S)} \end{bmatrix}^\mathsf{T}. \tag{5.34d}$$

The $S(2N_h+1)\times S(2N_h+1)$ matrix $\boldsymbol{\Upsilon}\left(a_n^{(ij)}, b_n^{(ij)}\right)$ is populated according to equation (5.32). Finally, the harmonic coefficients of $\mathbf{h}$ are computed by inverting equation (5.33), i.e. $\mathbf{c}_h = \boldsymbol{\Upsilon}^{-1}\mathbf{c}_\mathbf{p}$.

5.4 Application to the 4-DOF oscillator

5.4.1 Single-mode ROM results

We now revisit the 4-DOF oscillator considered in section 5.2, in order to demonstrate the proposed method. Firstly, a seventh-order ($K=7$)[1], single-DOF ROM of the first mode is computed using the ICE-IC method (equation (5.12)), while the remaining three modes are included in the statically condensed basis, i.e. $\boldsymbol{\Phi}_r = \begin{bmatrix}\boldsymbol{\phi}_1\end{bmatrix}$, $\boldsymbol{\Phi}_s = \begin{bmatrix}\boldsymbol{\phi}_2 & \boldsymbol{\phi}_3 & \boldsymbol{\phi}_4\end{bmatrix}$, and $\boldsymbol{\Phi}_u$ is unpopulated as no modes are unmodelled. The dataset used to calibrate the ROM consists of a series of static solutions where the the static force applied to the first mode is equally spaced between -3 and $+3$. An example of the fitting procedure for the reduced nonlinear stiffness function, $\mathbf{f}_r(\mathbf{r})$, and the quasi-static coupling functions, $\mathbf{g}(\mathbf{r})$, is shown in figures 5.4 (a) and (b), respectively.

Figure 5.5 shows the backbone curve of the computed single-DOF ROM, in the projection of modal amplitudes against fundamental response frequency (blue lines).

[1] As discussed earlier in this thesis, this truncation order was adopted, as the resulting ROM was found to be robust with respect to scaling of the static forces used to calibrate it. This suggests that, for the response range considered here, a higher truncation order is not necessary.

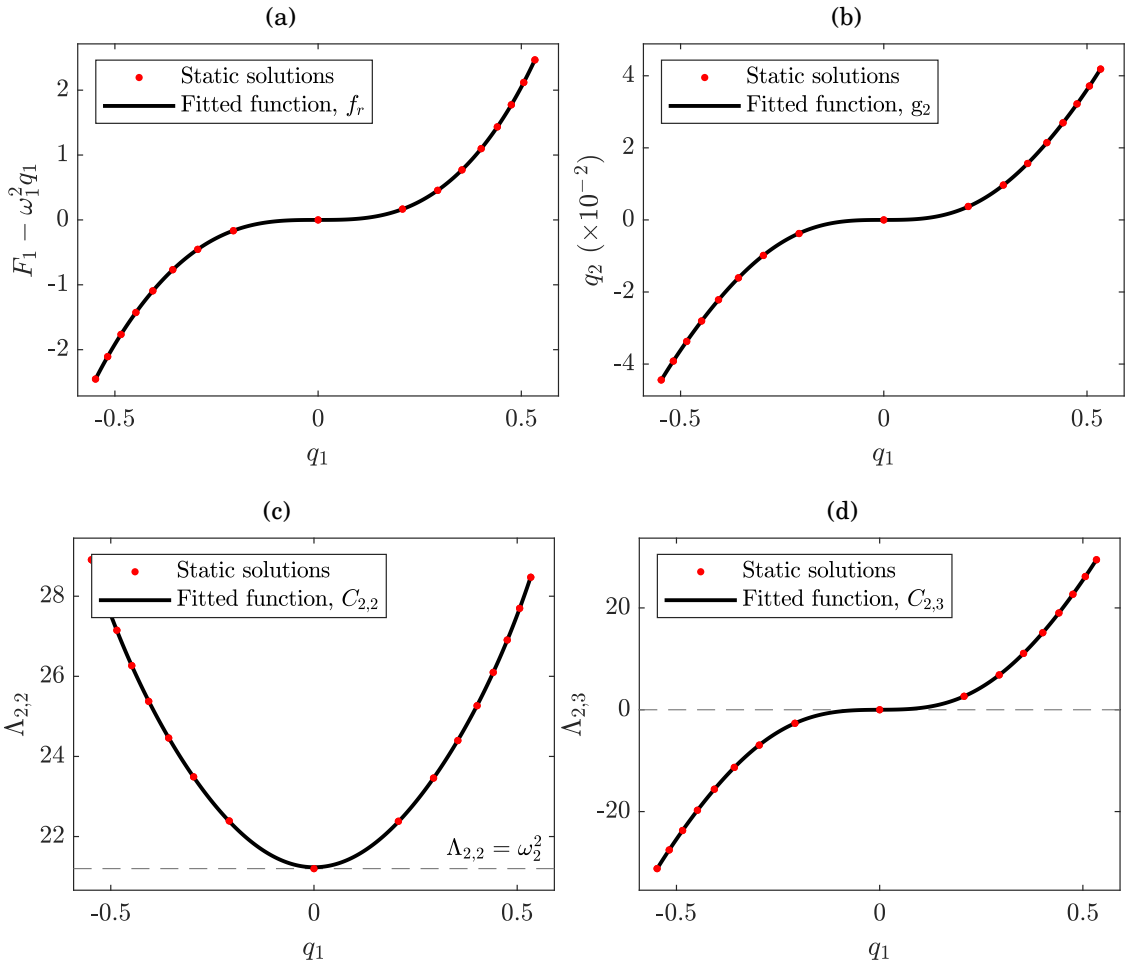

Figure 5.4. Examples of the calibration procedure for the single-DOF ROM of the oscillator: (a) function of reduced nonlinear internal forces, (b) quasi-static coupling function for the second mode, and (c,d) two different components of the tangent stiffness matrix. All quantities have been approximated as seventh-order polynomial functions of the reduced coordinate.

It should be noted that modes 2–4 are not modelled directly, but their response is approximated based on the response of the first (reduced) mode, using the quasi-static coupling functions. It can be seen that the primary response of the reduced mode (q_1), and that of the high-frequency condensed modes (q_3 and q_4), can be accurately predicted by the ROM. As expected, however, the internal resonance between the first and second mode near $\Omega = 1.6\,\mathrm{rad\,s^{-1}}$ cannot be captured. This is due to the dynamic energy transfer that takes place during an internal resonance — an effect that the static condensation approach is unable to capture.

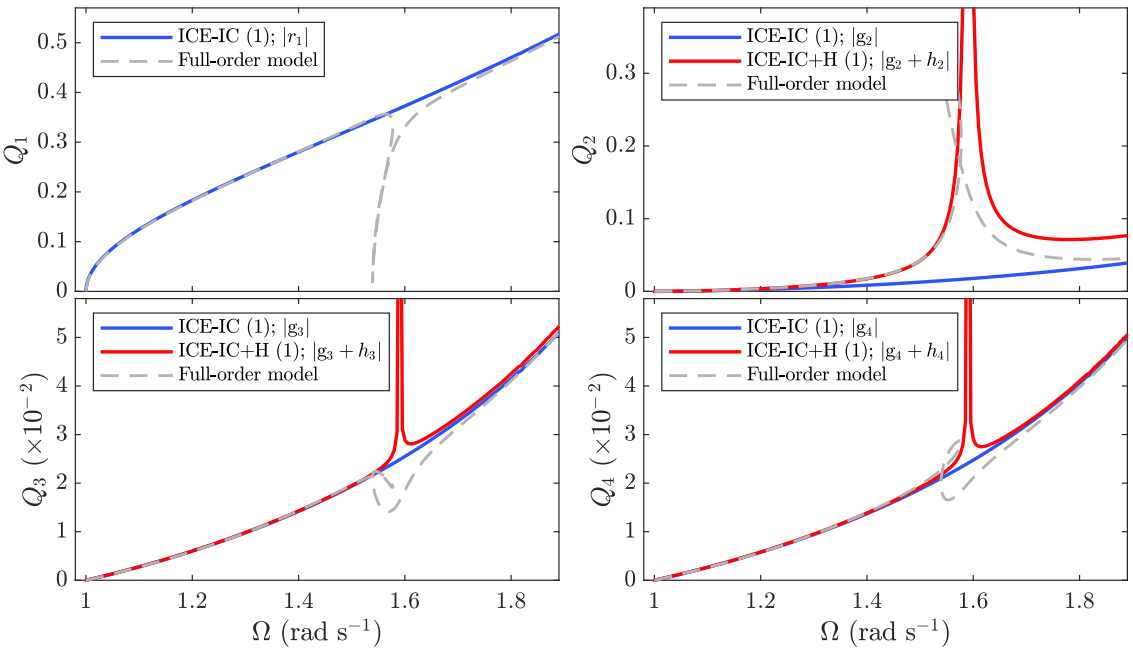

Figure 5.5. Backbone curve of the seventh-order, single-DOF ICE-IC ROM of the oscillator (blue lines). The backbone curve of the ROM when the static condensation error is taken into account, using the proposed method, is represented by red lines. The first backbone curve of the full-order system is also shown for reference (dashed grey lines).

5.4.2 Internal resonance prediction

Using equation (5.21b) and the harmonic balance method, as described in section 5.3.2, the error associated with the static condensation of each mode can now be estimated. To achieve this, the elements of the tangent stiffness matrix corresponding to the condensed modes, i.e. $\mathbf{\Lambda}_{\text{tan},s} = \mathbf{\Phi}_s^{\intercal}\mathbf{K}_{\text{tan}}\mathbf{\Phi}_s$, must be approximated as functions of the reduced coordinates.[2] Similar to the approximation of the reduced nonlinear stiffness functions and the quasi-static coupling functions, these are computed in a least-squares manner, based on the same set of full-order nonlinear static solutions. Examples of this are shown in figures 5.4 (c) and (d), for two different components of the modal tangent stiffness matrix.

The improved prediction of the reduced backbone curves, which takes into account the approximated error arising from the static condensation (with $N_h = 7$), is now represented by red lines in figure 5.5. From this it can be seen that, as the response frequency increases, the magnitude of h_2 relative to g_2 becomes increasingly large

[2]Note that, by definition, $\mathbf{\Lambda} := \mathbf{\Lambda}_{\text{tan}}(\mathbf{q} = \mathbf{0})$.

until $\Omega \approx 1.6\,\mathrm{rad}\,s^{-1}$, before it rapidly decreases again.[3] This singularity-type behaviour is caused by the third harmonic component of h_2, and it indicates that a dynamic interaction between the first and second modes exists, without the need for simulating the dynamics of both modes simultaneously. This suggests that, in this region, a single-mode ROM is no longer able to capture the dynamics of the full-order model, and the second mode must be included in the reduction basis. Note that, when considering FE models using commercial packages, the backbone curves of the full-order model cannot readily be computed. As such, significant features of the system, such as internal resonances, can often be overlooked during model reduction. With the proposed method, the existence of such dynamic interactions can be predicted, without the need for expensive full-order simulations.

5.4.3 Two-mode ROM results

A 2-DOF, seventh-order ROM ($\boldsymbol{\Phi}_r = \begin{bmatrix}\boldsymbol{\phi}_1 & \boldsymbol{\phi}_2\end{bmatrix}$, $\boldsymbol{\Phi}_s = \begin{bmatrix}\boldsymbol{\phi}_3 & \boldsymbol{\phi}_4\end{bmatrix}$) is now computed using the same procedure, i.e. according to the ICE-IC method. The dataset used to calibrate the ROM consists of a series of static load cases where either one or both of the reduced modes are forced directly. The amplitude of the maximum force applied to either mode is $|F_1| = 3$, as before, and $|F_2| = 8$. As before, this dataset is used to approximate the components of the modal tangent stiffness matrix as polynomial functions of the reduced coordinates, in addition to the reduced nonlinear stiffness functions and quasi-static coupling functions.

The first backbone curve of the 2-DOF ROM is shown in figure 5.6, in the projection of modal amplitudes against fundamental response frequency. The ROM (blue lines) is now able to accurately capture the dynamic behaviour of the full-order system for the whole range of frequencies considered. In this case, the additional treatment proposed here (red lines), acts as a tool for validating the ROM, as it indicates that the static condensation approximation is sufficiently accurate; this is determined by observing that the contribution from $\mathbf{h}$ is negligible for both condensed modes. In the next section, the proposed method is demonstrated using a finite element model of a clamped-clamped beam.

[3] It should be noted that, in the region where $|h_2|$ is relatively large, the smallness assumption is violated, resulting in mispredictions of the static condensation errors in modes 3 and 4. Nevertheless, the early growth of h_2 indicates the onset of a dynamic interaction, whilst the exact modal vibration amplitudes are of little importance.

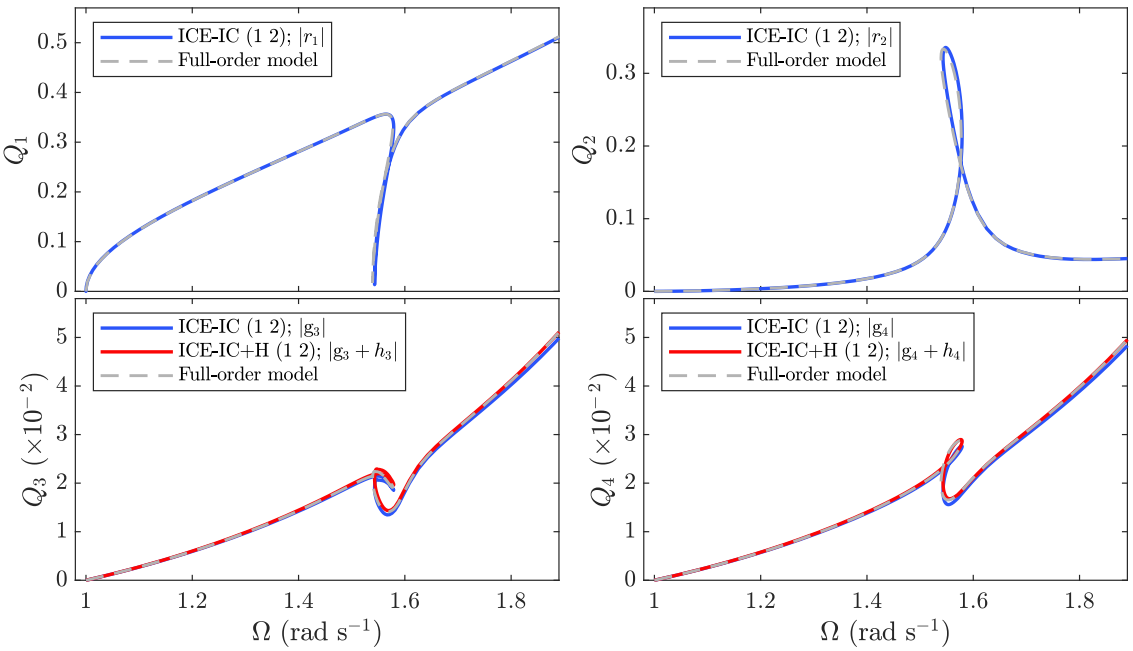

Figure 5.6. First backbone curve of the seventh-order, 2-DOF ICE-IC ROM of the oscillator (blue lines). The backbone curve of the ROM when the static condensation error is taken into account, using the proposed method, is represented by red lines. The first backbone curve of the full-order system is also shown for reference (dashed grey lines).

5.5 Application to FE model of a clamped-clamped beam

We now consider a geometrically nonlinear model of a clamped-clamped beam, constructed using the commercial FE software Abaqus. The beam model is identical to the one studied in Chapter 4. It has a length of 300 mm and a rectangular cross-section of 25 mm × 1 mm, and is made of steel with a Young's modulus of 205 GPa, density of 7800 kg m^{-3} and Poisson's ratio of 0.3. The mesh consists of 120 shear deformable, three-node quadratic beam elements (type B32), resulting in 1434 DOFs.

A quintic single-DOF ROM of the first (bending) mode is computed using the ICE method, with modes 3, 6, 72 and 129 included in the condensed basis; these correspond to the second and third symmetric bending modes, and the first and second symmetric axial modes, respectively.[4] The static solution dataset used to

[4]Here, the condensed basis was chosen based on the relative amplitude of each mode evaluated at the static solutions, as discussed in Chapter 4. For more complex structures, more intricate methods of selecting good candidate modes for the condensed basis may be necessary — this remains a topic for future investigation. The reader is referred to Buza *et al.* (2021) for a recent work on mode-selection criteria based on the theory of spectral submanifolds.

calibrate the ROM consists of four load cases where the static force applied to the first mode is $F_1 = \{-45, -22.5, +22.5, +45\}$, resulting in a maximum static transverse deflection of 1.13 mm at the beam midspan. For this model, the computation time for each load case is about 25 seconds on a standard computer. As before, the fitting procedure for the reduced nonlinear stiffness functions, the quasi-static coupling functions, and the tangent stiffness functions for the condensed modes,[5] is carried out in a least-squares manner.

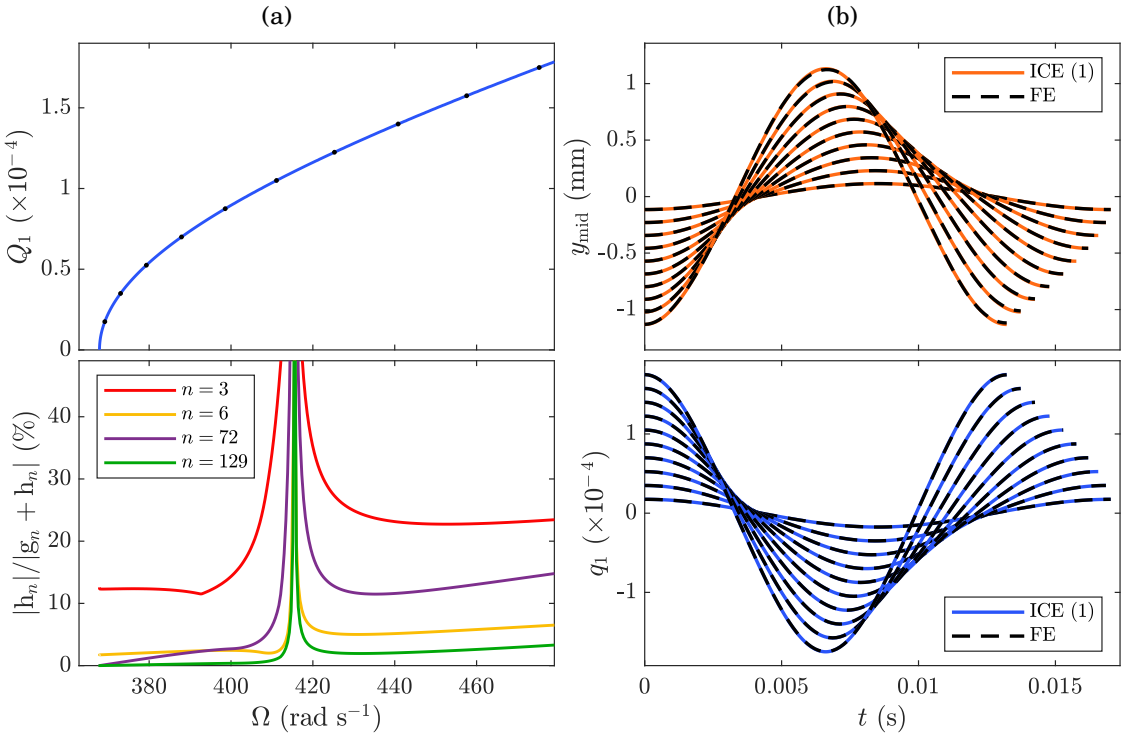

Figure 5.7. (a) Backbone curve of the quintic single-DOF ROM of the beam (top), and the corresponding error associated with the static condensation of each mode (bottom). (b) Comparison between the periodic responses predicted by the ROM and the responses of the FE model, for 10 different sets of initial conditions which correspond to the black dots on the backbone curve.

Figure 5.7 (a) shows the backbone curve of the single-DOF ROM (top), as well as the corresponding normalised amplitude of the error in the condensed modes (bottom). As the backbone curves of the full-order FE model cannot readily be computed, and thus cannot be directly compared to those of the ROM, the accuracy of the ROM is

[5] For this additional step, the tangent stiffness matrix of the full-order model must be evaluated at each static solution — this can be readily extracted from the FE package.

assessed by comparing a set of reduced NNMs to the dynamic response of the FE model when the corresponding initial conditions are applied, for a wide range of response frequencies. The initial conditions are enforced in the form of initial applied modal forces, as proposed in Kuether and Allen (2014). The periodic orbits of the ROM are compared to the FE response in the time domain, as shown in figure 5.7 (b). From this, it can be seen that the ICE method can provide accurate results for the reduction of the clamped-clamped beam model, even with a single-mode ROM — this agrees with observations seen in the literature (Kuether *et al.*, 2015; Hollkamp and Gordon, 2008; Gordon and Hollkamp, 2011), as well as the findings discussed in Chapters 3 and 4.

Interestingly, while the standard ROM results, as shown in 5.7 (b), indicate good agreement with the full-order model, the results obtained from the error-monitoring treatment suggest that there is a strong dynamic interaction between the first and

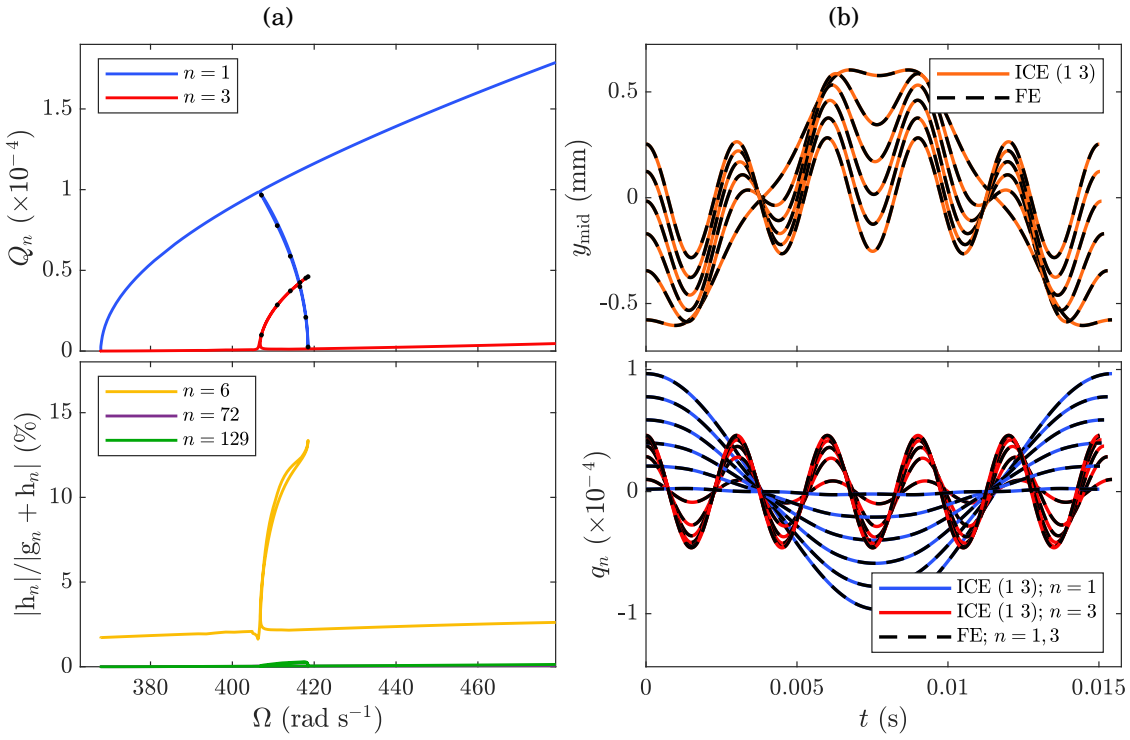

Figure 5.8. (a) First backbone curve of the quintic 2-DOF ROM of the beam (top), and the corresponding error associated with the static condensation of each mode (bottom). (b) Comparison between the periodic responses predicted by the ROM and the responses of the FE model, for 3 different sets of initial conditions which correspond to the black dots on the backbone curve.

third modes of the beam near $\Omega = 410\,\mathrm{rad\,s^{-1}}$, which the single-mode ROM is unable to capture. Note that, whilst the h components of modes 6, 72 and 129 are also large, the component of mode 3 is the largest, and begins its rapid growth at a lower frequency than the other modes. As such, mode 3 is treated as the candidate for a dynamic interaction. Specifically, this is associated with the amplitude of the fifth harmonic of the third mode. This result points to the existence of a 1:5 internal resonance between the first and third modes — a feature of flat clamped-clamped beams which has been widely observed in the literature, see for example Kuether *et al.* (2015); Givois *et al.* (2019).

In order to verify this observation, a quintic 2-DOF ICE ROM of the beam is computed, with $\boldsymbol{\Phi}_r = \begin{bmatrix}\boldsymbol{\phi}_1 & \boldsymbol{\phi}_3\end{bmatrix}$ and $\boldsymbol{\Phi}_s = \begin{bmatrix}\boldsymbol{\phi}_6 & \boldsymbol{\phi}_{72} & \boldsymbol{\phi}_{129}\end{bmatrix}$. The calibration dataset consists of 24 load cases, where the maximum force applied in each reduced mode is $F_1 = 45$ and $F_3 = 360$. The resulting backbone curve is shown in figure 5.8 (a). It can be seen that the ROM now exhibits a 1:5 internal resonance, whilst the error predicted using the proposed method remains relatively small. As before, the accuracy of the reduced internally-resonant NNMs is verified by comparing them to the corresponding set of responses of the full-order model (figure 5.8 (b)).

It should be noted that, in addition to enabling the internal resonance to be modelled, the 2-DOF ROM also leads to more accurate response predictions on the primary backbone curve. The accuracy of each reduced NNM is quantified using the periodicity metric ϵ, as defined in VanDamme and Allen (2017), i.e.

$$\epsilon = \frac{\|\mathbf{x}_T - \mathbf{x}_0\|}{\|\mathbf{x}_0\|}, \tag{5.35}$$

where $\mathbf{x}_0$ is the displacement vector of the FE model at $t = 0$, which is imposed as an initial condition based on the reduced NNM, and $\mathbf{x}_T$ is the displacement vector of the FE model after one period. A smaller ϵ value indicates a response which is closer to being periodic, and thus a more accurate ROM. The computed periodicity values for different NNMs on the primary backbone curves, both for the single- and 2-DOF ROMs, are shown in figure 5.9. The results suggest that the third mode of the FE model becomes increasingly important for response frequencies higher than $\sim 420\,\mathrm{rad\,s^{-1}}$. This is in qualitative agreement with the results shown in 5.7 (a), and further confirms the validity of the error-approximation procedure.

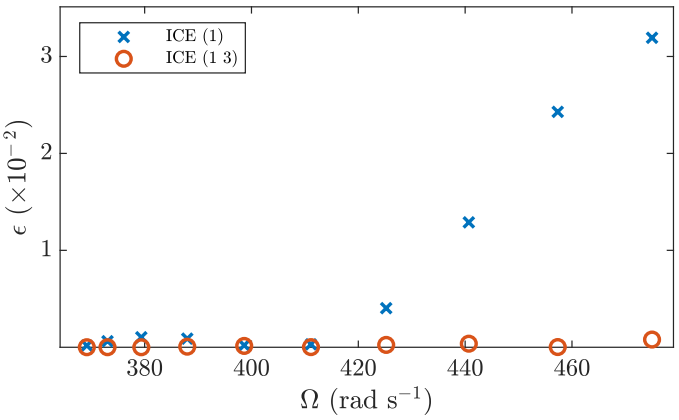

Figure 5.9. Plot of the periodicity error of the FE model, for different sets of initial conditions given by the single-DOF (blue crosses) and 2-DOF (red circles) ICE ROMs of the clamped-clamped beam.

5.6 Summary

This chapter has shown how the existence of internal resonances may be predicted in a computationally efficient manner during model order reduction of geometrically nonlinear structures. Specifically, a simple 4-DOF oscillator was used as a motivating example to show how each modal coordinate in a nonlinear system may be represented as the sum of a component that is quasi-statically coupled to a small number of coordinates, which must form the reduction basis in a ROM, and a component that is dynamically independent of them. The latter part may be considered as the error arising from static condensation, which is the concept on which methods such as the ICE(-IC) rely, and is typically applied to structures characterised by slow/fast dynamics. The harmonic balance method was used to approximate the error dynamics independently of the reduced dynamics, thus enabling any dynamic interaction between the reduced and condensed modes to be identified. This can be achieved in a very computationally efficient manner, as a linear approximation of the error dynamics is considered. The proposed method was demonstrated using the simple oscillator, as well as a finite element model of a clamped-clamped beam, and it was shown how the existence of a 1:3 and a 1:5 internal resonance, respectively, could be predicted based on single-mode ROMs.

The significance of this development is twofold. Firstly, the method presented here enables the identification of the modes which must form the reduction basis, without relying on knowledge of the full-order dynamics. Secondly, this method can serve as a

computationally cheap validation of ROMs without the need for full-order simulations, which can sometimes be infeasible to obtain. This removes the need for cumbersome trial-and-error processes and case-by-case treatment guided by empirical rules, and is a key step towards developing reduced-order modelling methods which can be applied systematically to a broad range of structures.

Chapter 6

Nonconservative structures

In previous chapters, the quality of the computed ROMs has been assessed using backbone curves, i.e. based on the response of the underlying conservative structure. Whilst backbone curves provide invaluable insight into the nonlinear behaviour of the structure and are closely related to forced response curves, it is often useful to compute the forced response of the structure directly. This chapter demonstrates how indirect reduced-order modelling techniques can be extended to nonconservative structures, using a nonlinear mapping of the physical DOFs into the reduced coordinates. The proposed method is contrasted with the traditional approach, which relies on a linear projection of the nonconservative forces onto the reduced subspace; as a result, only the nonconservative forces acting directly on the reduced modes can be captured, whilst any energy gained or dissipated by the statically condensed modes is neglected. This can lead to significant inaccuracies in the ROM predictions, which is demonstrated using a 2-DOF oscillator, an FE model of an axially-excited inclined cable, and an FE model of a cantilever beam. The proposed method enables the nonconservative forces acting on the statically condensed modes to be accounted for in the reduced dynamics. Excellent agreement is observed between the forced response curves of the full-order models and those of the proposed ROMs for all three structures.

Publication resulting from this work

Nicolaidou, E., Hill, T. L., and Neild, S. A. (2022). Nonlinear mapping of nonconservative forces for reduced-order modelling. *Proceedings of the Royal Society A: Mathematical, Physical and Engineering Sciences*, 478(2268):20220522

6.1 Introduction

Traditionally, the ICE method has suffered from limitations associated with the lack of invariance of the resulting ROMs. In a practical sense, this means that the ROMs are sensitive to the magnitude of the static forces used to obtain the calibration dataset (Gordon and Hollkamp, 2011), and as such can only remain accurate in a very limited range of operating conditions. As discussed in Chapters 3 and 4, this is a consequence of the fact that the reduced dynamics are obtained based on a *linear mapping*[1] between the physical DOFs of the FE model and the reduced coordinates, which is inherently unable to correctly capture the nonlinear modal couplings. It has been shown that, when a *nonlinear mapping* is used instead, the reduced dynamics must include not only higher orders of nonlinearity (Nicolaidou *et al.*, 2020b), but also some additional velocity- and acceleration-dependent terms associated with the inertia of the statically condensed modes (Nicolaidou *et al.*, 2020a). Similar results are seen in other *direct* reduced-order modelling methodologies which rely on a nonlinear mapping, including the quadratic manifold approach (Jain *et al.*, 2017; Rutzmoser *et al.*, 2017), as well as the more general concept of an invariant manifold based on normal form theory (Pesheck *et al.*, 2001; Shaw and Pierre, 1993; Touzé *et al.*, 2004b).

Nevertheless, these developments of the ICE method have focussed on the reduction of the underlying *conservative* structure, and computation of backbone curves. Whilst backbone curves are closely related to forced response curves, and offer rich insight into the dynamics of a system, it is often useful to compute the forced response of the structure directly. This chapter shows how indirect reduced-order modelling methods can be extended to nonconservative systems. The *nonconservative forces* acting on the structure are reduced based on a nonlinear mapping which, relative to the traditional, linear mapping, gives rise to some additional terms in the reduced dynamics, referred to as *force compensation*. These capture the nonconservative forces acting on the statically condensed modes, which the traditional method neglects, and bear similarity with expressions obtained using the forced/damped invariant manifold approach (Touzé and Amabili, 2006; Touzé *et al.*, 2008; Vizzaccaro *et al.*, 2022; Opreni *et al.*, 2022; Jain and Haller, 2022). In the proposed formulation, the physical DOFs of the FE model are mapped directly into the reduced coordinates *without* passing through the full modal coordinates, similar to the approach proposed in

[1] It should be noted that, whilst the stress manifold obtained using the ICE method is a manifestation of a *nonlinear* mapping which implicitly captures the effect of membrane stretching, the form of the reduced dynamics is a result of the *linear* transform $\mathbf{x} = \mathbf{\Phi}_r \mathbf{r}$, as discussed earlier in this thesis.

Vizzaccaro *et al.* (2021). This circumvents the need for a full modal transform, which can be a bottleneck when considering large FE models, and allows for straightforward modelling of point forces/moments.

The rest of this chapter is structures as follows. In section 6.2, the 2-DOF oscillator introduced in Chapter 3 is used as a motivating example to show how the traditional method, based on a linear mapping, is unable to capture the damping in the statically condensed mode, and leads to significant overestimations of the response amplitude. Section 6.3 introduces the proposed method, which achieves reduction through a nonlinear mapping, such that any energy gained or dissipated by the condensed modes can be accounted for. Section 6.4 revisits the oscillator example, and it is shown that the augmented ROM can capture the full-order response very accurately. In section 6.5, the proposed method is applied to an FE model of an axially-excited inclined cable. It is shown that the proposed ROM is extremely accurate in capturing not only the primary resonance curve, but also a parametric resonance, which the traditional approach neglects. In section 6.6, the proposed method is applied for the reduction of the large-amplitude forced/damped dynamics of a cantilever beam, modelled using commercial FE software. Two loading scenarios are considered: one with a constant-direction force and one with a follower force, both of which are applied at the free end of the beam. Finally, conclusions are summarised in section 6.7.

6.2 Motivating example

In this section, the simple 2-DOF oscillator which was previously introduced in Chapter 3,[2] is considered as a motivating example. The oscillator consists of a mass $m = 0.1\,\mathrm{kg}$, which is free to move in the x–y plane. It is constrained by two springs of length $\ell = 0.1\,\mathrm{m}$, which are undeformed and oriented along the x- and y-directions at the equilibrium configuration, as shown in figure 6.1. The springs are linearly elastic, with stiffness coefficients $k_1 = 10\,\mathrm{N\,m^{-1}}$ and $k_2 = 1000\,\mathrm{N\,m^{-1}}$, and obey a linear strain–displacement relationship.

The nonconservative forces acting on the oscillator are due to harmonic external excitation and Rayleigh damping, which is the most widely used dissipation model in

[2]Note that, here, the equations of motion of the oscillator are considered in their original form, *without* using a Taylor series expansion to truncate them up to the cubic order, as was done in Chapter 3.

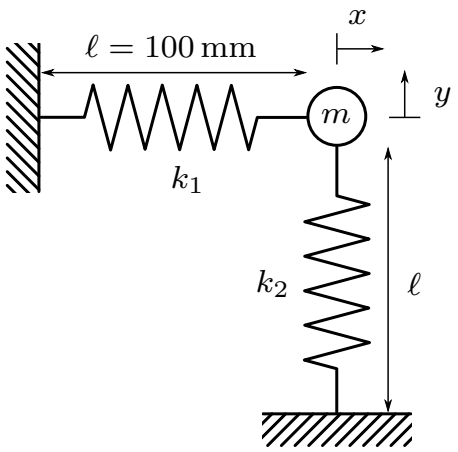

Figure 6.1. Schematic diagram of the single-mass, 2-DOF oscillator at its equilibrium position.

FE software. The equations of motion can be written in the form

$$m\ddot{x} + k_1 x + f_1(x,y) = P_1 \cos(\Omega t) - c_1 \dot{x} \tag{6.1a}$$

$$m\ddot{y} + k_2 y + f_2(x,y) = P_2 \cos(\Omega t) - c_2 \dot{y} \tag{6.1b}$$

where P_1 and P_2 are the excitation amplitudes in the x- and y-directions, respectively, $c_1 = \alpha m + \beta k_1$, $c_2 = \alpha m + \beta k_2$, and α and β are the mass- and stiffness-proportional Rayleigh damping coefficients, respectively.

6.2.1 Conservative dynamics

The stiffness coefficient of the vertical spring is much larger than that of the horizontal one, resulting in a large separation between the natural frequencies of the oscillator ($\omega_2/\omega_1 = 10$). As such, the dynamics of this system are governed primarily by the first mode. First, considering the underlying conservative system, a single-DOF reduced-order model can be expressed in the form

$$\ddot{r} + \frac{k_1}{m} r + D(r,\dot{r},\ddot{r}) = 0, \tag{6.2}$$

where r is the reduced coordinate, and the function D can differ both qualitatively, depending on the reduction methodology, as well as quantitatively, depending on the dataset used to approximate it. For example, using the ICE method (Hollkamp and Gordon, 2008), D takes the form of a nonlinear polynomial of the reduced

displacement, i.e.

$$D(r,\dot{r},\ddot{r}) = f_r(r) = \sum_{k=2}^{K} A_k r^k, \tag{6.3}$$

where f_r is the function of nonlinear restoring forces in the reduced space, and A_k are coefficients to be approximated up to the truncation order K, using a static solution dataset from the full-order model. Using the more generally applicable ICE-IC method proposed in Chapter 4, the reduced dynamics include some additional terms associated with the inertia of the condensed mode, i.e.

$$D(r,\dot{r},\ddot{r}) = f_r(r) + m\left(\frac{d\theta}{dr}\right)^2 \ddot{r} + m\frac{d\theta}{dr}\frac{d^2\theta}{dr^2}\dot{r}^2, \tag{6.4}$$

where

$$\theta(r) = \sum_{k=2}^{K} B_k r^k \tag{6.5}$$

is a function characterising the (nonlinear) quasi-static coupling between the vertical displacement of the oscillator, y, and the reduced coordinate, r.[3] Its coefficients, B_k, are computed via regression analysis, as with $f_r(r)$ above.

The static solution dataset used to approximate the two unknown functions, $f_r(r)$ and $\theta(r)$, is obtained by applying a static force F_1 in the first mode, and extracting the

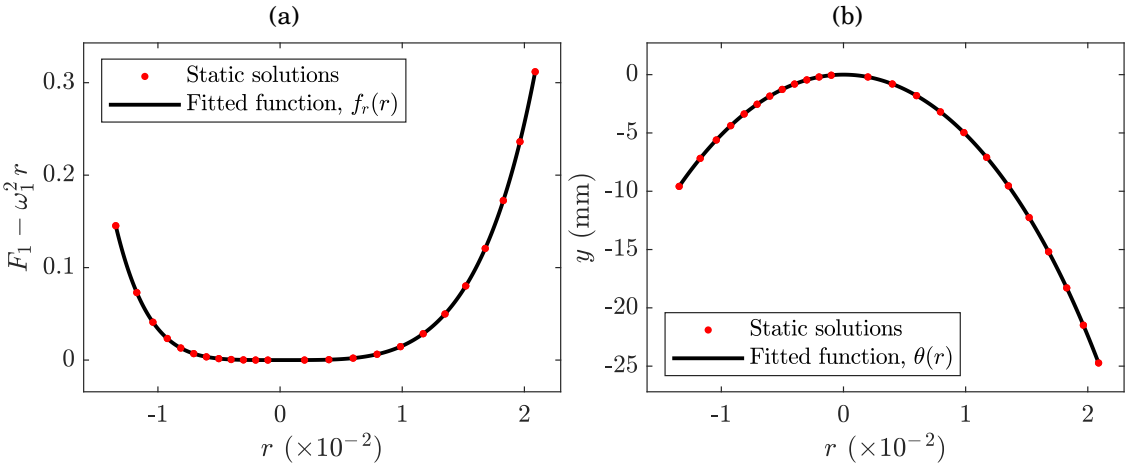

Figure 6.2. The static solution dataset used to approximate (a) the function of nonlinear restoring forces in the reduced space, and (b) the quasi-static coupling function.

[3] Equation (6.4) can be obtained using the nonlinear mapping $\mathbf{x} = [x \quad y]^\intercal = \left[r/\sqrt{m} \quad \theta(r)\right]^\intercal$, as discussed in Chapter 4. Note that, using the notation that will later be introduced in section 6.3, this is equivalent to $\mathbf{x} = \boldsymbol{\Phi}_r \mathbf{r} + \theta(\mathbf{r})$ with $\mathbf{r} = [r]$, $\boldsymbol{\Phi}_r = \left[1/\sqrt{m} \quad 0\right]^\intercal$ and $\theta(r) = \left[0 \quad \theta(r)\right]^\intercal$, as the physical coordinates of the oscillator are linearly uncoupled.

corresponding static displacement of the oscillator. Here, the dataset consists of 12 load cases where F_1 is increased in equal intervals from 0 to +2.4, and 12 load cases where F_1 is decreased in equal intervals from 0 to −1.2. Then, $f_r(r)$ is approximated using the $\{F_1 - \omega_1^2 r_{\text{st}}, r_{\text{st}}\}$ dataset, as shown in figure 6.2 (a), where r_{st} is the static displacement of the first mode and $\omega_1^2 = k_1/m$. Similarly, $\theta(r)$ is approximated using the $\{y_{\text{st}}, r_{\text{st}}\}$ dataset, as shown in figure 6.2 (b). The estimated parameters, for $K = 9$, are listed in table 6.1.

Table 6.1. Estimated coefficients of the function of reduced nonlinear restoring forces, $f_r(r)$, and the quasi-static coupling function, $\theta(r)$, for $K = 9$.

k	2	3	4	5
A_k	$+4.89 \times 10^{-1}$	$-6.53 \times 10^{+1}$	$+3.85 \times 10^{+5}$	$-1.14 \times 10^{+7}$
B_k	$-5.00 \times 10^{+1}$	$+1.62 \times 10^{+1}$	$-1.29 \times 10^{+4}$	$+2.44 \times 10^{+4}$
k	6	7	8	9
A_k	$+6.52 \times 10^{+8}$	$-2.63 \times 10^{+10}$	$+7.04 \times 10^{+11}$	$-3.17 \times 10^{+12}$
B_k	$-8.39 \times 10^{+6}$	$+1.54 \times 10^{+8}$	$-3.21 \times 10^{+9}$	$-2.27 \times 10^{+11}$

Figure 6.3 shows the backbone curves of the ninth-order, single-DOF ICE and ICE-IC ROMs, which have been computed according to equations (6.3) and (6.4), respectively. These are compared to the first backbone curve of the full-order system. It can be seen that, due to the significant effect of the inertia of the statically coupled second mode, a ROM that includes inertial compensation (Nicolaidou *et al.*,

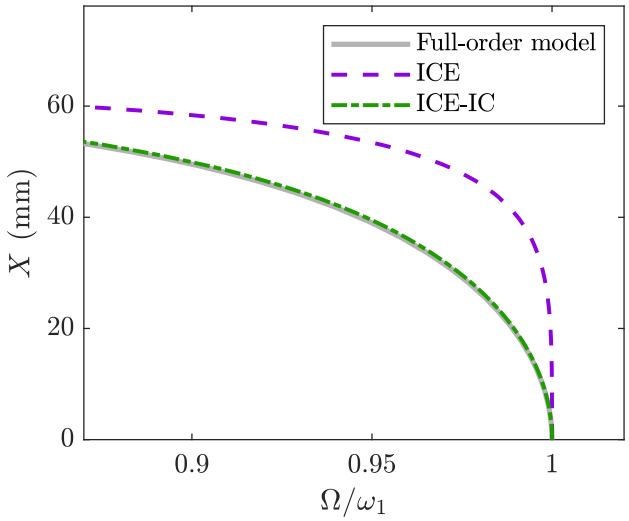

Figure 6.3. Comparison between the first backbone curve of the 2-DOF oscillator, and those of the single-DOF ICE and ICE-IC ROMs.

2020a) is required in order to accurately capture the conservative dynamics of the oscillator. This observation is in agreement with similar studies in the literature based on the theory of invariant manifolds (Touzé *et al.*, 2004a), which have found that neglecting this effect can lead to not only quantitatively inaccurate results, but even erroneous predictions of the type of nonlinearity (e.g. hardening rather than softening behaviour).

6.2.2 Nonconservative dynamics

The focus of this chapter is on how the *nonconservative* forces in equations (6.1) may be reduced. Traditionally, this is achieved via a linear projection onto the space spanned by the reduced modeshapes (Mignolet *et al.*, 2013; Van Damme *et al.*, 2020). The resulting terms are then appended onto the conservative ROM, equation (6.2), i.e.

$$\ddot{r} + \frac{k_1}{m} r + D(r, \dot{r}, \ddot{r}) = \frac{P_1}{\sqrt{m}} \cos(\Omega t) - \frac{c_1}{m} \dot{r}. \tag{6.6}$$

This approach is employed here to compute the forced response of the oscillator in the vicinity of $\Omega \approx \omega_1$, with $\alpha = 0$, $\beta = 10^{-3}$ s, $P_1 = 5 \times 10^{-3}$ N and $P_2 = 0$, based on both an ICE ROM (equation (6.3)) and an ICE-IC ROM (equation (6.4)). These are compared to the forced response of the full-order model in figure 6.4. It can be seen that, even

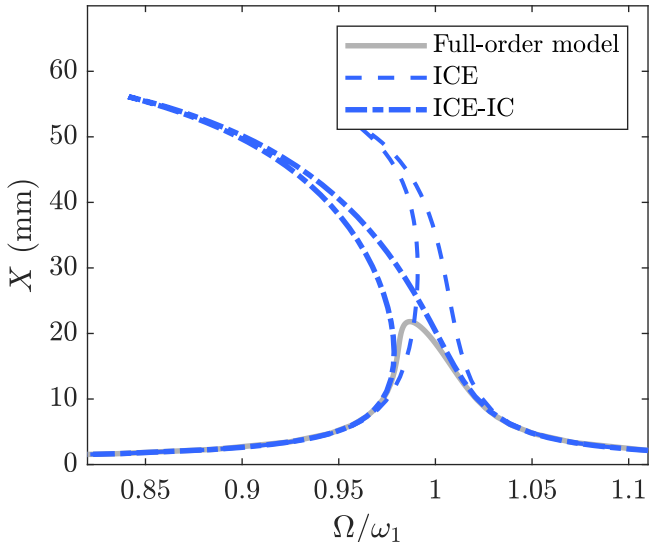

Figure 6.4. Comparison between the forced response curve of the 2-DOF oscillator in the vicinity of $\Omega \approx \omega_1$, with $\alpha = 0$, $\beta = 10^{-3}$ s, $P_1 = 5 \times 10^{-3}$ N and $P_2 = 0$ (grey line), and the corresponding forced response curves of the ICE(-IC) ROMs, obtained using a linear projection of the nonconservative forces (blue lines).

though the ICE-IC model is able to capture the conservative behaviour of the oscillator very accurately (as shown in figure 6.3), both ROMs significantly overestimate the amplitude of the nonconservative response of the oscillator. This is because the linear mapping is inherently unable to capture the damping present in the second mode. In the next section, it will be shown that any energy dissipated/gained by the statically coupled modes can be accounted for using a *nonlinear mapping* of the nonconservative forces.

6.3 Capturing the forces acting on the condensed modes

We start by considering the semi-discretised equations of motion of a nonconservative, geometrically nonlinear structure, i.e.

$$\mathbf{M}\ddot{\mathbf{x}} + \mathbf{K}\mathbf{x} + \mathbf{f}(\mathbf{x}) = \mathbf{F}(t, \mathbf{x}, \dot{\mathbf{x}}). \tag{6.7}$$

The conservative model on the left-hand side of equation (6.7) is typically obtained through a finite element procedure, whilst the nonconservative forces on the right-hand side are a result of any dissipative process and/or external excitation.

The dynamics of a structure are assumed to be governed by a small subset of its linear normal modes. As such, the full-order model may be reduced using the approximation

$$\mathbf{x} = \boldsymbol{\Phi}_r \mathbf{r} + \theta(\mathbf{r}), \tag{6.8}$$

such that

$$\dot{\mathbf{x}} = \left(\boldsymbol{\Phi}_r + \frac{\partial \theta}{\partial \mathbf{r}}\right)\dot{\mathbf{r}} \tag{6.9a}$$

$$\ddot{\mathbf{x}} = \left(\boldsymbol{\Phi}_r + \frac{\partial \theta}{\partial \mathbf{r}}\right)\ddot{\mathbf{r}} + \frac{\partial^2 \theta}{\partial \mathbf{r}^2}\dot{\mathbf{r}}\dot{\mathbf{r}}, \tag{6.9b}$$

where θ is a vector of quasi-static coupling functions *in the physical space*. The reduced dynamics are then obtained by substituting equations (6.8) and (6.9) into equation (6.7) and premultiplying by $\left(\frac{\partial \mathbf{x}}{\partial \mathbf{r}}\right)^{\mathsf{T}}$,[4] i.e.

$$\ddot{\mathbf{r}} + \underbrace{\left(\frac{\partial \theta}{\partial \mathbf{r}}\right)^{\mathsf{T}} \mathbf{M} \frac{\partial \theta}{\partial \mathbf{r}}\ddot{\mathbf{r}} + \left(\frac{\partial \theta}{\partial \mathbf{r}}\right)^{\mathsf{T}} \mathbf{M} \frac{\partial^2 \theta}{\partial \mathbf{r}^2}\dot{\mathbf{r}}\dot{\mathbf{r}}}_{\text{inertial compensation}} + \boldsymbol{\Lambda}_r \mathbf{r} + \mathbf{f}_r(\mathbf{r}) = \boldsymbol{\Phi}_r^{\mathsf{T}}\mathbf{F} + \underbrace{\left(\frac{\partial \theta}{\partial \mathbf{r}}\right)^{\mathsf{T}}\mathbf{F}}_{\text{force compensation}}, \tag{6.10}$$

[4] This ensures that the residual introduced by the projection approximation is orthogonal to the kinematically admissible displacements $\delta\mathbf{x}$ (Rutzmoser *et al.*, 2017).

where $\mathbf{\Lambda}_r$ contains the linear reduced coefficients along its main diagonal, and $\mathbf{f}_r(\mathbf{r})$ is to be approximated via regression analysis, as discussed earlier in this thesis. Note that the reduced conservative dynamics on the left-hand side of equation (6.10) are equivalent to those obtained using the unforced/undamped ICE-IC method introduced in Chapter 4. The above expression has been simplified by noting that, by definition, $\theta(\mathbf{r})$ must satisfy $\left(\frac{\partial \theta}{\partial \mathbf{r}}\right)^{\mathsf{T}}(\mathbf{K}\theta + \mathbf{f}_x(\mathbf{\Phi}_r\mathbf{r} + \theta)) = \mathbf{0}$, as it is computed based on static solution data where only the reduced modes are directly forced, as discussed in Chapter 4.

Equation (6.10) can be contrasted with the reduced equations of motion obtained using the standard ICE method, which relies on the linear mapping $\mathbf{x} = \mathbf{\Phi}_r\mathbf{r}$, i.e.

$$\ddot{\mathbf{r}} + \mathbf{\Lambda}_r\mathbf{r} + \mathbf{f}_r(\mathbf{r}) = \mathbf{\Phi}_r^{\mathsf{T}}\mathbf{F}. \tag{6.11}$$

The additional terms on the left-hand side of equation (6.10) relative to equation (6.11), which are collectively referred to as *inertial compensation* (IC), have been shown to account for the kinetic energy in the statically condensed modes in Chapter 4. Similarly, the additional terms on the right-hand side of equation (6.10), capture any energy gained or dissipated by the statically condensed modes through nonconservative forces; these are referred to as *force compensation* (FC).

The linear properties of the ROM, $\mathbf{\Phi}_r$ and $\mathbf{\Lambda}_r$, are directly computed using the full-order linear mass and stiffness matrices, whilst the nonlinear functions, $\mathbf{f}_r(\mathbf{r})$ and $\theta(\mathbf{r})$, are approximated in a least-squares manner using a nonlinear static solution dataset from the full-order model. It should be noted that the quasi-static coupling functions are now approximated in the physical space, i.e. a function is computed for each DOF, rather than for each relevant mode. Using the notation introduced earlier in this thesis, this is equivalent to $\theta(\mathbf{r}) \equiv \mathbf{\Phi}_s\,\mathbf{g}(\mathbf{r})$. As such, the modes which exhibit a strong quasi-static coupling to the reduced modes need not be explicitly identified, and performing a full modal transform is not required. This development is particularly advantageous when considering high-fidelity FE models with a very large number of DOFs, where performing a full linear modal transform is infeasible. It is worth highlighting that, since the quasi-static coupling function for each DOF is computed independently, the size of the least-squares problem associated with the function approximation does not increase. Instead, the number of least-squares problems to be solved increases in accordance with the number of DOFs of the FE model. Due to the efficiency of this procedure, the computational cost associated with this remains negligible.

6.4 Application to the 2-DOF oscillator

We now revisit the oscillator considered in section 6.2. A single-mode, nonconservative ROM which includes both inertial and force compensation (ICE-IC-FC) is computed according to equation (6.10). Its dynamics can be written as

$$\begin{aligned}\ddot{r} + m\left(\frac{d\theta}{dr}\right)^2 \ddot{r} + m\frac{d\theta}{dr}\frac{d^2\theta}{dr^2}\dot{r}^2 + \frac{k_1}{m}r + f_r(r) \\ = \left(\frac{P_1}{\sqrt{m}} + P_2\frac{d\theta}{dr}\right)\cos(\Omega t) - \left(\frac{c_1}{m} + c_2\left(\frac{d\theta}{dr}\right)^2\right)\dot{r}.\end{aligned} \tag{6.12}$$

The forced response of this ROM is shown in 6.5 (a) (top), for the same forcing/damping parameters as before. It can be seen that the proposed ROM (red line) can now reproduce the response of the full-order model very accurately. Relative to the baseline ICE-IC ROM considered in section 6.2 (equations (6.4) and (6.6)), and noting that $P_2 = 0$, the proposed ICE-IC-FC ROM (equation (6.12)) differs through the addition of a displacement-dependent damping term which accounts for the energy dissipated by the second mode. As such, the effective damping coefficient in the proposed ROM is equal to the linear damping coefficient of the first mode (c_1/m) at zero displacement, but increases as the response amplitude increases. This is shown in figure 6.5 (a) (bottom).

In the above example, the stiffness-proportional damping applied to the system results in a relatively large damping ratio in the second mode ($\zeta_1 = 0.5\%$, $\zeta_2 = 5\%$), and thus the correction term introduced by the force compensation method is significant. Mass-proportional damping ($\alpha = 1\,\mathrm{s}^{-1}$, $\beta = 0$) is now applied, such that the damping ratio in the second mode is much smaller ($\zeta_1 = 5\%$, $\zeta_2 = 0.5\%$). The forced response curves, with $P_1 = 5 \times 10^{-2} N$ and $P_2 = 0$, are shown in the top panel in figure 6.5 (b), and the corresponding effective damping coefficient in the ROMs is shown on the bottom. It can be seen that, as expected, the error in the response prediction of the baseline ROM is less significant, and the relative magnitude of the correction in the effective damping coefficient introduced by the force compensation method is smaller. These findings are supported by similar results reported in Touzé and Amabili (2006); Vizzaccaro *et al.* (2021) using the damped/forced invariant manifold approach.

In both of the above examples, no external excitation was applied to the second mode, such that the discrepancy between the response of the full-order model and that of the traditional ROM, is solely due to the viscous dissipation in the second mode, which the linear mapping fails to capture. The next section will show how, in

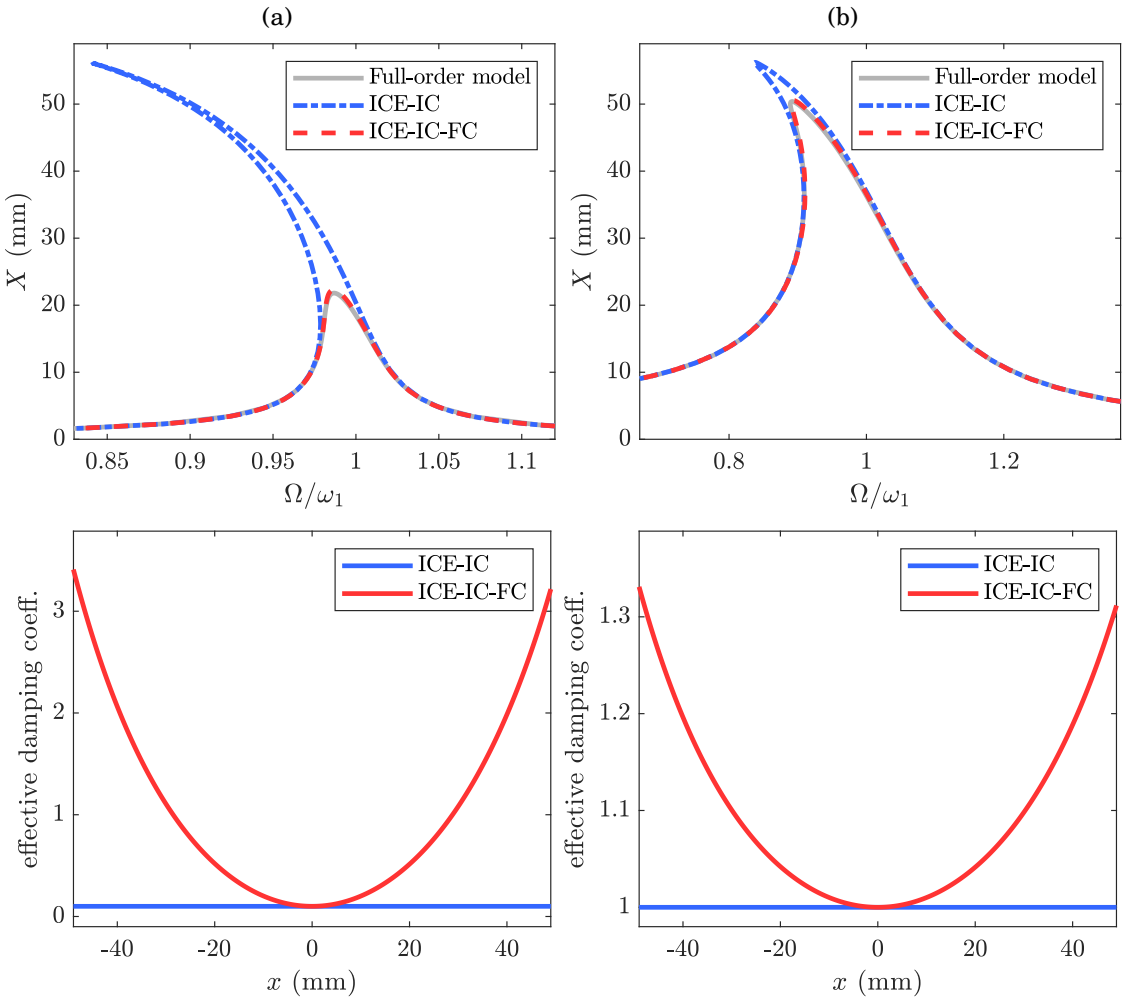

Figure 6.5. Top: forced response curves of the full-order model (grey line) and the ICE-IC ROMs obtained based on the linear (blue line) and the nonlinear (red line) mapping of the nonconservative forces. Bottom: the corresponding effective damping coefficient as the response of the ROM varies, for a system with (a) stiffness-proportional damping ($\alpha = 0$, $\beta = 10^{-3}$ s, $P_1 = 5 \times 10^{-3}$ N, $P_2 = 0$), and (b) mass-proportional damping ($\alpha = 1\,\mathrm{s}^{-1}$, $\beta = 0$ s, $P_1 = 5 \times 10^{-2}$ N, $P_2 = 0$).

a similar manner, the force compensation method can capture the forcing applied to modes that are not directly included in the reduction basis, which the traditional method would neglect.

6.5 Application to an axially-excited inclined cable

In this section, we consider a model of an inclined cable taut between two fixed end points, as shown in figure 6.6. The dynamics of the cable model are obtained through

a finite element discretisation, similar to the method in Nahon (1999). The FE model was developed in MATLAB and its accuracy has previously been verified in Hong *et al.* (2020), by comparing a reduced numerical model to the analytical model derived in Warnitchai *et al.* (1995), for a highly stressed horizontal cable.

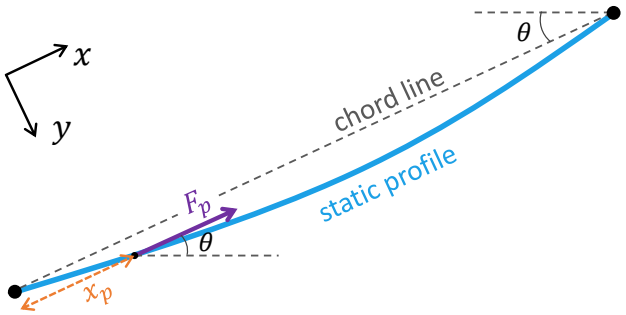

Figure 6.6. Schematic diagram of the axially-excited inclined cable model.

The cable is discretised into n identical, linearly elastic elements, connected in series between $n+1$ nodes. The two end nodes are fixed, whilst the remaining nodes are free to move in the x–y plane, resulting in a total of $2(n-1)$ DOFs. The inertia of the cable is modelled using variational mass lumping, giving rise to a consistent mass matrix (Felippa *et al.*, 2015). The cable has an unstretched length of L_0, uniform density ρ, Young's modulus E, a circular cross-section of diameter d, and its chord line is inclined at an angle θ from the horizontal. Axial stress is assumed to be uniformly distributed over the cross-sectional area, and a static axial pre-tension T is applied at both cable ends.

The forces acting on the cable are due to: (a) elasticity, (b) gravity, with gravitational constant g, (c) external harmonic excitation in the form $F_p = P\cos(\Omega t)$, acting in the axial direction at a location x_p along the chord length, as shown in figure 6.6, where P and Ω are the amplitude and frequency of excitation, respectively, and (d) viscous dissipation in the form of linear damping, with a constant damping ratio ζ in all modes.

6.5.1 Simplified FE model

A model with the following parameters is considered: $n=6$, $\theta=25°$, $L_0=1.5\,\mathrm{m}$, $\rho=3000\,\mathrm{kg\,m^{-3}}$, $E=200\,\mathrm{GPa}$, $d=5\,\mathrm{mm}$, $T=280\,\mathrm{N}$, $g=9.81\,\mathrm{m\,s^{-2}}$, and $\zeta=5\%$. Here, we are primarily interested in the effect of the axial external excitation on the dynamics of the cable, and less so in the interactions between bending modes. As such, we

first consider a simplified version of the full-order FE model described above, whereby any bending-mode coupling terms in the underlying Lagrangian of the system are neglected. In a Galerkin procedure, this is equivalent to intercepting a single bending mode for analysis.

This simplified 10-DOF model may then be reduced to a single DOF, whereby the axial dynamics are condensed using the quasi-static coupling approximation. The first backbone curve of the simplified full-order model, as well as those of cubic single-DOF ICE and ICE-IC ROMs based on the first mode, are shown in figure 6.7. It can be seen that the response of both ROMs is practically identical to that of the full-order model, irrespective of the inclusion of the inertial compensation terms. This is because the effect of in-plane inertia is often negligible in cable models, such that the more traditional ICE ROM is sufficient in accurately capturing the response of the full-order model (Warnitchai *et al.*, 1995; Hong *et al.*, 2020).

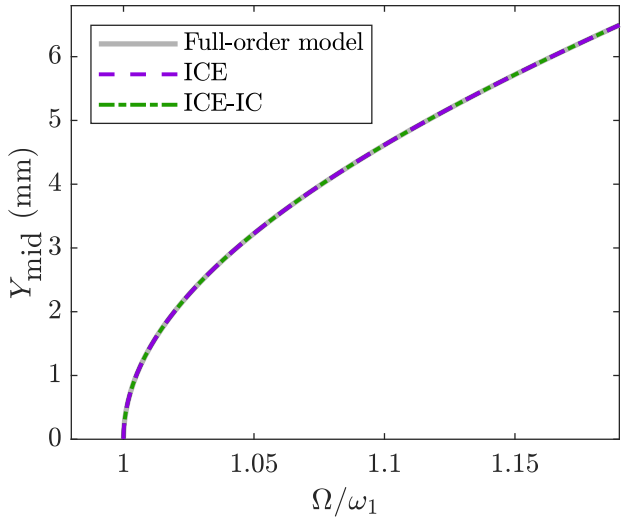

Figure 6.7. Comparison between the first backbone curve of the inclined cable model, and those of the single-DOF ICE and ICE-IC ROMs.

Figure 6.8 shows the forced response curve of the simplified FE model (grey line), as well as those of the ICE ROMs without force compensation (figure 6.8 (a), blue line) and with force compensation (figure 6.8 (b), red line), when a harmonic force with amplitude $P = 500\,\text{N}$ and frequency $\Omega \sim 2\omega_1$ is applied at the first free node of the cable ($x_p = L_0/6$). It can be observed that the cable exhibits a 2:1 parametric resonance, emanating from period-doubling bifurcation points (black crosses in figure 6.8) — this is a known and commonly observed phenomenon (Pinto da Costa *et al.*, 1996; Liu

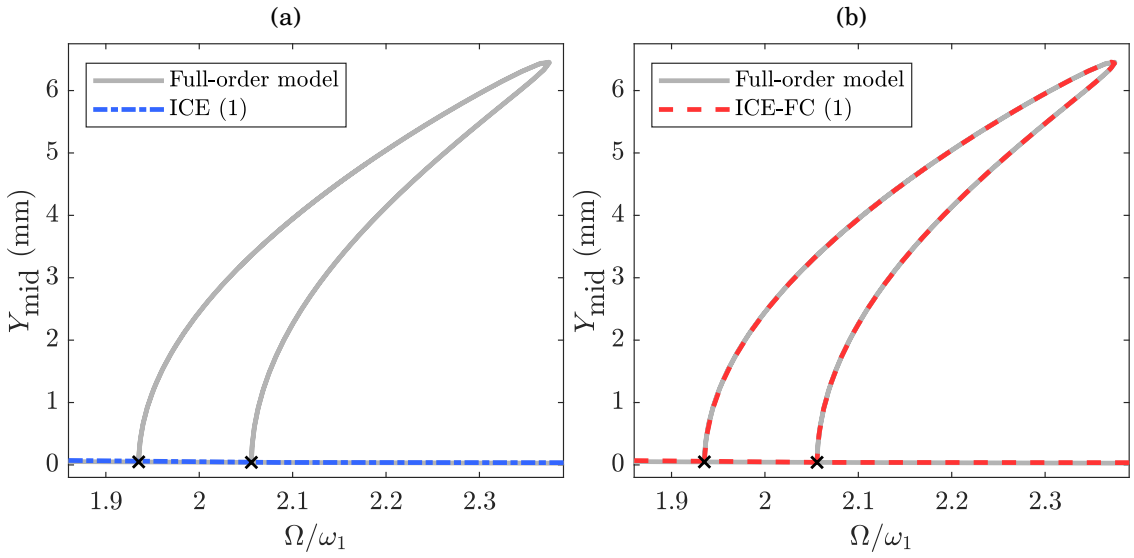

Figure 6.8. Forced response curves of the simplified version of the cable FE model (grey line) and the ICE ROMs obtained using (a) the linear (blue line) and (b) the nonlinear (red line) mapping of the nonconservative forces, computed in the vicinity of twice the first natural frequency with $P = 500\,\text{N}$. The period-doubling bifurcation points are marked with black crosses.

et al., 2020). Since the axial excitation is near-orthogonal to the reduced (bending) mode, the linear mapping is unable to capture this behaviour. On the other hand, the proposed ROM, which includes force compensation, can capture the parametric resonance and shows perfect agreement with the full-order model.

6.5.2 Fully-coupled FE model

The fully-coupled 10-DOF FE model is now considered. Its forced response curve for $P = 400\,\text{N}$ and $\Omega \sim 2\omega_1$ is shown in figure 6.9 (grey lines). Two main differences between the behaviour of the fully-coupled FE model and that of the simplified FE model can be observed, caused by the dynamic interactions with higher bending modes:

- the bifurcation points, marked with black crosses in figure 6.9 (a), are shifted to lower frequencies;
- the primary resonance curve, from which the parametric resonance emanates, has non-zero displacement amplitude.

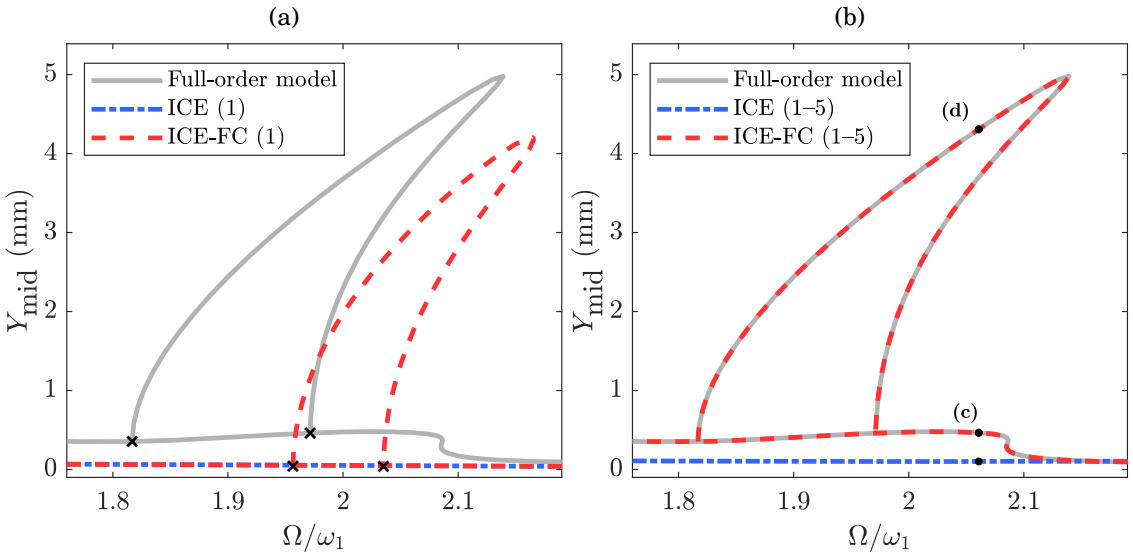

Figure 6.9. Forced response curves of the fully-coupled FE model (grey line) and the ICE ROMs obtained using the linear (blue line) and the nonlinear (red line) mapping of the nonconservative forces, computed in the vicinity of twice the first natural frequency with $P = 400\,\text{N}$: (a) single-mode ROMs, (b) five-mode ROMs.

As can be seen in figure 6.9 (a), even though the single-mode ICE-FC ROM can capture the fundamental behaviour of the cable (i.e. the existence of the parametric resonance), it is unable to capture the abovementioned effects. This is because the higher bending modes, whose natural frequencies are similar to that of the first bending mode ($\omega_2 \approx 2\omega_1$, $\omega_3 \approx 3\omega_1$, etc.), cannot adequately be modelled based on a static condensation procedure and must be directly included in the reduction basis.

As such, the corresponding forced response curves of 5-DOF ICE and ICE-FC ROMs are computed, which include all five bending modes in the reduction basis, whilst the axial dynamics are statically condensed — these are shown in figure 6.9 (b). It can be seen that, without the inclusion of the force compensation terms, the ICE ROM cannot accurately capture the primary resonance of the cable, whilst it altogether neglects the existence of the parametric resonance. The proposed ICE-FC ROM, however, can capture both solution branches with an extremely high level of accuracy.

In the next section, the proposed method is applied to a larger FE model of a cantilever beam, modelled using commercial FE software, which demonstrates its non-intrusive nature and suitability for industrial applications.

6.6 Application to FE model of a cantilever beam

This section considers the large-amplitude vibrations of a forced and damped cantilever beam, modelled using the commercial finite element software Abaqus. A schematic diagram of the beam is shown in figure 6.10, where a clamped boundary condition is imposed at $x = 0$. The beam has a length of $\ell = 300\,\text{mm}$, width of $w = 25\,\text{mm}$ and thickness of $h = 1\,\text{mm}$, and is made of isotropic steel with a Young's modulus of 205 GPa, density of $7800\,\text{kg}\,\text{m}^{-3}$ and Poisson's ratio of 0.3. The model is meshed with 120 shear deformable, three-node quadratic beam elements (B32), resulting in $N = 1440$ DOFs. The dissipation in the beam is due to mass-proportional viscous damping, with coefficient $\alpha = 4\,\text{s}^{-1}$, resulting in a damping ratio of $\zeta_1 = 3.5\%$ in the first mode.

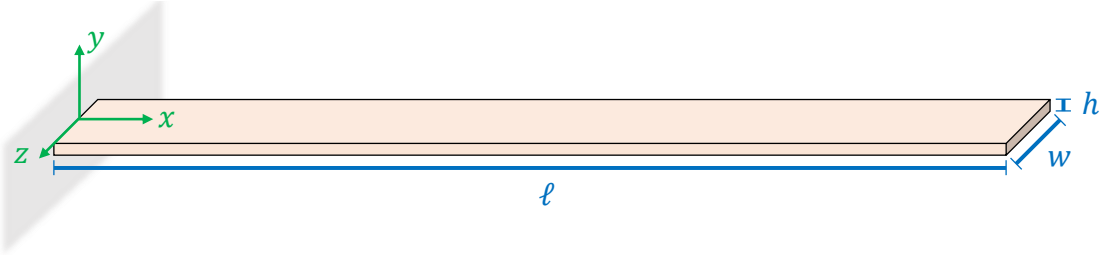

Figure 6.10. Schematic diagram of the cantilever beam.

Two different loading scenarios are considered, both of which involve a harmonic external excitation acting at the free end of the beam. In the first example, the external excitation acts along the y-direction, i.e. perpendicular to the axis of the beam in the original, undeformed configuration. The nonconservative forces acting on the beam can then be written as

$$\mathbf{F}_x(t, \dot{\mathbf{x}}) = P\,\mathbf{e}_i \cos(\Omega t) - \alpha \mathbf{M}\dot{\mathbf{x}}, \tag{6.13}$$

where P and Ω are the amplitude and frequency of excitation, respectively, $\mathbf{e}_i$ is the $N \times 1$ unit vector with a single non-zero element in its i^{th} position, and i is the index of the DOF corresponding to a translation of the tip node along the y-axis. In the second loading scenario, the external force remains perpendicular to the axis of the beam as the beam deforms, i.e.

$$\mathbf{F}_x(t, \mathbf{x}, \dot{\mathbf{x}}) = P\,\left[\mathbf{e}_i \cos\left(\mathbf{e}_k^\mathsf{T}\mathbf{x}\right) - \mathbf{e}_j \sin\left(\mathbf{e}_k^\mathsf{T}\mathbf{x}\right)\right] \cos(\Omega t) - \alpha \mathbf{M}\dot{\mathbf{x}}, \tag{6.14}$$

where j and k are the indices of the DOFs corresponding to a translation of the tip node along the x-axis, and a rotation of the tip node about the z-axis, respectively. Schematic diagrams of the two loadings scenarios are shown in figure 6.11.

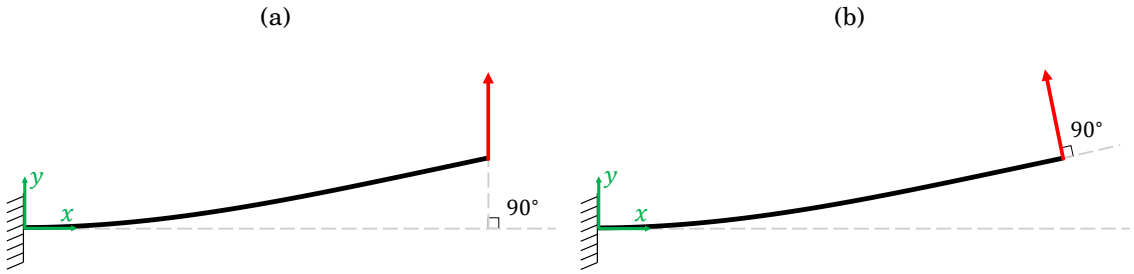

Figure 6.11. Schematic diagram of the two different loading scenarios: (a) force acting along the y-direction, (b) follower force which remains perpendicular to the beam axis as the beam deforms.

Here, the forced response of the cantilever beam in the vicinity of the first nonlinear normal mode is of interest, which has a linearised natural frequency of $\omega_1 = 57.8\,\mathrm{rad\,s^{-1}}$. As discussed and demonstrated in Chapter 4, the *conservative* dynamics in this region can be captured with a very high degree of accuracy and up to large vibration amplitudes, by a fifth-order, single-DOF ROM using the ICE-IC

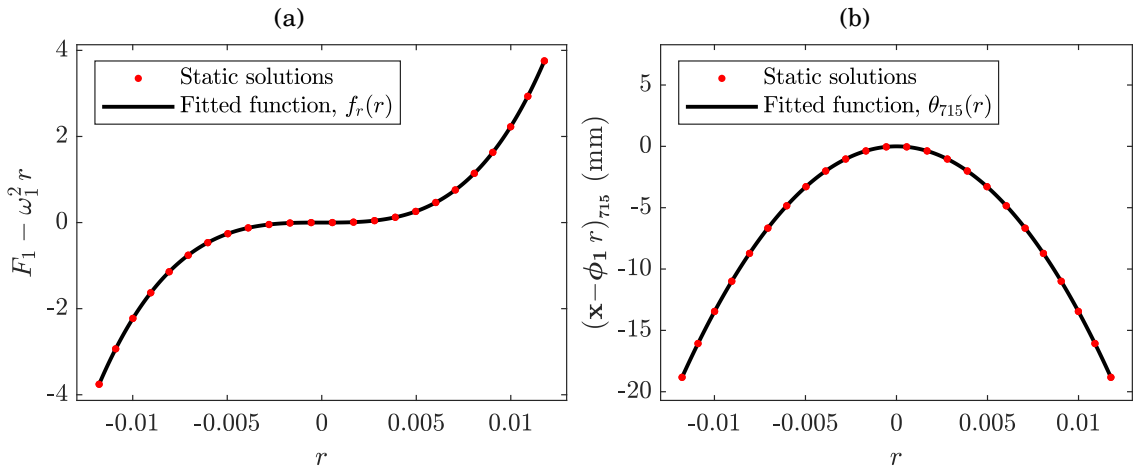

Figure 6.12. The static solution dataset used to approximate (a) the function of nonlinear restoring forces in the reduced space, and (b) the quasi-static coupling function associated with the 715^{th} DOF; similarly a quasi-static coupling function is approximated for each DOF.

method. As such, the same reduction basis ($\Phi_r = [\phi_1]$) and truncation order ($K = 5$) are used here. The static solution dataset used to compute the reduced parameters is obtained by applying a static force $F_1 \in [-45, +45]$ in the first mode, and extracting the corresponding displacement of the beam. The function of nonlinear restoring forces in the ROM, $f_r(r)$, is approximated using the $\{F_1 - \omega_1^2 r, r\}$ dataset, as shown in figure 6.12 (a), where r is the displacement of the first mode. Similarly, the quasi-static coupling functions, $\theta(r)$, are approximated using the $\{\mathbf{x} - \phi_1 r, r\}$ dataset. It should be highlighted that each quasi-static coupling function is approximated independently; an example is shown in figure 6.12 (b) for the 715^{th} element in θ, which is the DOF corresponding to a translation of the tip node along the x-axis.

Figure 6.13 (a) shows the forced response curve of the FE model (black crosses) and ICE-IC ROMs using both a linear (blue lines) and a nonlinear (red lines) projection of the nonconservative forces, when a constant-direction sinusoidal force is applied at the free end of the beam (first loading scenario) with $P = 0.9\,\text{N}$ and $\Omega/\omega_1 \in (0.8, 1.2)$. It can be seen that the proposed ROM remains highly accurate up to very large amplitudes ($Y_{\text{tip}} \sim 2\ell/3$), whilst the ROM obtained using the traditional approach overestimates the response of the FE model. This behaviour is similar to the example considered previously in figure 6.5 (b), whereby the traditional ROM is unable to account for the energy dissipated by the statically coupled modes. At the same

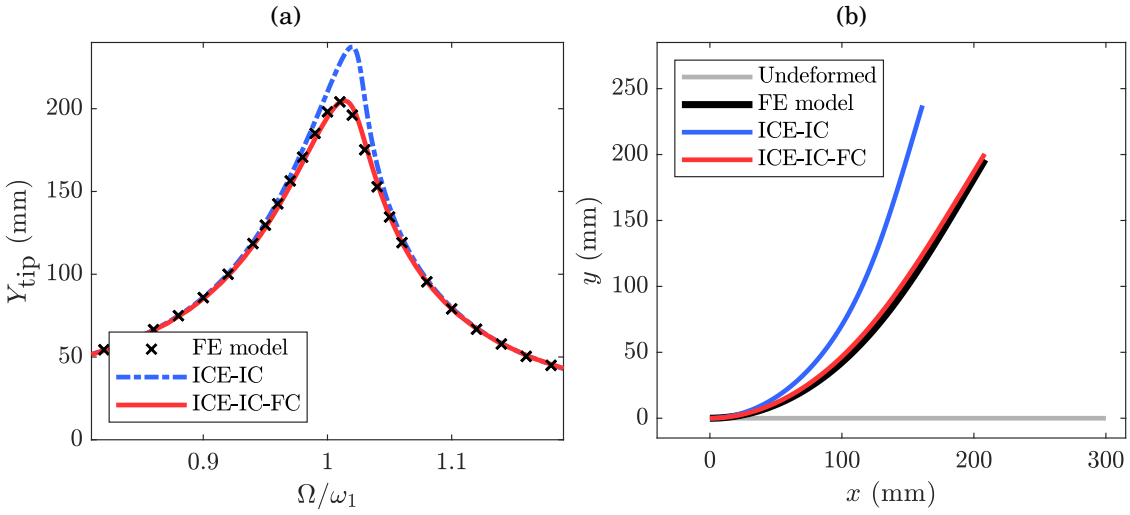

Figure 6.13. (a) Forced response curves of the FE model and the ICE-IC ROMs obtained based on the linear (blue line) and the nonlinear (red line) mapping of the nonconservative forces, for the first loading scenario (force along y-direction) with $P = 0.9\,\text{N}$. (b) Snapshots of the beam at its maximum deflection when $\Omega = 1.02\,\omega_1$.

time, the energy transferred into the statically coupled modes is negligible since the external forcing, which acts along the y-direction, is orthogonal to the axial modeshapes. Snapshots of the beam at its maximum deflection, as predicted by the two ROMs as well as the full-order FE model for $P = 0.9\,\mathrm{N}$ and $\Omega = 1.02\omega_1$, are shown in figure 6.13 (b).

The situation changes in the second loading scenario (figure 6.14), where a follower force with $P = 0.9\,\mathrm{N}$ and $\Omega/\omega_1 \in (0.8, 1.2)$ is considered. In this case, the axial component of the external excitation is significant, as the rotation of the cantilever beam about the z-axis is as large as $\sim 70^\circ$ at its free end, when $Y_{\mathrm{tip}} \sim 218\,\mathrm{mm}$. As a result, the uncaptured energy gained by the statically coupled axial modes is greater than the uncaptured energy dissipated due to damping, and the traditional ROM now underestimates the response of the FE model. On the other hand, the proposed ROM is able to capture the competing effect of both types of nonconservative forces, and accurately predict the forced response of the FE model.

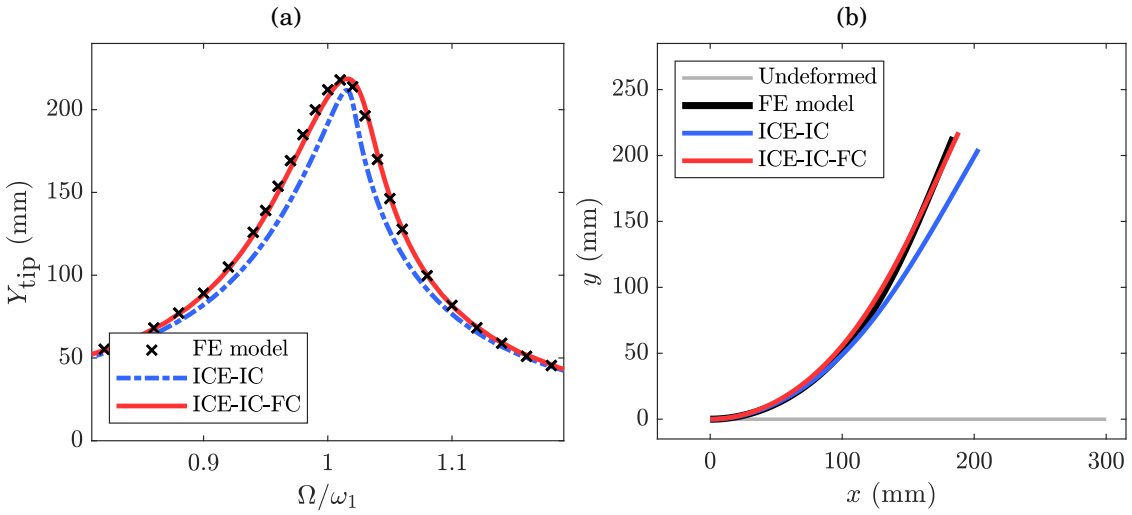

Figure 6.14. (a) Forced response curves of the FE model and the ICE-IC ROMs obtained based on the linear (blue line) and the nonlinear (red line) mapping of the nonconservative forces, for the second loading scenario (follower force) with $P = 0.9\,\mathrm{N}$. (b) Snapshots of the beam at its maximum deflection when $\Omega = 1.02\omega_1$.

6.7 Summary

This chapter has focussed on how force-based indirect reduced-order modelling methods, such as the ICE, can be appropriately extended to nonconservative structures,

enabling forced response curves to be computed directly in an accurate and efficient manner. The traditional approach of incorporating nonconservative forces in the ROM relies on a linear projection of these onto the reduced subspace. As such, only the nonconservative forces acting directly on the reduced modes can be captured, whilst any energy gained or dissipated by the statically condensed modes is neglected. Using a simple 2-DOF oscillator, it was shown that this can lead to a significant overestimation of the oscillation amplitude when the condensed modes dissipate non-negligible amounts of energy. Similarly, an FE model of an axially-excited cable was used to show that the traditional method not only underestimates the vibration amplitude on the primary resonance curve, but is also unable to capture fundamental behaviours of the cable, such as a 2:1 parametric resonance. This is because the traditional ROM is inherently unable to capture the external energy transferred to the axial modes, without including those directly in the reduction basis. This effect was also demonstrated using an FE model of a cantilever beam under two different loading scenarios: one where a constant-direction force and one where a follower force is applied at the free end of the beam.

Here, a nonlinear mapping of the physical coordinates into the reduced coordinates was used to show how the nonconservative forces acting on both the reduced, as well as the statically condensed modes, can be accounted for. This nonlinear mapping gives rise to some additional terms in the nonconservative reduced dynamics, which are referred to as *force compensation*. When these were taken into account, the ROM has shown excellent agreement with the full-order model, for all three structures considered.

The force compensation method proposed in this chapter, may be considered as an extension to existing indirect reduced-order modelling techniques, whereby the nonconservative forces are appended to the reduced conservative dynamics obtained using, for example, the ICE(-IC) method, resulting in dramatically improved accuracy. These additional terms are computed based on existing knowledge of the structure, i.e. the quasi-static coupling functions, and require no additional information from the FE model. In addition, the proposed formulation, whereby the physical coordinates are directly mapped into the reduced coordinates, circumvents the need for a full modal transform, which could otherwise be a bottleneck when considering large FE models. Whilst this chapter has focussed on nonconservative forces arising from harmonic external excitation and viscous damping, it should be highlighted that there is no restriction on the form that the function of nonconservative forces can take.

It is theorised that the force compensation approach can work well with other types of nonconservative forces, including friction. Limitations are likely to be encountered when the nonconservative forces cause the quasi-static coupling approximation to break down – this remains a topic for future work.

Chapter 7

Conclusions and future work

This aim of this thesis has been to further the current state-of-the-art of reduced-order modelling methods applicable to geometrically nonlinear engineering structures modelled using commercial FE software. In this final chapter, the findings of this thesis are summarised, and potential avenues for future research are outlined.

7.1 Conclusions

This thesis has focussed on non-intrusive, or indirect, reduced-order modelling methods, which can be employed in conjunction with commercial FE software, and are thus well-suited to industrial applications. As discussed in Chapter 2, such methods do not require access to the inner workings of the FE code or knowledge of the parameters characterising the underlying full-order equations of motion. Instead, reduced-order models are computed based on data extracted from the FE model, typically in the form of nonlinear static solutions, which are computationally inexpensive to obtain. The static solutions of the FE model may be obtained either by enforcing the structure into a prescribed static displacement and extracting the resulting reaction forces (STEP method), or by applying a static force to the structure and extracting the resulting displacement (ICE method). The latter approach has the advantage of implicitly capturing the response of the high-frequency in-plane modes within the stress manifold, even when the reduction basis consists only of transverse modes. As a result, ROMs obtained using the ICE method often require significantly fewer DOFs compared to their displacement-based counterparts, leading to larger computational savings.

Chapter 3: Accounting for quasi-static coupling

Nevertheless, the ICE method has traditionally suffered from issues related to the lack of invariance of the reduced subspace. Specifically, one of its major drawbacks is that the computed ROM parameters are greatly dependent on the scaling of the static forces used to obtain the calibration dataset, which may introduce significant errors if the relevant scale factors are not carefully tuned. In Chapter 3, this feature of the ICE method was investigated using a simple oscillator which exhibits quasi-static coupling between its two modes. It was demonstrated mathematically that, in general, quasi-static coupling introduces higher orders of nonlinearity in the reduced dynamics, beyond the order of nonlinearity present in the full-order model. It was shown that the traditional ICE ROM, which contains nonlinearities only up to the cubic order, was extremely sensitive to the force scale factor, both in terms of the estimated parameters as well as the corresponding backbone curves. On the other hand, ROMs which contain higher-order nonlinear terms were found to be not only more accurate, but also significantly more robust with respect to the force scale factor. These findings were also validated by computing ROMs of a clamped-clamped beam, modelled using commercial FE software.

In conclusion:

- Due to quasi-static coupling, ROMs obtained using the ICE method should, in general, include higher orders of nonlinearity than the full-order model.
- Even though ROMs with higher orders of nonlinearity require a larger number of parameters to be estimated, their invariance to force scale factor renders them more robust and more accurate for a wider range of operating conditions, and removes the need for any tuning of the force scale factor.

Chapter 4: Capturing in-plane inertia

Another drawback of the ICE method is that its applicability is limited to structures in which in-plane displacement is limited. This requirement arises from the fact that in-plane inertia/kinetic energy is assumed to be negligible. This approximation is often reasonable for structures such as thin plates and slender beams with fixed/pinned boundary conditions, however, this assumption is violated when considering structures with free boundary conditions (e.g. cantilever beams). In Chapter 4, this limitation of the ICE method was addressed by using a Lagrangian approach to demonstrate how in-plane kinetic energy can be accounted for in the

reduced dynamics. It was shown that this introduces some additional velocity- and acceleration-dependent terms in the reduced equations of motion relative to the traditional ICE method, which are referred to as inertial compensation. The proposed method was demonstrated using ICE ROMs with and without inertial compensation for an FE model of a cantilever beam. It was shown that the traditional ICE ROM severely overestimates the response frequency of the beam, as it is unable to capture the softening effect caused by in-plane inertia. On the other hand, excellent accuracy was observed when inertial compensation was included in the reduced dynamics.

In conclusion:

- In-plane kinetic energy can be accounted for in the reduced dynamics through some additional velocity- and acceleration-dependent terms. These can be computed using the existing static solution dataset, and do not require any additional information from the FE model.
- This additional treatment enables force-based indirect reduction methods to be applied to a far wider range of structures whilst maintaining accuracy to higher deflection amplitudes.

Chapter 5: Detecting internal resonances

Chapter 5 addressed the challenge of selecting an appropriate reduction basis without *a priori* knowledge of the full-order dynamics. Retaining redundant modes will lead to computationally suboptimal ROMs, whilst omitting dynamically significant modes will lead to inaccurate results, and important features such as internal resonances may not be captured. In this chapter, it was demonstrated how the error associated with static condensation can be efficiently approximated during model order reduction, in order to predict when dynamic modal interactions will occur. Specifically, it was proposed that each modal coordinate in a nonlinear system may be represented as the sum of a component that is quasi-statically coupled to the reduced modes, and a component that is dynamically independent of them — the latter part may be considered as the error arising from static condensation. The harmonic balance method was used to approximate the error dynamics independently of the reduced dynamics, thus enabling any dynamic interaction between the reduced and condensed modes to be identified. This can be achieved in a very computationally efficient manner, as a linear approximation of the error dynamics is considered. The proposed method was demonstrated using the simple oscillator, as well as a finite element model of

a clamped-clamped beam, and it was shown how the existence of a 1:3 and a 1:5 internal resonance, respectively, could be predicted based on single-mode ROMs.

In conclusion:

- The error associated with static condensation may be efficiently approximated during model order reduction using the harmonic balance method. This may serve as a tool for guiding the reduction basis selection process, as well as a computationally cheap method for validating the accuracy of ROMs, without the need for full-order simulations.
- This development removes the need for cumbersome trial-and-error processes and case-by-case treatment guided by empirical rules, and is a key step towards developing reduced-order modelling methods which can be applied systematically to a broad range of structures.

Chapter 6: Nonconservative structures

Chapter 6 considered the reduction of nonconservative structures, which enables the assessment of ROMs based on forced response curves, rather than just backbone curves. It was demonstrated how nonconservative forces acting on a structure may be reduced using a nonlinear mapping of the physical DOFs into the reduced coordinates. This was contrasted with the traditional approach, which relies on a linear mapping; as a result, only the forces acting directly on the reduced modes can be captured, whilst any energy gained or dissipated by the statically condensed modes is neglected. Using a 2-DOF oscillator, it was shown that this can lead to a significant overestimation of the oscillation amplitude when the condensed modes dissipate non-negligible amounts of energy. Equivalently, an FE model of an axially-excited inclined cable was used to show that the traditional method not only underestimates the vibration amplitude on the primary resonance curve, but is also unable to capture fundamental behaviours of the cable, such as a 2:1 parametric resonance. Similar results were observed for the large-amplitude vibrations of a cantilever beam modelled using commercial FE software under different excitation scenarios, including a follower force. The proposed method, which is referred to as force compensation, enables the nonconservative forces acting on the statically condensed modes to be accounted for in the reduced dynamics. Excellent agreement was observed between the forced response curves of the full-order models and those of the proposed ROMs, for all three structures.

In conclusion:

- The concept of reduction through projection onto a nonlinear manifold may be extended to nonconservative structures, such that any energy gained or dissipated by the statically condensed modes can be accounted for in the reduced dynamics, leading to highly accurate response predictions.
- The proposed formulation, whereby the physical coordinates are directly mapped into the reduced coordinates, circumvents the need for a full modal transform, which could otherwise be a bottleneck when considering large FE models.

7.2 Future work

Despite the recent advances in nonlinear reduced-order modelling, many potential avenues for future work are available. Some recommendations for interesting and potentially impactful research topics are outlined below:

- Throughout this thesis, reduction has been achieved based on a static condensation procedure. This requires that the natural frequencies of the reduced and condensed modes are well-separated, as is the case with low-frequency bending modes and high-frequency in-plane modes in plates and beams. However, when the slow/fast assumption does not hold, the unmodelled modes are better approximated as functions of not only the reduced displacements, but also the reduced velocities, as in the invariant manifold approach. The identification of such manifolds in a truly non-intrusive manner, for example via regression analysis and using sets of nonlinear *dynamic* solutions of the full-order model, could revolutionise indirect reduction methodologies and extend their applicability to a vast range of nonlinear systems.
- This thesis, as well as the vast majority of the literature on nonlinear reduced-order modelling, is concerned with the reduction of the dynamics of a structure about a single stable equilibrium. Future work could investigate reduced-order modelling of bistable or even multistable structures, and aim to address questions such as: How can multiple ROMs be combined in order to model a multistable structure? Can a single ROM capture the dynamics of a structure about multiple equilibria? What effect, if any, does symmetry have?

- In practical design applications in the engineering industry, the development cycle of structures often involves optimisation procedures and parametric studies. In this context, developing parametric ROMs, whose coefficients are functions of a set of physical properties of the structure, may dramatically reduce the upfront computational cost associated with reduced-order modelling. Research into how this may be achieved, whether it be in a black-box fashion or informed by underlying physical processes, could be of great value.
- This thesis has focussed on the reduction of nonlinear structural dynamics in isolation. However, in practical applications, problems from different domains are often coupled. Therefore, future work could be devoted to investigating the feasibility of the methods proposed herein, for the reduction of models which may include, for example, pizeoelectric or electrostatic couplings, thermal or aeroelastic effects, or fluid-structure interaction.

References

Allen, M. S., Kuether, R. J., Deaner, B. J., and Sracic, M. (2012). A Numerical Continuation Method to Compute Nonlinear Normal Modes Using Modal Reduction. In *53rd AIAA/ASME/ASCE/AHS/ASC Structures, Structural Dynamics and Materials Conference 20th AIAA/ASME/AHS Adaptive Structures Conference 14th AIAA*.

Amabili, M., Pellicano, F., and Vakakis, A. (2000). Nonlinear vibrations and multiple resonances of fluid-filled, circular shells, part 1: equations of motion and numerical results. *J. Vib. Acoust.*, 122(4):346–354.

Antonio, D., Zanette, D. H., and López, D. (2012). Frequency stabilization in nonlinear micromechanical oscillators. *Nature communications*, 3(1):1–6.

Bathe, K.-J. (2006). *Finite element procedures*. Klaus-Jurgen Bathe.

Bendiksen, O. O. (1987). Mode localization phenomena in large space structures. *AIAA Journal*.

Blevins, R. D., Holehouse, I., and Wentz, K. R. (1993). Thermoacoustic loads and fatigue of hypersonic vehicle skin panels. *Journal of Aircraft*, 30(6):971–978.

Brennan, M. J., Kovacic, I., Carrella, A., and Waters, T. P. (2008). On the jump-up and jump-down frequencies of the Duffing oscillator. *Journal of Sound and Vibration*.

Buza, G., Jain, S., and Haller, G. (2021). Using spectral submanifolds for optimal mode selection in nonlinear model reduction. *Proceedings of the Royal Society A*, 477(2246):20200725.

Caughey, T., Vakakis, A. F., and Sivo, J. (1990). Analytical study of similar normal modes and their bifurcations in a class of strongly non-linear systems. *International Journal of Non-Linear Mechanics*, 25(5):521–533.

Challa, V. R., Prasad, M., Shi, Y., and Fisher, F. T. (2008). A vibration energy harvesting device with bidirectional resonance frequency tunability. *Smart Materials and Structures*, 17(1):015035.

Chen, C., Zanette, D. H., Czaplewski, D. A., Shaw, S., and López, D. (2017). Direct observation of coherent energy transfer in nonlinear micromechanical oscillators. *Nature communications*, 8(1):1–7.

Chen, L.-Q. and Jiang, W.-A. (2015). Internal resonance energy harvesting. *Journal of Applied Mechanics*, 82(3).

Craig, R. R. and Bampton, M. C. C. (1968). Coupling of substructures for dynamic analyses. *AIAA Journal*.

Dankowicz, H. and Schilder, F. (2013). *Recipes for continuation*, volume 11. SIAM, Philadelphia, PA.

Dassault Systèmes (2017). Abaqus. Dassault Systèmes, Providence, RI.

de la Llave, R. and Kogelbauer, F. (2019). Global persistence of lyapunov subcenter manifolds as spectral submanifolds under dissipative perturbations. *SIAM Journal on Applied Dynamical Systems*, 18(4):2099–2142.

Doebling, S. W. S., Farrar, C. R. C., Prime, M. B. M., and Shevitz, D. W. D. (1996). Damage identification and health monitoring of structural and mechanical systems from changes in their vibration characteristics: a literature review. *Los Alamos National Laboratory*.

Ewins, D. J. and Saunders, H. (1986). Modal Testing: Theory and Practice. *Journal of Vibration Acoustics Stress and Reliability in Design*, 108(1):109.

Fahy, F. J. (1994). Statistical energy analysis: a critical overview. *Philosophical Transactions of the Royal Society of London. Series A: Physical and Engineering Sciences*.

Felippa, C. A., Guo, Q., and Park, K. (2015). Mass matrix templates: general description and 1d examples. *Archives of Computational Methods in Engineering*, 22(1):1–65.

Frangi, A. and Gobat, G. (2019). Reduced order modelling of the non-linear stiffness in mems resonators. *International Journal of Non-Linear Mechanics*, 116:211–218.

Givois, A., Grolet, A., Thomas, O., and Deü, J.-F. (2019). On the frequency response computation of geometrically nonlinear flat structures using reduced-order finite element models. *Nonlinear Dynamics*, 97(2):1747–1781.

Gonzalez-Buelga, A., Neild, S. A., Wagg, D. J., and Macdonald, J. H. G. (2008). Modal stability of inclined cables subjected to vertical support excitation. *Journal of Sound and Vibration*.

Gordon, R. W. and Hollkamp, J. J. (2011). Reduced-order models for acoustic response prediction. Technical Report AFRL-RB-WP-TR-2011-3040, Air Force Research Laboratory, Dayton, OH.

Haight, E. and King, W. (1972). Stability of nonlinear oscillations of an elastic rod. *The Journal of the Acoustical Society of America*, 52(3B):899–911.

Haller, G. and Ponsioen, S. (2016). Nonlinear normal modes and spectral submanifolds: existence, uniqueness and use in model reduction. *Nonlinear dynamics*, 86(3):1493–1534.

Hill, T. L. (2016). *Modal Interactions in Nonlinear Systems*. PhD thesis, University of Bristol.

Hill, T. L., Cammarano, A., Neild, S. A., and Wagg, D. J. (2015). Out-of-unison resonance in weakly nonlinear coupled oscillators. *Proceedings of the Royal Society A: Mathematical, Physical and Engineering Sciences*.

Hollkamp, J., Gordon, R., and Spottswood, S. (2003). Nonlinear sonic fatigue response prediction from finite element modal models: a comparison with experiments. In *44th AIAA/ASME/ASCE/AHS/ASC Structures, Structural Dynamics, and Materials Conference*, page 1709.

Hollkamp, J. J. and Gordon, R. W. (2008). Reduced-order models for nonlinear response prediction: Implicit condensation and expansion. *Journal of Sound and Vibration*, 318(4-5):1139–1153.

Hollkamp, J. J., Gordon, R. W., and Spottswood, S. M. (2005). Nonlinear modal models for sonic fatigue response prediction: a comparison of methods. *Journal of Sound and Vibration*, 284(3-5):1145–1163.

Hong, D., Nicolaidou, E., Hill, T. L., and Neild, S. A. (2020). Identifying phase-varying periodic behaviour in conservative nonlinear systems. *Proceedings of the Royal Society A: Mathematical, Physical and Engineering Sciences*, 476(2237):20200028.

Hsieh, S.-R., Shaw, S. W., and Pierre, C. (1994). Normal modes for large amplitude vibration of a cantilever beam. *International Journal of Solids and Structures*, 31(14):1981–2014.

Idelsohn, S. R. and Cardona, A. (1985). A load-dependent basis for reduced nonlinear structural dynamics. *Computers & Structures*, 20(1-3):203–210.

Idelsohn, S. R. and Cardona, A. (1985). A reduction method for nonlinear structural dynamic analysis. *Computer Methods in Applied Mechanics and Engineering*, 49(3):253–279.

Jacob, B. and Ebecken, N. (1992). Adaptive reduced integration method for nonlinear structural dynamic analysis. *Computers & structures*, 45(2):333–347.

Jain, S. and Haller, G. (2022). How to compute invariant manifolds and their reduced dynamics in high-dimensional finite element models. *Nonlinear dynamics*, 107(2):1417–1450.

Jain, S., Tiso, P., Rutzmoser, J. B., and Rixen, D. J. (2017). A quadratic manifold for model order reduction of nonlinear structural dynamics. *Computers & Structures*, 188:80–94.

Jensen, K., Kim, K., and Zettl, A. (2008). An atomic-resolution nanomechanical mass sensor. *Nature nanotechnology*, 3(9):533–537.

Jezequel, L. and Lamarque, C. (1991). Analysis of non-linear dynamical systems by the normal form theory. *Journal of Sound and Vibration*, 149(3):429–459.

Kerschen, G., Peeters, M., Golinval, J. C., and Vakakis, A. F. (2009). Nonlinear normal modes, Part I: A useful framework for the structural dynamicist. *Mechanical Systems and Signal Processing*.

Kim, K., Radu, A. G., Wang, X., and Mignolet, M. P. (2013). Nonlinear reduced order modeling of isotropic and functionally graded plates. *International Journal of Non-Linear Mechanics*, 49:100–110.

King, M. E. and Vakakis, A. F. (1994). An Energy-Based Formulation for Computing Nonlinear Normal Modes in Undamped Continuous Systems. *Journal of Vibration and Acoustics*, 116(3):332.

Kuether, R. J. (2014). *Nonlinear modal substructuring of geometrically nonlinear finite element models*. PhD Thesis, The University of Wisconsin-Madison.

Kuether, R. J. and Allen, M. S. (2014). A numerical approach to directly compute nonlinear normal modes of geometrically nonlinear finite element models. *Mechanical Systems and Signal Processing*, 46(1):1–15.

Kuether, R. J., Deaner, B. J., Hollkamp, J. J., and Allen, M. S. (2015). Evaluation of geometrically nonlinear reduced-order models with nonlinear normal modes. *AIAA Journal*, 53(11):3273–3285.

Lan, C., Qin, W., and Deng, W. (2015). Energy harvesting by dynamic unstability and internal resonance for piezoelectric beam. *Applied Physics Letters*, 107(9):093902.

Lazarus, A., Thomas, O., and Deü, J.-F. (2012). Finite element reduced order models for nonlinear vibrations of piezoelectric layered beams with applications to nems. *Finite Elements in Analysis and Design*, 49(1):35–51.

Liu, M., Zheng, L., Zhou, P., and Xiao, H. (2020). Stability and dynamics analysis of in-plane parametric vibration of stay cables in a cable-stayed bridge with superlong spans subjected to axial excitation. *Journal of Aerospace Engineering*, 33(1):04019106.

Mahboob, I. and Yamaguchi, H. (2008). Bit storage and bit flip operations in an electromechanical oscillator. *Nature nanotechnology*, 3(5):275–279.

Manevich, L. and Mikhlin, I. (1972). On periodic solutions close to rectilinear normal vibration modes. *Journal of Applied Mathematics and Mechanics*, 36(6):988–994.

Manolas, D., Riziotis, V., and Voutsinas, S. (2015). Assessing the importance of geometric nonlinear effects in the prediction of wind turbine blade loads. *Journal of Computational and Nonlinear Dynamics*, 10(4):041008.

McEwan, M., Wright, J. R., Cooper, J. E., and Leung, A. Y. T. (2001). A combined modal/finite element analysis technique for the dynamic response of a non-linear beam to harmonic excitation. *Journal of Sound and Vibration*, 243(4):601–624.

Mei, C. and Moorthy, J. (1995). Numerical simulation of the nonlinear response of composite plates under combined thermal and acoustic loading.

Mignolet, M. P., Przekop, A., Rizzi, S. A., and Spottswood, S. M. (2013). A review of indirect/non-intrusive reduced order modeling of nonlinear geometric structures. *Journal of Sound and Vibration*, 332(10):2437–2460.

Mignolet, M. P. and Soize, C. (2008). Stochastic reduced order models for uncertain geometrically nonlinear dynamical systems. *Computer Methods in Applied Mechanics and Engineering*, 197(45-48):3951–3963.

Mottershead, J. and Friswell, M. (1993). Model Updating In Structural Dynamics: A Survey. *Journal of Sound and Vibration*, 167(2):347–375.

MSC Software Corporation (2003). Nastran. MSC Software Corporation, Santa Ana, CA.

Muravyov, A. A. and Rizzi, S. A. (2003). Determination of nonlinear stiffness with application to random vibration of geometrically nonlinear structures. *Computers & Structures*, 81(15):1513–1523.

Nahon, M. (1999). Dynamics and control of a novel radio telescope antenna. In *Modeling and Simulation Technologies Conference and Exhibit*, page 4120.

Nash, M. (1977). *Nonlinear Structural Dynamics by Finite Element Modal Synthesis*. PhD thesis, Imperial College, University of London.

Nayfeh, A. H. (1981). *Introduction to Perturbation Techniques*. Wiley-Interscience, New York.

Nayfeh, A. H. and Mook, D. T. (1995). *Nonlinear oscillations*. John Wiley & Sons, Weinheim, Germany.

Neild, S. A., Champneys, A. R., Wagg, D. J., Hill, T. L., and Cammarano, A. (2015). The use of normal forms for analysing nonlinear mechanical vibrations. *Philosophical Transactions of the Royal Society A: Mathematical, Physical and Engineering Sciences*, 373(2051):20140404.

Nguyen, C. T.-C. (2007). Mems technology for timing and frequency control. *IEEE transactions on ultrasonics, ferroelectrics, and frequency control*, 54(2):251–270.

Nicolaidou, E., Hill, T. L., and Neild, S. A. (2020). Indirect reduced-order modelling: using nonlinear manifolds to conserve kinetic energy. *Proceedings of the Royal Society A: Mathematical, Physical and Engineering Sciences*, 476(2243):20200589.

Nicolaidou, E., Hill, T. L., and Neild, S. A. (2021). Detecting internal resonances during model reduction. *Proceedings of the Royal Society A: Mathematical, Physical and Engineering Sciences*, 477(2250):20210215.

Nicolaidou, E., Hill, T. L., and Neild, S. A. (2022). Nonlinear mapping of non-conservative forces for reduced-order modelling. *Proceedings of the Royal Society A: Mathematical, Physical and Engineering Sciences*, 478(2268):20220522.

Nicolaidou, E., Melanthuru, V. R., Hill, T. L., and Neild, S. A. (2020). Accounting for quasi-static coupling in nonlinear dynamic reduced-order models. *Journal of Computational and Nonlinear Dynamics*, 15(7):071002.

Opreni, A., Vizzaccaro, A., Frangi, A., and Touzé, C. (2021). Model order reduction based on direct normal form: application to large finite element mems structures featuring internal resonance. *Nonlinear Dynamics*, 105(2):1237–1272.

Opreni, A., Vizzaccaro, A., Touzé, C., and Frangi, A. (2022). High order direct parametrisation of invariant manifolds for model order reduction of finite element structures: application to generic forcing terms and parametrically excited systems.

Pai, P. F. (2007). *Highly flexible structures: modeling, computation, and experimentation*. American Institute of Aeronautics and Astronautics.

Pai, P. F. and Nayfeh, A. H. (1990). Non-linear non-planar oscillations of a cantilever beam under lateral base excitations. *International Journal of Non-Linear Mechanics*, 25(5):455–474.

Pak, C. H. and Rosenberg, R. M. (1968). On the existence of normal mode vibrations in nonlinear systems. *Quarterly of Applied Mathematics*.

Papazafeiropoulos, G., Muñiz-Calvente, M., and Martínez-Pañeda, E. (2017). Abaqus2matlab: a suitable tool for finite element post-processing. *Advances in Engineering Software*, 105:9–16.

Patil, M. J., Hodges, D. H., and Cesnik, C. E. (2001). Limit-cycle oscillations in high-aspect-ratio wings. *Journal of fluids and structures*, 15(1):107–132.

Peeters, M., Viguié, R., Sérandour, G., Kerschen, G., and Golinval, J. C. (2009). Nonlinear normal modes, Part II: Toward a practical computation using numerical continuation techniques. *Mechanical Systems and Signal Processing*, 23(1):195–216.

Perez, R., Wang, X., and Mignolet, M. P. (2014). Nonintrusive structural dynamic reduced order modeling for large deformations: enhancements for complex structures. *Journal of Computational and Nonlinear Dynamics*, 9(3).

Pesheck, E. (2000). *Reduced order modeling of nonlinear structural systems using nonlinear normal modes and invariant manifolds*. PhD thesis, The University of Michigan.

Pesheck, E., Boivin, N., Pierre, C., and Shaw, S. W. (2001). Nonlinear modal analysis of structural systems using multi-mode invariant manifolds. *Nonlinear Dynamics*, 25(1-3):183–205.

Petrov, E. P. and Ewins, D. J. (2003). Analytical formulation of friction interface elements for analysis of nonlinear multi-harmonic vibrations of bladed disks. *Journal of Turbomachinery*.

Pinto da Costa, A., Martins, J., Branco, F., and Lilien, J.-L. (1996). Oscillations of bridge stay cables induced by periodic motions of deck and/or towers. *Journal of Engineering Mechanics*, 122(7):613–622.

Przekop, A., Azzouz, M. S., Guo, X., Mei, C., and Azrar, L. (2004). Finite element multiple-mode approach to nonlinear free vibrations of shallow shells. *AIAA journal*, 42(11):2373–2381.

Przekop, A., Guo, X., Azzouz, S., and Mei, C. (2004). Reinvestigation of nonlinear random response of shallow shells using finite element modal formulation. In *45th AIAA/ASME/ASCE/AHS/ASC Structures, Structural Dynamics & Materials Conference*, page 1553.

Przekop, A. and Rizzi, S. A. (2006). A reduced order method for predicting high cycle fatigue of nonlinear structures. *Computers & structures*, 84(24-25):1606–1618.

Rand, R. H. (1971). Nonlinear Normal Modes in Two-Degree-of-Freedom Systems. *Journal of Applied Mechanics*, 38(2):561.

Rand, R. H. (1974). A direct method for non-linear normal modes. *International Journal of Non-Linear Mechanics*, 9(5):363–368.

Rayleigh, J. W. S. B. (1896). *The theory of sound*, volume 2. Macmillan & Company.

Reddy, J. N. (1993). *An introduction to the finite element method*. McGraw-Hill, New York.

Rizzi, S. A. and Przekop, A. (2005). The effect of basis selection on static and random acoustic response prediction using a nonlinear modal simulation. Technical Report TP-2005-213943, NASA.

Rizzi, S. A. and Przekop, A. (2008). System identification-guided basis selection for reduced-order nonlinear response analysis. *Journal of Sound and Vibration*, 315(3):467–485.

Rosenberg, R. M. (1960). Normal modes of nonlinear dual-mode systems. *Journal of Applied Mechanics, Transactions ASME*.

Rosenberg, R. M. (1962). The normal modes of nonlinear n-degree-of-freedom systems. *Journal of Applied Mechanics, Transactions ASME*.

Rosenberg, R. M. (1966). On nonlinear vibrations of systems with many degrees of freedom. In *Advances in applied mechanics*, volume 9, pages 155–242. Elsevier.

Rugar, D., Budakian, R., Mamin, H., and Chui, B. (2004). Single spin detection by magnetic resonance force microscopy. *Nature*, 430(6997):329–332.

Rutzmoser, J. (2018). *Model order reduction for nonlinear structural dynamics*. PhD thesis, Technische Universität München.

Rutzmoser, J. B., Rixen, D. J., and Tiso, P. (2014). Model order reduction using an adaptive basis for geometrically nonlinear structural dynamics. In *International Conference on Noise and Vibration Engineering, ISMA, Leuven, Belgium*.

Rutzmoser, J. B., Rixen, D. J., Tiso, P., and Jain, S. (2017). Generalization of quadratic manifolds for reduced order modeling of nonlinear structural dynamics. *Computers & Structures*, 192:196–209.

Sanders, J., Murdock, J., and Verhulst, F. (2007). Averaging methods in nonlinear dynamical systems. In *Applied Mathematical Sciences*. Springer.

Sayed, M. and Kamel, M. (2012). 1:2 and 1:3 internal resonance active absorber for non-linear vibrating system. *Applied Mathematical Modelling*.

Schilder, F. and Dankowicz, H. (2015). Continuation Core (COCO). URL `http://sourceforge.net/\allowbreak projects/cocotools/`.

Segalman, D. J. and Dohrmann, C. R. (1996). A method for calculating the dynamics of rotating flexible structures, part 1: Derivation. *Journal of Sound and Vibration*, 118(3):313–317.

Shaw, S. W. and Pierre, C. (1991). Non-linear normal modes and invariant manifolds. *Journal of Sound and Vibration*, 150(1):170–173.

Shaw, S. W. and Pierre, C. (1992). On nonlinear normal modes. In *American Society of Mechanical Engineers, Design Engineering Division (Publication) DE*.

Shaw, S. W. and Pierre, C. (1993). Normal modes for non-linear vibratory systems. *Journal of Sound and Vibration*, 164(1):85–124.

Shaw, S. W. and Pierre, C. (1994). Normal modes of vibration for non-linear continuous systems. *Journal of Sound and Vibration*, 169(3):319–347.

Shaw, S. W., Pierre, C., and Pesheck, E. (1999). Modal analysis-based reduced-order models for nonlinear structures – an invariant manifold approach. *The Shock and Vibration Digest*, 31(1):3–16.

Shearer, C. M. and Cesnik, C. E. S. (2007). Nonlinear flight dynamics of very flexible aircraft. *Journal of Aircraft*, 44(5):1528–1545.

Shen, Y., Béreux, N., Frangi, A., and Touzé, C. (2021). Reduced order models for geometrically nonlinear structures: assessment of implicit condensation in comparison with invariant manifold approach. *European Journal of Mechanics-A/Solids*, 86:104165.

Shi, Y. and Mei, C. (1996). A finite element time domain modal formulation for large amplitude free vibrations of beams and plates. *Journal of Sound and Vibration*, 193(2):453–464.

Slaats, P., De Jongh, J., and Sauren, A. (1995). Model reduction tools for nonlinear structural dynamics. *Computers & structures*, 54(6):1155–1171.

Sombroek, C. S., Tiso, P., Renson, L., and Kerschen, G. (2018). Numerical computation of nonlinear normal modes in a modal derivative subspace. *Computers & Structures*, 195:34–46.

Tartaruga, I., Elliott, A., Hill, T. L., Neild, S. A., and Cammarano, A. (2019). The effect of nonlinear cross-coupling on reduced-order modelling. *International Journal of Non-Linear Mechanics*, 116:7–17.

Thomas, O. and Bilbao, S. (2008). Geometrically nonlinear flexural vibrations of plates: In-plane boundary conditions and some symmetry properties. *Journal of Sound and Vibration*, 315(3):569–590.

Thomas, O., Sénéchal, A., and Deü, J.-F. (2016). Hardening/softening behavior and reduced order modeling of nonlinear vibrations of rotating cantilever beams. *Nonlinear dynamics*, 86(2):1293–1318.

Thothadri, M. and Moon, F. (2005). Nonlinear system identification of systems with periodic limit-cycle response. *Nonlinear Dynamics*, 39(1):63–77.

Tiso, P. (2011). Optimal second order reduction basis selection for nonlinear transient analysis. In *Modal Analysis Topics, Volume 3*, pages 27–39. Springer.

Tiso, P., Jansen, E., and Abdalla, M. (2011). Reduction method for finite element nonlinear dynamic analysis of shells. *AIAA journal*, 49(10):2295–2304.

Touzé, C. and Amabili, M. (2006). Nonlinear normal modes for damped geometrically nonlinear systems: Application to reduced-order modelling of harmonically forced structures. *Journal of sound and vibration*, 298(4-5):958–981.

Touzé, C., Amabili, M., and Thomas, O. (2008). Reduced-order models for large-amplitude vibrations of shells including in-plane inertia. *Computer methods in applied mechanics and engineering*, 197(21-24):2030–2045.

Touzé, C. and Thomas, O. (2004). Reduced-order modeling for a cantilever beam subjected to harmonic forcing. In *Proceedings of the EUROMECH Colloquium 457: Non-linear Modes of Vibrating Systems,*, pages 165–168.

Touzé, C. and Thomas, O. (2006). Non-linear behaviour of free-edge shallow spherical shells: effect of the geometry. *International Journal of non-linear Mechanics*, 41(5):678–692.

Touzé, C., Thomas, O., and Chaigne, A. (2004). Hardening/softening behaviour in non-linear oscillations of structural systems using non-linear normal modes. *Journal of Sound and Vibration*, 273(1-2):77–101.

Touzé, C., Thomas, O., and Huberdeau, A. (2004). Asymptotic non-linear normal modes for large-amplitude vibrations of continuous structures. *Computers & structures*, 82(31-32):2671–2682.

Touzé, C., Vizzaccaro, A., and Thomas, O. (2021). Model order reduction methods for geometrically nonlinear structures: a review of nonlinear techniques. *Nonlinear Dynamics*, 105(2):1141–1190.

Vakakis, A. F. (1992). Non-similar normal oscillations in a strongly non-linear discrete system. *Journal of Sound and Vibration*, 158(2):341–361.

Vakakis, A. F. (1997). Non-linear normal modes (NNMs) and their applications in vibration theory: An overview.

Vakakis, A. F., Manevitch, L. I., Mikhlin, Y. V., Pilipchuk, V. N., and Zevin, A. A. (2001). *Normal modes and localization in nonlinear systems*. Springer.

Vakakis, A. F., Manevitch, L. I., Mlkhlin, Y. V., Pilipchuk, V. N., and Zevin, A. A. (1996). *Normal Modes and Localization in Nonlinear Systems*. Wiley.

Van Damme, C. I., Allen, M. S., and Hollkamp, J. J. (2020). Updating geometrically nonlinear reduced-order models using nonlinear modes and harmonic balance. *AIAA Journal*, 58(8):3553–3568.

VanDamme, C. I. and Allen, M. S. (2017). Nonlinear normal modes of a curved beam and its response to random loading. In *Nonlinear Dynamics, Volume 1*, pages 115–126. Springer.

Vizzaccaro, A., Givois, A., Longobardi, P., Shen, Y., Deü, J.-F., Salles, L., Touzé, C., and Thomas, O. (2020). Non-intrusive reduced order modelling for the dynamics of geometrically nonlinear flat structures using three-dimensional finite elements. *Computational Mechanics*, 66(6):1293–1319.

Vizzaccaro, A., Opreni, A., Salles, L., Frangi, A., and Touzé, C. (2022). High order direct parametrisation of invariant manifolds for model order reduction of finite element structures: application to large amplitude vibrations and uncovering of a folding point. *Nonlinear Dynamics*, pages 1–47.

Vizzaccaro, A., Shen, Y., Salles, L., Blahoš, J., and Touzé, C. (2021). Direct computation of nonlinear mapping via normal form for reduced-order models of finite element nonlinear structures. *Computer Methods in Applied Mechanics and Engineering*, 384:113957.

Wagg, D. J. and Neild, S. A. (2015). Approximate methods for analysing nonlinear vibrations. *Solid Mechanics and its Applications*.

Wang, X., Mignolet, M., Eason, T., and Spottswood, S. (2009). Nonlinear reduced order modeling of curved beams: a comparison of methods. In *50th AIAA/ASME/ASCE/AHS/ASC Structures, Structural Dynamics, and Materials Conference*, page 2433.

Warnitchai, P., Fujino, Y., and Susumpow, T. (1995). A non-linear dynamic model for cables and its application to a cable-structure system. *Journal of Sound and Vibration*, 187(4):695 – 712.

Wu, L. and Tiso, P. (2016). Nonlinear model order reduction for flexible multibody dynamics: a modal derivatives approach. *Multibody System Dynamics*, 36(4):405–425.

Zega, V., Gattere, G., Koppaka, S., Alter, A., Vukasin, G. D., Frangi, A., and Kenny, T. W. (2020). Numerical modelling of non-linearities in mems resonators. *Journal of Microelectromechanical Systems*, 29(6):1443–1454.